TECHNISCHE UNIVERSITÄT WIEN

DIPLOMARBEIT

Uncertainty Assessment of TLS Distance Deviations evoked by Material and Incidence Angle

zur Erlangung des akademischen Grades

Diplom-Ingenieur

im Rahmen des Studiums

Geodäsie und Geoinformation

eingereicht von

Rupert Lettner BSc
Matrikelnummer 01525461

ausgeführt im Forschungsbereich Ingenieurgeodäsie
des Department für Geodäsie und Geoinformation
der Fakultät für Mathematik und Geoinformation
der Technischen Universität Wien

Betreuung
Univ.Prof. Dr.-Ing. Hans-Berndt Neuner
Univ.Ass. Finn Linzer MSc

Wien, am 12. Dezember 2022

(Unterschrift Verfasser) (Unterschrift Betreuer)

Affidavit

I declare in lieu of oath, that I wrote this thesis myself in accordance with the recognised principles for scientific papers. All resources used, especially the literature, are listed in this thesis. If text passages from sources are used literally, they are marked as such.

I confirm that this work is original and has not been submitted elsewhere for any examination, nor is it currently under consideration for a thesis elsewhere.

Vienna, December 12, 2022

(Signature)

Acknowledgements

I would like to thank all the people who supported me during my studies and especially throughout the preparation of this thesis. I am aware of the privilege to enjoy this education and that I would not have reached this point without support.

First, I want to thank my supervisor Univ.Prof. Dr.-Ing. Hans-Berndt Neuner for offering me this topic, for the continuous technical support and for the precise and carefully thought out criticism. Thank you! Many thanks to my co-supervisor Univ.Ass Finn Linzer for the patience, the countless explanations, the practical help during the measurements and the extra dose of motivation and fun! I am very grateful to both of you for allowing me to work with you and learn from you.

Thank you, Stefan, for proofreading the thesis and for the many useful suggestions for optimisation.

I also would like to thank my fellow students for their valuable companionship and their motivating spirit. You made my studies to an unforgettable part of my life!

Last but not least, I am very grateful to my whole family and especially to my parents for their unrestricted support of any kind along my path. Thanks a million!

Abstract

Terrestrial Laser Scanners (TLS) are increasingly being used in the field of engineering geodesy. The 3D-point accuracy achievable with state-of-the-art TLS is in the low millimetre range and manufacturers of TLS even state ranging precisions down to the submillimetre range. This encourages investigations on suspected systematic effects that might influence the uncertainty of TLS distance measurements. The commercial launch of geodetic multi stations - these instruments combine the capabilities of total stations (TS) and TLS - allow a new approach to check the performance of TLS distance measurements, particularly with respect to the material being scanned and the laser's angle of incidence on the scanned object. Such a methodology, referred to as ROSIAM, for evaluating TLS distance measurements has been developed by the research unit of Engineering Geodesy at TU Wien. The basic principle is the direct comparison of TLS distances with reference distances obtained by an instrument with higher accuracy.

The objective of this work is to determine and quantify sources of uncertainty in the ROSIAM methodology and to create a comprehensive uncertainty budget for the derived differences between TLS distances and reference distances. Variance-covariance propagation and Monte Carlo simulation are used as computational methods to determine the combined effect of all known sources of uncertainty on the distance differences. An essential step for this is the development of a network transformation model to establish a spatial relationship between the measurands of TLS and reference instrument, which can be placed arbitrarily to each other.

In this thesis, the uncertainties of distance differences are determined for incidence angles ranging from 0 to 60 gon and for seven different materials. Significant disparities in distance differences are found between all materials for a majority of the incidence angles studied. This leads to the conclusion that systematic effects underlie the observed distance differences.

It is also ascertained that there are no significant differences in the uncertainties of the distance differences with regard to material and incidence angle. Therefore, a single value of 0.2 mm can be used as standard uncertainty for all TLS distance differences. However, this value is limited to the ROSIAM method, the materials investigated and the range of incidence angles investigated.

Based on the results, the ROSIAM methodology is deemed sensitive enough to investigate suspected systematic effects in TLS distance measurements of multi stations.

Kurzfassung

Terrestrische Laserscanner (TLS) finden immer häufiger Anwendung im Bereich der Ingenieurgeodäsie. Die mit modernen TLS erreichbare 3D-Punktgenauigkeit liegt im niedrigen Millimeterbereich. Zudem geben Hersteller Präzisionen für die Distanzmessung an, die bis in den Submillimeterbereich reichen. Dies treibt dazu an, vermutete systematische Effekte zu untersuchen, welche die Unsicherheit von TLS-Entfernungsmessungen beeinflussen könnten. Die Markteinführung von geodätischen Multistationen - Kombinationsinstrumente aus Totalstation (TS) und TLS - ermöglicht einen neuen Ansatz zur Genauigkeitüberprüfung von TLS-Distanzmessungen, insbesondere in Bezug auf das zu scannende Material und den Einfallswinkel zwischen Laserstrahl und Objekt. Eine solche, als ROSIAM bezeichnete, Methode zur Durchführung und Auswertung von TLS-Distanzmessungen wurde vom Forschungsbereich für Ingenieurgeodäsie der TU Wien entwickelt. Das Grundprinzip ist der direkte Vergleich von TLS-Distanzen und Referenzdistanzen, welche mit einem Instrument höherer Genauigkeit ermittelt wurden.

Ziel dieser Arbeit ist es, die Unsicherheitsquellen der ROSIAM-Methode zu bestimmen und zu quantifizieren sowie ein umfassendes Unsicherheitsbudget für die abgeleiteten Differenzen von TLS-Distanzen und Referenzdistanzen zu erstellen. Die Varianz-Kovarianz-Fortpflanzung und die Monte-Carlo-Simulation werden als Berechnungsmethoden eingesetzt, um die gemeinsame Auswirkung aller Unsicherheitseinflüsse auf die Distanzdifferenzen zu bestimmen. Ein wesentlicher Schritt dazu ist die Entwicklung eines Modells zur Netztransformation, welches einen funktionalen räumlichen Zusammenhang zwischen den Messgrößen des terrestrischen Laserscanners und jenen des Referenzinstruments herstellt. Die Instrumente können dabei beliebig zueinander positioniert und orientiert sein.

In dieser Arbeit werden die Unsicherheiten von Distanzdifferenzen für Einfallswinkel von 0 bis 60 gon und für sieben verschiedene Materialien bestimmt. Zwischen allen Materialien wurden signifikante Unterschiede bei den Distanzdifferenzen für jeweils einen Großteil der untersuchten Einfallswinkel festgestellt. Dies lässt den Schluss zu, dass den vorliegenden Distanzdifferenzen systematische Effekte zugrunde liegen.

Es wurde auch festgestellt, dass keine signifikanten Unterschiede in den Unsicherheiten der Distanzdifferenzen bezüglich Material und Einfallswinkel vorliegen. Daher kann ein einheitlicher Wert von 0.2 mm als Standardunsicherheit für die Distanzdifferenzen verwendet werden. Die Anwendung dieser Standardunsicherheit ist jedoch auf die ROSIAM-Methode, die untersuchten Materialien und den Bereich der untersuchten Einfallswinkel zu beschränken.

Die Ergebnisse zeigen insgesamt, dass die ROSIAM-Methode geeignet ist, um vermutete systematische Effekte bei TLS-Distanzmessungen von Multistationen zu untersuchen.

Contents

Acknowledgements v

Abstract vii

Kurzfassung ix

1. Introduction 1
- 1.1. Motivation . . . 1
- 1.2. Related Work . . . 1
- 1.3. Aim of the Thesis . . . 2
- 1.4. Outline of the Thesis . . . 2

2. Fundamentals 3
- 2.1. Methodological Fundamentals . . . 3
  - 2.1.1. Adjustment Theory . . . 3
  - 2.1.2. Variance Component Estimation . . . 6
  - 2.1.3. Guide to the Expression of Uncertainty in Measurement (GUM) . . . 7
  - 2.1.4. Monte Carlo Method . . . 10
  - 2.1.5. Statistical Test . . . 11
- 2.2. Hardware and Software . . . 13
  - 2.2.1. Hardware . . . 13
  - 2.2.2. Software . . . 16

3. ROSIAM 19
- 3.1. ROSIAM System . . . 19
  - 3.1.1. High-Accuracy Network . . . 19
  - 3.1.2. Instrument Setup . . . 20
- 3.2. ROSIAM Procedure . . . 20
  - 3.2.1. Network Measurement . . . 21
  - 3.2.2. Network Evaluation . . . 22
  - 3.2.3. Scan Measurement . . . 22
  - 3.2.4. Scan Evaluation . . . 23

4. Development of a Model for Network Transformation 25
- 4.1. Transformation Model . . . 25
- 4.2. Adjustment Model . . . 26

5. Quantification of Uncertainties in ROSIAM 29
- 5.1. Overview . . . 29
- 5.2. Measurand Preprocessing . . . 30
- 5.3. Atmospheric Correction . . . 32

5.4. Reflector . . . 33
5.5. Total Station (Terrestrial Laser Scanner) . . . 36
5.6. Laser Tracker . . . 37
5.7. Handheld Scanner . . . 37
5.8. Variance Component Estimation . . . 38
5.9. Network Transformation . . . 40
5.9.1. Input Quantities . . . 40
5.9.2. Functional Model . . . 43
5.9.3. Result . . . 43
5.9.4. Effect on Distance Differences (ΔD) . . . 44
5.10. Scan Point Matching . . . 46
5.11. Scan Uncertainty . . . 48
5.12. Axis Eccentricity . . . 48
5.13. Neglected Influential Quantities . . . 49
5.14. Summary . . . 50

6. Analysis of Uncertainties **53**
6.1. Analysis of Distance Differences . . . 54
6.2. Analysis of Uncertainties of ΔD . . . 56
6.3. Validation . . . 57

7. Conclusion **61**

References **65**

List of Acronyms **67**

List of Figures **69**

A. Scanned Materials **73**

B. Results: Distance Differences and Uncertainties **75**

1. Introduction

1.1. Motivation

Laser scanners are used as instruments for fast data acquisition in many fields of geodetic applications. Variations in environmental parameters such as scan distance, object material and angle of incidence on objects are inevitable. These factors may systematically influence the accuracy of scans. Manufacturers naturally consider diverse situations and numerous influencing variables when meticulously deriving uncertainty specifications for their instruments. The market launch of instruments with quality certificates requires the compliance to designated international standards. However, internal findings through thorough experiments that go beyond the required international standards are usually not published. Knowledge on the behaviour and magnitude of additional factors impacting the instrument's accuracy would open up the opportunity of significantly undercutting the instrument's specifications stated by the manufacturer. Keeping that in mind, the instrument would also be usable for applications with even more accurate requirements. In this context, this thesis is intended to contribute to the research of Finn Linzer, who is investigating systematic distance deviations in scanning total stations.

1.2. Related Work

Already in the year 2000, distance deviations relating to the calibration of a scanner's electronic distance measurement (EDM) unit were found (Lichti *et al.* 2000). Significant systematics in measured distances for different terrestrial laser scanners of the second generation (see: Staiger 2011) were detected in experiments carried out by Kersten *et al.* (2008). Investigated factors of influence were scanning distance and incidence angle, whereat the manufacturer's accuracy specifications were met for all instruments. Also, test procedures for a possible standardised methodology for calibration were proposed.

The performance of the multi station Leica MS60 was compared against other scanning total stations and conventional TLS by Lachat *et al.* (2017). An instrument of this model also serves as terrestrial laser scanner in the experiments of this thesis. In Voegtle *et al.* (2008) extensive experiments were carried out on the influence of object colour, surface roughness, surface wetness, surface reflectivity and ambient illumination on the accuracy of TLS distance measurements. Exemplary, an increase in the measurement accuracy was ascertained for scans at night-time and onto bright materials. The influence of different types of wood and wetness was found to be marginal while light-transmissive material and metal plates caused mean square errors that were much larger than the general ranging accuracy of the laser scanner. The returned signal intensity has also been taken into account in similar experiments to derive relations to material properties and distance accuracy (Kaasalainen *et al.* 2009; Voegtle *et al.* 2008).

Starting with (Zámečníková *et al.* 2014a,b) a novel approach for assessing the accuracy of distance measurements of scanning total stations (i.e. multi stations) was introduced. Single points were scanned, staked out and measured by two theodolites with known relative position. With that, reference distances to the scanned points were derived and a direct comparison with the scanned distances was possible.

A systematic influence of the surface reflectivity and the angle of incidence at close range was hypothesised. With the utilisation of a high-accuracy network for the determination of reference distances, different geometric scanning situations could be realised more flexibly. Particular emphasis was put on a comprehensive consideration of possible sources of uncertainty. By qualitatively estimating their interfering influence behaviour and their magnitude, significant distance deviations in connexion with the angle of incidence were proved (Zámečníková *et al.* 2018). A continuation with further and more in-depth experiments was published by Linzer *et al.* (2021) with an additional focus on automating the test procedure.

1.3. Aim of the Thesis

The following topics are defined as aims of this thesis.

- Development of a model for network estimation with consistent results to existing models and the opportunity for unrestricted uncertainty propagation throughout itself
- Quantification of influence quantities and uncertainty propagation of the influence quantities in the measurement procedure developed by the research unit of Engineering Geodesy at TU Wien.
- Analysis of the uncertainty of distance differences related to incidence angle and material.

1.4. Outline of the Thesis

The thesis is structured into the following six chapters. Chapter 2 comprises the methodological fundamentals and lists the used hardware and software. In Chapter 3 the ROSIAM methodology is described. The development of a model for network transformation is presented in Chapter 4. Chapter 5 focuses on the quantification of uncertainties in the ROSIAM methodology and the propagation of uncertainties to the derived distance differences. The distance differences are statistically analysed in Chapter 6 based on the calculated uncertainties. The conclusion of the thesis is provided in Chapter 7.

2. Fundamentals

This chapter provides an introduction to the topics that form the theoretical basis of this work. It encompasses the Gauss-Helmert model in adjustment theory including the concept of variance component analysis. Since the results involve uncertainty estimates based on measurements, suitable methods for tracing uncertainties through a chain of mathematical concepts are covered: the variance-covariance propagation (VCP) and the Monte Carlo method (MCM). Another section is dedicated to the 'Guide to the Expression of Uncertainty in Measurement' (GUM), an ISO standard to whom the whole calculation process is kept in conformity.

2.1. Methodological Fundamentals

The propagation of distributions (and hence the propagation of uncertainties expressed by distributions) can be implemented in several ways according to the GUM (BIPM *et al.* 2008a):

(a) analytical methods, i.e. methods that make use of the mathematical representation of the probability distribution

(b) uncertainty propagation based on replacing the model by a first-order Taylor series approximation

(c) as (b), except that contributions derived from higher-order terms in the Taylor series approximation are included

(d) numerical methods that implement the propagation of distributions, specifically using Monte Carlo methods

Only methods of type (b) and (d) are utilised in this thesis and are addressed in Chapters 2.1.3 and 2.1.4.

2.1.1. Adjustment Theory

In the field of metrology, measurements themselves often do not directly represent desired physical values. However, measurements can be linked to these physical values via mathematical functions. Overdetermination can lead to either statistically non-optimal or ambiguous results. Concepts provided by adjustment theory, however, intend to obtain best and unambiguous estimates for the unknowns.

The most adequate concept for the tasks in this thesis is the Gauss-Helmert model (GHM), also known as the 'universal case' of adjustment theory. In adjustment theory the terms observation and unknown or parameter are used instead of measurement and physical value. The description of the GHM is extracted and adapted from Niemeier (2008).

Functional Model Assuming observations l_i $(i = 1,\dots,n)$ are pooled in a (n, 1) vector $\boldsymbol{L}$ and the unknowns x_j $(j = 1,\dots,u)$ in vector $\boldsymbol{X}$ with dimension (u, 1).

$$\boldsymbol{L} = \begin{bmatrix} l_1 \\ l_2 \\ \vdots \\ l_n \end{bmatrix}; \quad \boldsymbol{X} = \begin{bmatrix} x_1 \\ x_2 \\ \vdots \\ x_u \end{bmatrix} \tag{2.1}$$

Then, Equation (2.2) outlines the functional model ψ that establishes a relation between observations and unknown parameters in a system of b equations. Since overdetermination $(n > u)$ is assumed, this system can not be solved consistently but results in a vector of discrepancies $\boldsymbol{w}$.

$$\psi(\boldsymbol{L},\boldsymbol{X}) = \boldsymbol{w} \tag{2.2}$$

In contrary, a consistent solution of the system of equations (2.3) can be written for the vector of adjusted observations $\hat{\boldsymbol{L}}$ and adjusted parameters $\hat{\boldsymbol{X}}$.

$$\psi(\hat{\boldsymbol{L}},\hat{\boldsymbol{X}}) = \boldsymbol{0} \tag{2.3}$$

A solution of Equation (2.2) requires approximate values for the observations $(\boldsymbol{L}^0)$ and for the parameters $(\boldsymbol{X}^0)$. Relations between the observed, approximate and adjusted variables are given in the subsequent formulas.

$$\hat{\boldsymbol{X}} = \boldsymbol{X}^0 + \hat{\boldsymbol{x}} \tag{2.4}$$

$$\hat{\boldsymbol{L}} = \boldsymbol{L} + \boldsymbol{v} \tag{2.5}$$

$$\boldsymbol{l} = \boldsymbol{L} - \boldsymbol{L}^0 \tag{2.6}$$

Linearising Equation (2.2) in a Taylor series leads to:

$$\psi(\boldsymbol{L},\boldsymbol{X}) = \psi(\boldsymbol{L},\boldsymbol{X}^0) + \frac{\partial\psi(\boldsymbol{L},\boldsymbol{X}^0)}{\partial\boldsymbol{L}}(\hat{\boldsymbol{L}} - \boldsymbol{L}) + \frac{\partial\psi(\boldsymbol{L},\boldsymbol{X}^0)}{\partial\boldsymbol{X}^0}(\hat{\boldsymbol{X}} - \boldsymbol{X}^0) = \boldsymbol{0}. \tag{2.7}$$

The partial derivatives with respect to the observations are pooled in the Jacobian matrix $\boldsymbol{B}$. Another Jacobian matrix $\boldsymbol{A}$ is filled with the partial derivatives with respect to the parameters and is labelled as design matrix.

$$\boldsymbol{A} = \frac{\partial\psi(\boldsymbol{L},\boldsymbol{X}^0)}{\partial\boldsymbol{X}^0} = \begin{bmatrix} \frac{\partial\psi_1}{\partial X_1^0} & \frac{\partial\psi_1}{\partial X_2^0} & \cdots & \frac{\partial\psi_1}{\partial X_u^0} \\ \frac{\partial\psi_2}{\partial X_1^0} & \frac{\partial\psi_2}{\partial X_2^0} & \cdots & \frac{\partial\psi_2}{\partial X_u^0} \\ \vdots & \vdots & \ddots & \vdots \\ \frac{\partial\psi_b}{\partial X_1^0} & \frac{\partial\psi_b}{\partial X_2^0} & \cdots & \frac{\partial\psi_b}{\partial X_u^0} \end{bmatrix} \tag{2.8}$$

$$\boldsymbol{B} = \frac{\partial\psi(\boldsymbol{L},\boldsymbol{X}^0)}{\partial\boldsymbol{L}} = \begin{bmatrix} \frac{\partial\psi_1}{\partial L_1} & \frac{\partial\psi_1}{\partial L_2} & \cdots & \frac{\partial\psi_1}{\partial L_n} \\ \frac{\partial\psi_2}{\partial L_1} & \frac{\partial\psi_2}{\partial L_2} & \cdots & \frac{\partial\psi_2}{\partial L_n} \\ \vdots & \vdots & \ddots & \vdots \\ \frac{\partial\psi_b}{\partial L_1} & \frac{\partial\psi_b}{\partial L_2} & \cdots & \frac{\partial\psi_b}{\partial L_n} \end{bmatrix} \tag{2.9}$$

The linearised model can now be formulated in a compact notation:

$$\boldsymbol{B}\boldsymbol{v} + \boldsymbol{A}\hat{\boldsymbol{x}} + \boldsymbol{w} = \boldsymbol{0}. \tag{2.10}$$

The degrees of freedom f is computed as difference between number of equations and number of parameters and is used to decide whether the model is overdetermined ($f > 0$).

$$f = b - u \tag{2.11}$$

The handling of the adjustment as a linear problem implies the advantage that well-known numerical linear algebra can be applied. In case of n observations and n unknowns a unique solution can be reached. An overdetermined problem has no unique solution, since the residuals $\boldsymbol{v}$ in (2.10) cannot be made to reach zero. However, they can be made as small as possible (Horvath 2014; Trefethen *et al.* 1997).

Stochastic Model In order to account for the accuracy of measurements, the observations are attached with uncertainty information. These a-priori uncertainties exert influence on the uncertainties of the parameters via the functional relations. The a-priori uncertainty information for an $(n, 1)$ observation vector is summarised in a (n, n) covariance matrix:

$$\boldsymbol{\Sigma}_{ll} = \begin{bmatrix} \sigma_1^2 & \rho_{12}\,\sigma_1\,\sigma_2 & \dots & \rho_{1n}\,\sigma_1\,\sigma_n \\ \rho_{21}\,\sigma_2\,\sigma_1 & \sigma_2^2 & \dots & \rho_{2n}\,\sigma_2\,\sigma_n \\ \vdots & \vdots & \ddots & \vdots \\ \rho_{n1}\,\sigma_n\,\sigma_1 & \rho_{n2}\,\sigma_n\,\sigma_2 & \dots & \sigma_n^2 \end{bmatrix}. \tag{2.12}$$

The main diagonal contains the variances of the observations. Off-diagonal elements represent correlations between observations which can also be zero. For the adjustment only relative accuracies are needed. Hence, the covariance matrix is split up into the variance factor σ_0^2 and the cofactor matrix $\boldsymbol{Q}_{ll}$.

$$\boldsymbol{\Sigma}_{ll} = \sigma_0^2 \boldsymbol{Q}_{ll} \tag{2.13}$$

The variance factor represents a shifting parameter used to link the relative accuracies in $\boldsymbol{Q}_{ll}$ to an absolute level of accuracy. In more complex models also single observations or groups of observations can be assigned with their own variance factors as explained in Chapter 2.1.2. The inversion of the cofactor matrix leads to the weight matrix $\boldsymbol{P}$.

$$\boldsymbol{P} = (\boldsymbol{Q}_{ll})^{-1} \tag{2.14}$$

Based on the estimation principle of Least Squares (2.15) the extended optimisation criterion (2.16) for the Gauss-Helmert model can be derived as shown in Krabs (1979).

$$\boldsymbol{v}^T \boldsymbol{P} \boldsymbol{v} \longrightarrow min \tag{2.15}$$

$$\Omega = \boldsymbol{v}^T \boldsymbol{P} \boldsymbol{v} - 2\boldsymbol{k}^T (\boldsymbol{B}\boldsymbol{v} + \boldsymbol{A}\hat{\boldsymbol{x}} + \boldsymbol{w}) \tag{2.16}$$

Derivation of (2.16) with respect to $\boldsymbol{v}$ and $\boldsymbol{x}$ leads to a system of equations shown in matrix notation in (2.17).

$$\begin{bmatrix} \boldsymbol{B}\boldsymbol{Q}_{ll}\boldsymbol{B}^T & \boldsymbol{A} \\ \boldsymbol{A}^T & \boldsymbol{0} \end{bmatrix} \begin{bmatrix} \boldsymbol{k} \\ \hat{\boldsymbol{x}} \end{bmatrix} = \begin{bmatrix} -\boldsymbol{w} \\ \boldsymbol{0} \end{bmatrix} \tag{2.17}$$

Inversion of this system grants direct access to a vector containing the adjusted parameters $\hat{\boldsymbol{x}}$:

$$\begin{bmatrix} \boldsymbol{k} \\ \hat{\boldsymbol{x}} \end{bmatrix} = - \begin{bmatrix} \boldsymbol{B}\boldsymbol{Q}_{ll}\boldsymbol{B}^T & \boldsymbol{A} \\ \boldsymbol{A}^T & \boldsymbol{0} \end{bmatrix}^{-1} \begin{bmatrix} \boldsymbol{w} \\ \boldsymbol{0} \end{bmatrix}. \tag{2.18}$$

2.1.2. Variance Component Estimation

In particular, when the functional model combines observations of different types and instruments e.g. distances and angles, the accuracy relations between groups of observations might be insufficiently known a-priori. The concept of variance component estimation (VCE) enables to not just estimate a single global variance factor but to assign groups of observations or individual observations with sub-variance factors, which are named variance components (Heunecke *et al.* 2013). In the course of the global test of the adjustment model, the fundamental relation in Formula (2.19) shows that the residual square sum is an unbiased estimator of the variance factor $\hat{\sigma}_0^2$.

$$E(\Omega) = (n-u)\hat{\sigma}_0^2 \tag{2.19}$$

Thus, the a-posteriori variance factor is calculated as the squared weighted residuals divided by the total redundancy r, which is the difference between the number of observations n and the number of parameters u. (Horvath 2014)

$$\hat{\sigma}_0^2 = \frac{\Omega}{r} = \frac{\boldsymbol{v}^T \boldsymbol{P} \boldsymbol{v}}{n-u} \tag{2.20}$$

To correctly apply the VCE, the stochastic model of the Gauss-Helmert model is altered to consider individual a-priori variance components. The covariance matrix of the observations is therefore written as a sum of submatrices.

$$\boldsymbol{\Sigma}_{ll} = \sum_{i=1}^{k} \boldsymbol{\Sigma}_i = \sigma_{0,1}^2 \boldsymbol{Q}_1 + \sigma_{0,2}^2 \boldsymbol{Q}_2 + \cdots + \sigma_{0,k}^2 \boldsymbol{Q}_k \tag{2.21}$$

If no correlations among groups of observations exist, the framework simplifies. In this case of ranked cofactors, the cofactor matrix $\boldsymbol{Q}$ decomposes into linearly independent cofactor submatrices (2.22).

$$\boldsymbol{Q}_1 = \begin{bmatrix} \overline{\boldsymbol{Q}}_1 & \boldsymbol{0} & \dots & \boldsymbol{0} \\ \boldsymbol{0} & \boldsymbol{0} & \dots & \boldsymbol{0} \\ \vdots & \vdots & \ddots & \vdots \\ \boldsymbol{0} & \boldsymbol{0} & \dots & \boldsymbol{0} \end{bmatrix}; \quad \boldsymbol{Q}_2 = \begin{bmatrix} \boldsymbol{0} & \boldsymbol{0} & \dots & \boldsymbol{0} \\ \boldsymbol{0} & \overline{\boldsymbol{Q}}_2 & \dots & \boldsymbol{0} \\ \vdots & \vdots & \ddots & \vdots \\ \boldsymbol{0} & \boldsymbol{0} & \dots & \boldsymbol{0} \end{bmatrix}; \quad \boldsymbol{Q}_k = \begin{bmatrix} \boldsymbol{0} & \boldsymbol{0} & \dots & \boldsymbol{0} \\ \boldsymbol{0} & \boldsymbol{0} & \dots & \boldsymbol{0} \\ \vdots & \vdots & \ddots & \vdots \\ \boldsymbol{0} & \boldsymbol{0} & \dots & \overline{\boldsymbol{Q}}_k \end{bmatrix} \tag{2.22}$$

Since Equation (2.20) is evaluated after the adjustment, the variance component estimation is also an iterative process. "Therefore, an initial value $\alpha_{0,i}^2$ for $\sigma_{0,i}^2$ is needed. The initial value $\alpha_{0,i}^2$ shall be chosen in that way, that the variance components $\hat{\sigma}_0^2$ are approximately 1. In each iteration step, $\hat{\sigma}_0^2$ of each observation group is computed as shown in Equation (2.20) and then multiplied by $\alpha_{0,i}^2$. The method converges, if $\hat{\sigma}_0^2 = 1$. The true variance component is the improved initial value of $\alpha_{0,i}^2$." (Horvath 2014). In fact, Equation (2.21) will develop practically to (2.23).

$$\boldsymbol{\Sigma}_{ll} = \sigma_{0,1}^2(\alpha_{0,1}^2 \boldsymbol{Q}_1) + \sigma_{0,2}^2(\alpha_{0,2}^2 \boldsymbol{Q}_2) + \cdots + \sigma_{0,k}^2(\alpha_{0,k}^2 \boldsymbol{Q}_k) \tag{2.23}$$

Since VCE is constructed on top of the adjustment, some prerequisites have to be fulfilled (Grimm-Pitzinger *et al.* 1986):

- knowledge of variance proportions within groups of observations
- sufficient conjunction of different observations groups by a coefficient matrix to ensure mutual interference
- the measurements follow a normal distribution i.e. the measurements are void of systematic and gross errors
- reliable parameter estimation is assumed i.e. redundancies inside groups of observations are balanced and sufficiently large ($r_{g,i} > 50$)(Förstner 1979)

2.1.3. Guide to the Expression of Uncertainty in Measurement (GUM)

The 'Guide to the Expression of Uncertainty in Measurement' is a guide published by the Joint Committee for Guides in Metrology (JCGM). Its purpose is to provide industry, research organisations, calibration and gauging authorities as well as common users with rules how to deduce standardised, comprehensible parameters that express the quality of measurements. To avoid misunderstandings and to support the clarity of the statements in this chapter, definitions according to the GUM of some important terms are given below (BIPM *et al.* 2008b).

- **(measurable) quantity**: attribute of a phenomenon, body or substance that may be determined quantitatively
- **measurement**: set of operations being done to determine a value of a quantity
- **value (of a quantity)**: magnitude of a particular quantity generally expressed as a unit of measurement multiplied by a number
- **principle of measurement**: scientific basis of a measurement e.g. Doppler effect, thermoelectric effect
- **method of measurement**: logical sequence of operations used in the performance of measurements e.g. null method, differential method
- **measurand**: particular quantity subject to measurement
- **accuracy of measurement**: closeness of the agreement between the result of a measurement and a true value of the measurand.

The key term 'uncertainty' has two meanings (BIPM *et al.* 2008b). First, uncertainty as a concept means doubt about the validity of the result of a measurement. On the other hand, uncertainty (of measurement) is a parameter associated with the result of a measurement, that characterises the dispersion of the values that could reasonably be attributed to the measurand. The standard deviation, for example, is one possible parameter to express uncertainty of measurement. It is understood that the result of the measurement is the best estimate of the value of the measurand, and that all components of uncertainty, including those arising from systematic effects, such as components associated with corrections and reference standards, contribute to the dispersion. Evidently, accuracy and uncertainty are inversely related: high accuracy implies low uncertainty and low accuracy implies high uncertainty (Kirkup *et al.* 2006).

The uncertainty in the result of a measurement generally consists of several components which may be grouped into two categories according to the way in which their numerical value is estimated. Both types are based on probability distributions and the uncertainty components resulting from either type are quantified by variances or standard deviations.

Type A Uncertainty Uncertainties of Type A are evaluated by statistical methods. In a common situation a sequence of repeated measurements will give slightly different values due to random errors. This sequence is analysed by calculating the mean and then considering individual differences from this mean. The scatter of these individual differences is a rough indication of the uncertainty of measurement: the greater the scatter, the more uncertain the measurement (Kirkup *et al.* 2006). The empirical variance $s^2(x)$ in (2.24) is one possibility to express uncertainty.

$$s^2(x) = \frac{1}{n-1}\sum_{j=1}^{n}\left(x_j - \overline{x}\right)^2 \tag{2.24}$$

Equation (2.24) contains the arithmetic mean value $\overline{x}$ of the series of observations which is calculated as (2.25) shows.

$$\overline{x} = \frac{1}{n}\sum_{j=1}^{n} x_j \tag{2.25}$$

According to the GUM, uncertainties of type A should be reported along with their degrees of freedom ν (DoF). The DoF is a number assigned to a statistical sample or its estimated parameters which describes the number of values that are free to be varied with the given information (Donnelly *et al.* 2016). "In applications such as that being considered, where there are n independent samples, the number of degrees of freedom is simply the number of independent variables less the number of constraints c." (Dunn *et al.* 2012)

$$\nu = n - c \tag{2.26}$$

The degrees of freedom of n independent observations equals to $n-1$ when an empirical variance $s^2(x)$ is derived, because one constraint emerges from the previous calculation of the arithmetic mean.

Type B Uncertainty Uncertainties of Type B comprises uncertainties evaluated by means other than the statistical analysis of series of observations. For an estimate x_i of an input quantity, the associated estimated variance $u^2(x_i)$ is evaluated by scientific judgement based on all available information on the possible variability of the quantity. The pool of information may include previous measurement data, experience or general knowledge of the behaviour and properties of relevant materials and instruments, manufacturer's specifications, data provided in calibration and other certificates and uncertainties assigned to reference data taken from handbooks (BIPM *et al.* 2008b).

Combining Standard Uncertainties A crucial step is the correct mathematical combination of uncertainty information regardless of its type. The GUM precisely describes this approach which is rooted is the Gaussian Law of Error Propagation. Considering quantity y being a function of quantities x_i $(i = 1 \ldots n)$ with their individual standard uncertainties $u(x_i)$. Then the combined standard uncertainty u_c of quantity y is derived as shown in (2.27). No distinction between type A and B is made when evaluating the standard uncertainty of the quantity y.

$$u_c^2(y) = \left(\frac{\partial y}{\partial x_1}\right)^2 u^2(x_1) + \left(\frac{\partial y}{\partial x_2}\right)^2 u^2(x_2) + \ldots \left(\frac{\partial y}{\partial x_n}\right)^2 u^2(x_n) \tag{2.27}$$

Equation (2.27) can be rewritten in a more compact form (2.28) as shown in Kirkup *et al.* (2006).

$$u_c^2(y) = \sum_{i=1}^{n}\left(\frac{\partial y}{\partial x_i}\right)^2 u^2(x_i) \tag{2.28}$$

The partial derivatives are named sensitivity coefficients and are abbreviated as c_i. With that, Equation (2.29) is derived (Kirkup *et al.* 2006).

$$u_c^2(y) = \sum_{i=1}^{n} c_i^2 u^2(x_i) \tag{2.29}$$

As extension to the standard uncertainty, the GUM proposes the expanded uncertainty U_k which is obtained by the multiplication of the standard uncertainty with a coverage factor k (2.30).

$$U_k = k \cdot \sqrt{u_c^2(y)} \tag{2.30}$$

The coverage factor is typically in the range of 2 to 3 and is chosen so that U_k encompasses a large fraction of the probability distribution around the measurement result.

Table 2.1 lists the most common coverage factors and their corresponding levels of confidence for the standard normal distribution.

Table 2.1.: Value of the coverage factor k_p that results in an interval with a level of confidence p assuming standard normal distribution (BIPM *et al.* 2008b)

Level of confidence p (percent)	**Coverage factor** k_p
68.27	1
90	1.645
95	1.960
95.45	2
99	2.576
99.73	3

To account for the combination of uncertainties following different probability distributions, weight factors G_i are introduced in Equation (2.31).

$$U_k = k \cdot \sqrt{\sum_{i=1}^{n} G_i \, (c_i \, u_i)^2} \tag{2.31}$$

The particular variables are now:

k	coverage factor
G_i	weight factor of quantity x_i
u_i	uncertainty contribution of quantity x_i
c_i	sensitivity coefficient of quantity x_i

Finally, Equation (2.31) is extended according to Pesch (2003) to vectorial shape and is adapted for the consideration of correlations among the influencing quantities x_i.

$$\boldsymbol{U_k} = k \cdot \sqrt{\left(\frac{\partial f}{\partial x_1}, \frac{\partial f}{\partial x_2}, \cdots, \frac{\partial f}{\partial x_n} \right) \begin{pmatrix} G_1 \, u_1^2 & \sqrt{G_1 \, G_2} \, u_1 \, u_2 \, \rho_{1,2} & \cdots & \sqrt{G_1 \, G_n} \, u_1 \, u_n \, \rho_{1,n} \\ \sqrt{G_2 \, G_1} \, u_2 \, u_1 \, \rho_{2,1} & G_2 \, u_2^2 & \cdots & \sqrt{G_2 \, G_n} \, u_2 \, u_n \, \rho_{2,n} \\ \vdots & \vdots & & \vdots \\ \sqrt{G_n \, G_1} \, u_n \, u_1 \, \rho_{n,1} & \sqrt{G_n \, G_2} \, u_n \, u_2 \, \rho_{n,2} & \cdots & G_n \, u_n^2 \end{pmatrix} \begin{pmatrix} \frac{\partial f}{\partial x_1} \\ \frac{\partial f}{\partial x_2} \\ \vdots \\ \frac{\partial f}{\partial x_n} \end{pmatrix}} \tag{2.32}$$

Also a combined uncertainty is allocated with a degree of freedom. Especially in view of the sample size for a type A uncertainty the degree of freedom reveals the information of statistical validity. The pooled DoF is calculated by the equation of Welch-Satterthwaithe (2.33). Since uncertainties of type B are not calculated from known series of measurements there are no DoF deducible. Therefore, the degree of freedom for an uncertainty of type B by definition is $\nu_B = \infty$.

$$\nu = \frac{u_c^4}{\sum_{i=1}^{N} \frac{u_i^4(y_i)}{\nu_i}} \tag{2.33}$$

In practice, uncertainty information from data sheets may be available in the form of absolute intervals (often denoted as specification limits, error limits, error intervals or maximum measurement errors). Without specific knowledge about the probability distribution of the quantity, the GUM recommends to assume that a realisation of the quantity is equally probable to lie anywhere within the given interval. This means the assumption of a uniform distribution (rectangular distribution) is sensible. For a given interval a_- to a_+, the expected value of the quantity is the midpoint of the interval, $x_i = (a_- + a_+)/2$, and the associated variance is calculated as shown in Equation (2.34) (BIPM *et al.* 2008b).

$$u^2(x_i) = \frac{(a_+ - a_-)^2}{12} \tag{2.34}$$

The derivation of Equation (2.34) as well as more conversion rules to standard uncertainties for further probability distributions can be found in Pesch (2003).

2.1.4. Monte Carlo Method

The Monte Carlo method (MCM), also called Monte Carlo simulation, is a numerical method for the propagation of distributions by performing random sampling from probability distributions (BIPM *et al.* 2008a). It is particularly suitable for strongly non-linear functional models. The MCM can generally be expected to give valid results, since it makes no approximating assumptions. The implementation of the MCM is shown diagrammatically in Figure 2.1 and is described by the step-by-step procedure subsequently.

(a) The number of Monte Carlo trials M is selected. It controls the number of input samples and the number of model evaluations to be performed. The quality of the results improves as M increases. The GUM suggests M to be in the range of 10^4 to 10^6, depending on the expected quality of the output uncertainty. Since M is strongly related to computer processing time, especially for complex functional models, a lower number of Monte Carlo trails is accepted as a trade-off for a shorter computation time.

(b) Determination of all input quantities including the corresponding probability distributions.

(c) As realisation of the input quantities X, M vectors are generated by taking samples from the assigned probability density functions (PDF). If appropriate, samples are drawn from the joint PDF.

(d) The functional model $Y = f(X)$ is evaluated for each vector of input quantities.

(e) The model values are sorted into strictly increasing order.

(f) The sorted model values are used to from a discrete representation $\boldsymbol{G}$ of the distribution function for the output quantity.

(g) The discrete representation $\boldsymbol{G}$ is used to derive an estimate y for the output quantity Y and a standard uncertainty $u(y)$, associated with y. Practically, the average and standard deviation of the model values are built.

(h) Optionally, a coverage interval for Y can be formed using G and a stipulated coverage probability p.

A condition for the valid application of the MCM is a continuous functional model f with respect to the input quantities. Furthermore, the distribution function for the output quantity Y must be continuous and strictly increasing towards the mode. As mentioned in (a), a sufficiently large number of samples M is required.

As shown in Wyszkowska (2017), results of the MCM and those derived by covariance propagation approximate each other when the number of samples increases and the functions are linear.

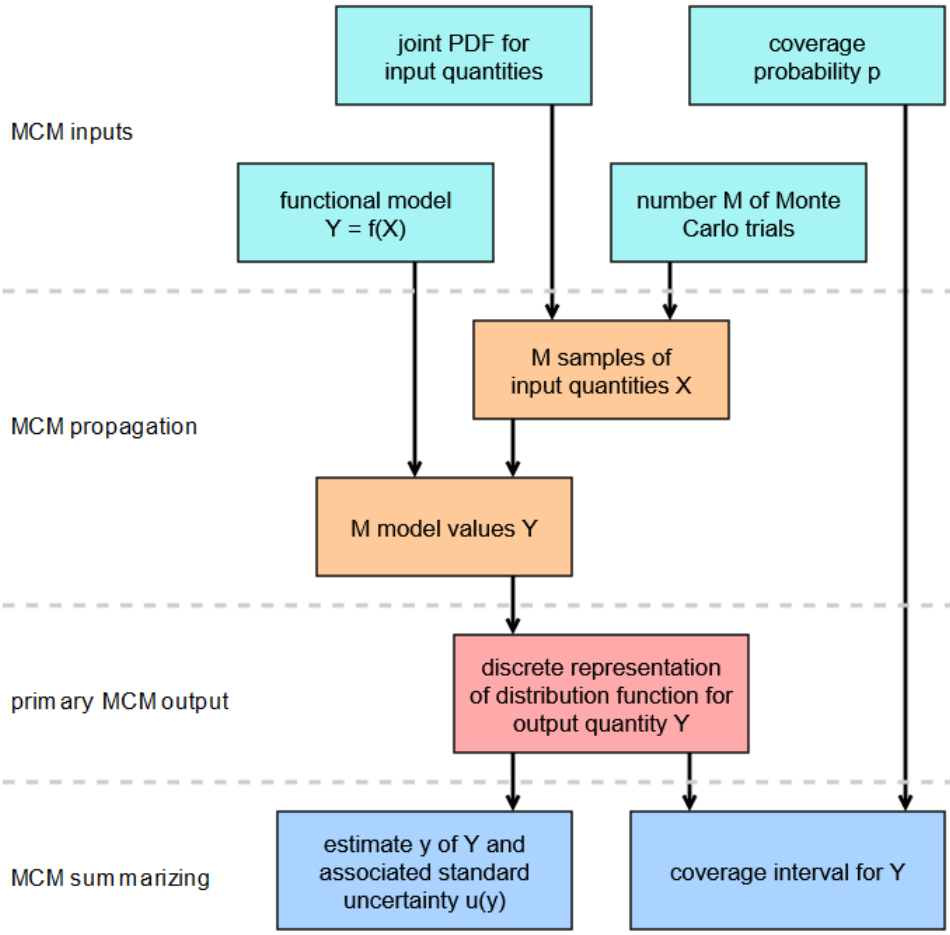

Figure 2.1.: Schematic process of uncertainty propagation using the MCM (adapted from BIPM *et al.* 2008a)

2.1.5. Statistical Test

The objective of statistical tests is to determine whether estimators agree with other independent estimators or with theoretical reference values (Niemeier 2008). Tests are conducted at a certain level of confidence which is predefined based on the desired statistical validity of the objective hypothesis. While numerous tests have been developed in the past, only two types of tests are described subsequently and will be applied in Chapter 6.

Paired Difference Test with Known Variances

This kind of hypothesis test evaluates the difference between two realisations of independent random variables with known variances of the corresponding populations. The test and its procedure is described in Niemeier (2008) and summarised subsequently.

Based on two independent, normally distributed random variables

$$X_1 \sim N_1(\mu_1, \sigma_1^2) \tag{2.35}$$

$$X_2 \sim N_2(\mu_2, \sigma_2^2) \tag{2.36}$$

the samples x_1 and x_2 exist. The variances σ_1^2 and σ_2^2 are known, while the expected values μ_1 and μ_2 are unknown.

The null hypothesis is given by Equation (2.37).

$$H_0 : \mu_1 = \mu_2 \tag{2.37}$$

The null hypothesis is modified by introducing the difference between the samples:

$$d = x_1 - x_2 \tag{2.38}$$

into Equation (2.39).

$$H_0 : E(d) = E(x_1 - x_2) = \mu_1 - \mu_2 = 0 \tag{2.39}$$

The alternative hypothesis is formulated as:

$$H_a : \mu_1 \neq \mu_2. \tag{2.40}$$

As a consequence the test is designed as a two-tailed test. Next, the test statistic y is built as Equation (2.41) shows.

$$y = \frac{x_1 - x_2}{\sqrt{\sigma_1^2 + \sigma_2^2}} \tag{2.41}$$

If the null hypothesis is valid, the test statistic value y follows a standard normal distribution. Hence the critical values for the test's outcome are looked up from tables of the standard normal distribution. The null hypothesis is not rejected if y lies in between the critical values (2.42).

$$y_{\alpha/2} \leq y \leq y_{1-\alpha/2} \tag{2.42}$$

On the other hand, the null hypothesis is rejected in favour of the alternative hypothesis if the conditions in (2.43) are true.

$$y < y_{\alpha/2} \text{ or } y > y_{1-\alpha/2} \tag{2.43}$$

F-Test

The *F*-Test is a hypothesis test suitable for determining the statistical agreement of two empirical variances or standard deviations (Riffenburgh *et al.* 2020).

Two independent samples, X_1 and X_2, are given and are both assumed to follow normal distributions. Sample X_1 has a sample variance s_1^2 calculated from n_1 observations and sample X_2 has a sample variance s_2^2 calculated from n_2 observations (Riffenburgh *et al.* 2020). The null hypothesis (2.44) expresses the equality of the expectations of the two sample variances (Niemeier 2008). The expected values of the sample variances are used as representatives for the unknown theoretical variances of the populations.

$$H_0 : E(s_1^2) = \sigma_1^2 = \sigma_2^2 = E(s_2^2) \tag{2.44}$$

In contrast, the alternative hypothesis (2.44) is formulated to set up a two-sided questioning.

$$H_a : \sigma_1^2 \neq \sigma_2^2 \tag{2.45}$$

The test statistic F is calculated as ratio of the two empirical variances, with the larger variance used as nominator. In case of $\sigma_1^2 < \sigma_2^2$, the variances are swapped without loss of generality.

Since empirical variances of normally distributed random variables follow Student's *t*-distributions, the ratio of the variances is distributed according to a Fisher-distribution with its two degrees of freedom corresponding

to the DoF of the samples. The DoF of the samples are calculated by the samples sizes minus one: $\nu_1 = n_1 - 1$, $\nu_2 = n_2 - 1$.

The critical values are taken from tables of the Fisher-distribution according to the probability error α and the two degrees of freedom. When the test statistic is within the critical values (2.46), the null hypothesis cannot be rejected at the level of confidence.

$$F_{\nu 1,\nu 2,\alpha/2} \leq F \leq F_{\nu 1,\nu 2,1-\alpha/2} \tag{2.46}$$

In contrast, the null hypothesis is rejected if F is outside the interval defined by the critical values (2.47).

$$F < F_{\nu 1,\nu 2,\alpha/2} \text{ or } F > F_{\nu 1,\nu 2,1-\alpha/2} \tag{2.47}$$

2.2. Hardware and Software

2.2.1. Hardware

The hardware section comprises the used instruments, the scanned objects and further auxiliary tools for conducting the measurements. The selection of instruments is based on the availability of equipment at the department and the comparability to related experiments, especially to those of Zámečníková *et al.* (2018) and Linzer *et al.* (2021).

Terrestrial Laser Scanner (TLS)

A modern multi station of type Leica Nova MS60 serves as terrestrial laser scanner. Its relevant technical parameters are comprised in Table 2.2. Multi stations extend the concept of total stations by additional features such as a 3D laser scanning function or GNSS connectivity (Leica Geosystems 2017). Throughout this thesis the instrument is referred to as TS(TLS) whenever the capabilities of the total station part are specifically addressed.

Parameter	Quantity
angular accuracy	
horizontal angle (Hz)	±0.3 mgon
vertical angle (V)	±0.3 mgon
distance accuracy	
onto prism	±1 mm + 1.5 ppm
onto any surface	±2 mm + 2 ppm
scan rate	30 000 Hz

Figure 2.2 & Table 2.2: Accuracy specifications (1σ-values) and technical characteristics of the used multi station Leica MS60 stated by the manufacturer (Leica Geosystems 2020).

Laser Tracker (LT)

Reference measurements are provided by a laser tracker of the model Leica LTD 800 which is compatible with a series of accessories like armless, wireless probing devices or handheld, non-contact scanners (Leica Geosystems n.d.). The primary area of application is in indoor industries and laboratories conditioned by the instrument's size and weight as well as by the bulky, essential accessories (controller, logger, power supply). For polar point determination, the laser tracker provides two methods for distance measurement. An absolute distance meter (ADM) provides absolute distance measurements. The relative distance measurement is realised by an interferometric distance meter which requires permanent visual contact to the reflector. A mirror that can be turned around two axes ensures uninterrupted angular tracking of the target (Joeckel *et al.* 2008). The laser tracker is used in combination with a Leica T-Cam 800, which is mounted on top. This device enables the recognition of orientations of probing and scanning sensors. The orientation parameters roll, pitch and yaw angle are derived by mapping active infrared-LED's of the accessories onto the CCD-array of the T-Cam (Joeckel *et al.* 2008).

Parameter	Quantity
distance measurement	
absolute accuracy	±5 µm
wave length stabilisation	±0.25 µm/m
wave length	633 nm
distance resolution	1.26 µm
angular measurements	
absolute accuracy	±5 µm/m
angular resolution	0.68 µm/m

Figure 2.3 & Table 2.3: Accuracy specifications (1σ-values) and technical properties of the used laser tracker Leica LTD 800 stated by the manufacturer (Leica Geosystems n.d.).

The laser tracker itself does not have a levelling tool (bullseye level, electronic level) for aligning the instrument horizontally. Whenever the device is set up, the laser tracker can only be aligned approximately horizontally. Hence, its polar measurements must not be viewed as perfectly levelled measurands. However, the manufacturer offers a compatible inclination sensor as upgrade accessory to the laser tracker (Hexagon Metrology 2011). Such a sensor is not used in the experiments performed for this thesis.

Handheld Scanner (HS)

The measurement of reference scans is accomplished with a handheld triangulation scanner, the Leica T-Scan TS50-A (Figure 2.4). This compact line scanner is carried along surfaces at a distance of approximately 9 cm, while being tracked by a laser tracker.

On the one hand, prisms on the scanner's outer casing allow distance measurements by the laser tracker, while on the other hand, multiple active infrared LEDs on the scanner are monitored by the T-Cam in order to compute the orientation of the scanner. The prisms and infrared transmitters are distributed over multiple sides of the scanner's cover to maximise the possible geometrical scan situations.

Parameter	Quantity
sensor accuracy	±20 µm
plane surface uncertainty	±40 µm + 1.5 µm/m
mean measuring distance	86 mm
measurement sampling rate	20 000 Hz

Figure 2.4 & Table 2.4: Accuracy specifications (1σ-values) and technical characteristics of the used handheld scanner Leica T-Scan TS50-A stated by the manufacturer (Hexagon Metrology 2013).

Corner Cube Reflector (CCR)

During network measurements, the targets are signalised by means of a corner cube reflector (CCR) with a spherical outer casing. Its technical data is outlined in Table 2.5.

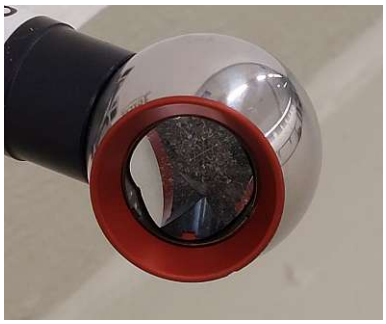

Parameter	**Accuracy** (1σ-values)
radius	±0.0025 mm
centring of optics	±0.003 mm
roundness	±0.003 mm

Figure 2.5 & Table 2.5: Specifications of Leica Red Ring Reflector 1.5″ (Hexagon Metrology 2022).

The reflector is adhered magnetically onto the consoles and is, due to its roundness, aligned unrestrictedly towards the line of sight to the respective instrument. The interior of the CCR is composed of three mirror planes perpendicular to each other with a common intersection point in the centre. For all epochs and all points the very same reflector is used.

Robot Arm (UR5)

To enhance the level of automation in data acquisition, a robot arm of the model Universal Robots UR5 is utilised. The end effector of the UR5 is linked via six rotating joints with its base (Universal Robots 2016). The relevant technical specifications are summarised in Table 2.6.

Parameter	Quantity
payload	5 kg
reach	850 mm
joint ranges	±360°
speed	joints: ≤180 °/s
	tool: ≤1 m/s
repeatability	±0.1 mm

Figure 2.6 & Table 2.6: Specifications of robot arm UR5 (Universal Robots 2016)

2.2.2. Software

Various programs and software packages are used for the acquisition and evaluation of the measurement data.

SpatialAnalyzer

This proprietary software is used for controlling and immediate visualisation of laser tracker measurements. Besides, it offers advanced tools for joining data from different sensors and analysis functions. One relevant feature for merging network measurements from different instruments, the Unified Spatial Metrology Network (USMN), is covered in detail below because it serves as a comparative algorithm to the own algorithm for network estimation.

Unified Spatial Metrology Network (USMN)

USMN is an advanced tool for combining common measurements for two or more instruments into a single instrument network. The major strengths include the calculation of the most likely position and orientation for all instruments and targets and the capability of calculating realistic uncertainties (New River Kinematics 2020).

The derivation of a USMN-composite point i.e. a point measured by different instruments, is sketched in the software manual. Measurement uncertainties usually are given relative to the instrument. In the case of instruments networked together, this simple uncertainty no longer applies, because the common point position in a networked measurement is really determined by a combination of instruments that measured the common point. In fact, the computed common point in the real world never lies on top of any of the component observations.

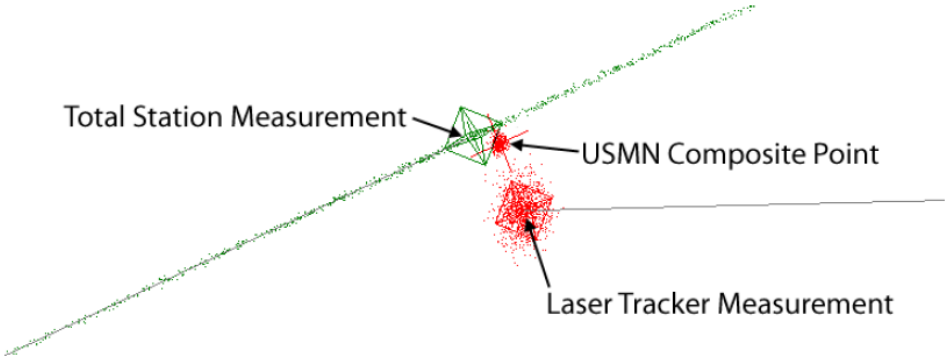

Figure 2.7.: USMN composite point. Errors between total station and laser tracker measurements are exaggerated for clarity. (taken from New River Kinematics 2020)

Referring to Figure 2.7, a total station and laser tracker have measured a common target in a nest. Due to noise, operator error and a number of other factors each instrument 'sees' the target in slightly different positions. USMN calculates the most likely position of the real target based on instrument characteristics and the uncertainty of that composite point. The composite point in Figure 2.7 is closer to the total station's line-of-sight position (due to lower angular uncertainties of total stations), but much closer to the laser tracker's distance measurement (due to less uncertainty in the laser tracker's distance measurement). Moreover, the uncertainty of the composite point itself has less uncertainty than either of the instrument observations (New River Kinematics 2020). Nonetheless, the underlying mathematical model for the combination of measurements of different instruments is not stated. The manual only reveals that an 'intelligent weighted bundle approach' is used.

Robot Operating System (ROS)

The Robot Operating System is an open source software development kit for robot applications. It provides low-level device control, implementation of commonly-used functionalities, data exchange between processes, and package management (Stanford Artificial Intelligence Laboratory et al. 2022).

Python

Python is a high-level programming language following the object-oriented programming paradigm among others and is suitable for general purposes (Python Software Foundation 2022). In this work it is used for the evaluation of observations and the quantitative analysis of uncertainties. Also the routines for propagating uncertainties through the evaluation procedure are written in python. Additionally to numerous public packages, one private package by Andreas Ettlinger, comprising object-oriented adjustment algorithms, is utilised.

CloudCompare

CloudCompare is an open source software which is mainly used for processing and visualisation of point clouds. Its application in this thesis is limited to visualisation and simple statistical analysis of scanning data.

GNU Octave

GNU Octave is a high-level programming language for scientific applications with a mathematics-oriented syntax and built-in plotting and visualisation tools (Eaton 2022). It is distributed as free software and largely compatible to MATLAB-scripts. Here, Octave is used for evaluating scan data and plotting results. Based on existing routines provided by Finn Linzer and Nortje Weise, own analysis on the scan data is accomplished.

3. ROSIAM

The term ROSIAM denotes the entirety of measurement setup, measurement procedure and measurement evaluation for determining distance differences of terrestrial laser scanners related to incidence angle and material as developed by the research unit for Engineering Geodesy at TU Wien. It can be separated into the ROSIAM system and the ROSIAM procedure. The acronym ROSIAM abbreviates the phrase Robot Operating System for investigating Incidence Angle and Material.

3.1. ROSIAM System

The collectivity of required instruments and hardware as well as their particular setup is labelled as ROSIAM system. The ROSIAM system is developed to serve as infrastructure for applying the ROSIAM procedure at a high level of automation.

The ROSIAM system, at this stage of development, is realised in the research unit's measurement facility at campus Gußhaus. The laboratory room (Figure 3.1) offers virtually unrestricted line of sights across its dimensions of approximate 55 × 6 × 3.5 m. Furthermore, it offers steady ambient atmospheric conditions.

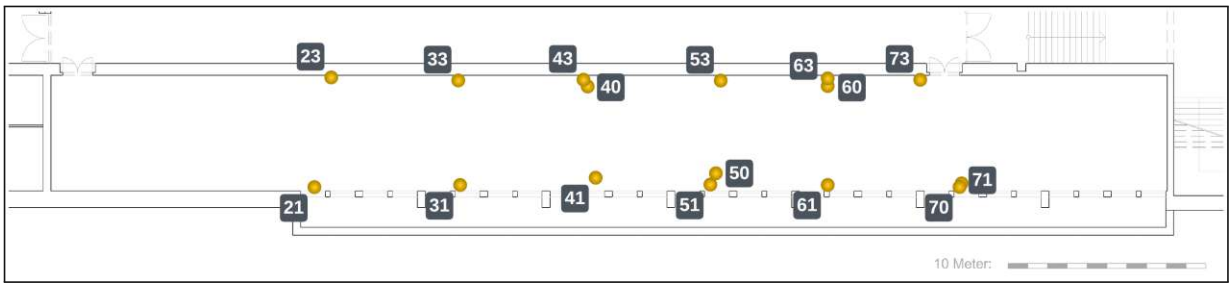

Figure 3.1.: Floor plan of the measurement laboratory (GUT TU Wien). The target points, realising a high-accuracy network, are highlighted and attached with their target names.

3.1.1. High-Accuracy Network

One essential part of the ROSIAM system is the availability of a set of stable and precisely reproducible points. Since the laboratory offers existing points that meet these requirements, these points are employed for the ROSIAM system. In total 16 targets are used. The basis for the network is formed by consoles mounted at different heights on the walls and by brackets integrated in the floor of the laboratory (Figure 3.2). Each console is completed by a magnetic nest which adheres the reflector during measurements in order to physically realise a network point.

(a) wall console (b) floor console (c) console with reflector

Figure 3.2.: A spherical reflector inserted at consoles realises a point of the high-accuracy network.

3.1.2. Instrument Setup

Figure 3.3 provides an overview on the instrument setup utilised in the ROSIAM system. The laser tracker (LT) is located centrally in the high-accuracy network. Scan object and robot arm (UR5) are placed close to each other to enable close range reference scans by the handheld scanner (HS), which is attached at the end effector of the robot arm (UR5). The terrestrial laser scanner (TLS) is mounted onto a massive pillar at a distance of approximate 30 m to the object. Hence, the TLS is located slightly eccentrically in relation to the network. The scan object is fixed on a rotary plate, whose orientation is modifiable by a small stepping motor chained to it. Vertical alignment of the plate is ensured via auto-collimation by the TS(TLS) by means of a mirror attached to the plate. Considering this setup, the object plate can only be rotated around its vertical axis, which is employed to realise different incidence angles. All hardware components are integrated into a Robot Operating System-framework which coordinates the measurement procedures and data flow.

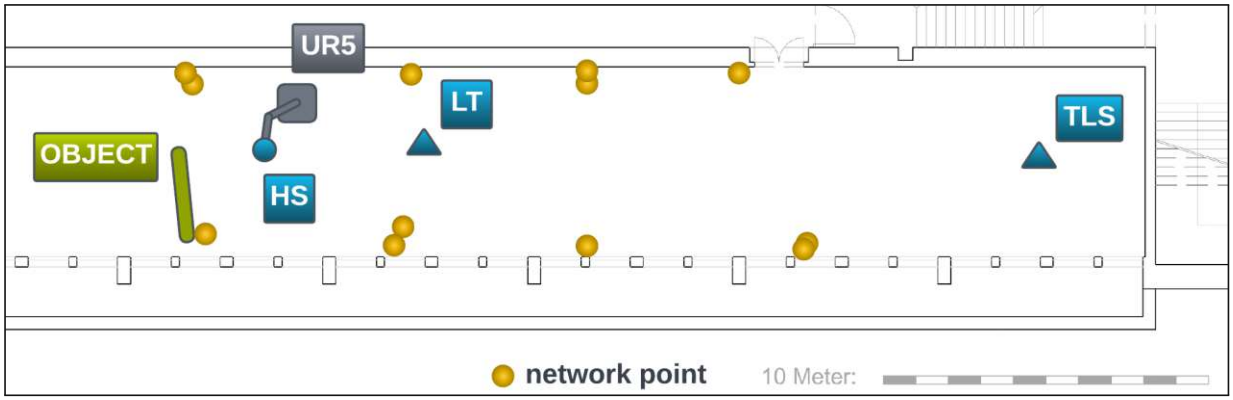

Figure 3.3.: Overview of the geometrical measurement setup of ROSIAM system.

3.2. ROSIAM Procedure

ROSIAM procedure terms the conduction of measurements utilising the ROSIAM system and the following evaluation of the measurements. The aim of these measurements is to generate absolute distance differences ΔD by determining the difference between a highly accurate reference distance D_{ref} against the measured distance to single scan points of the terrestrial laser scanner D_{TLS}. The methodology of systematic, largely automatised data acquisition is summarised as a flow diagram in Figure 3.4. It is designed to provide data for

one material per epoch. The process is composed of a manually conducted network measurement and the ROS controlled scan measurements.

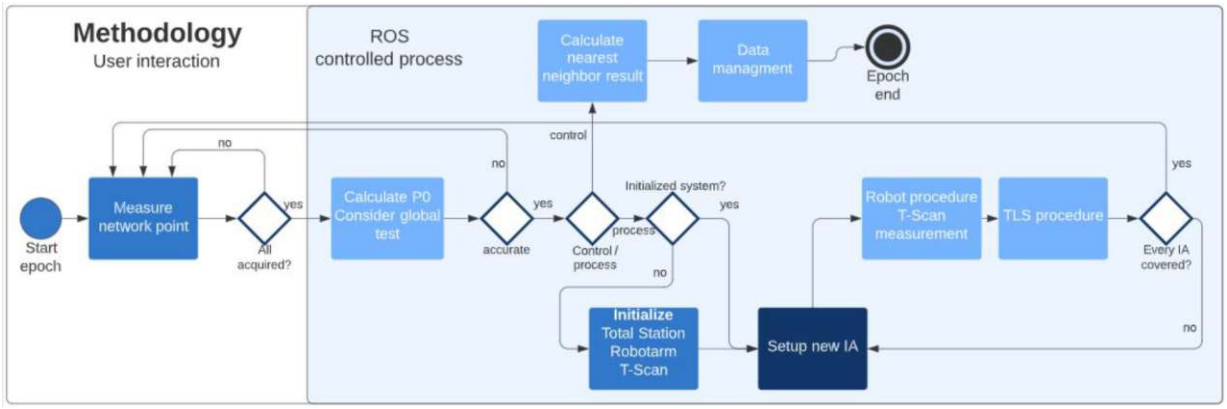

Figure 3.4.: Flow diagram of the measurement part of ROSIAM procedure (taken from: Linzer *et al.* (2021))

3.2.1. Network Measurement

The network measurement comprises the quasi-simultaneous measurements of laser tracker and total station (terrestrial laser scanner) to multiple network points (Figure 3.5). The aim of the network measurement is to produce data that allow the derivation of a spatial relationship between LT and TS(TLS). Network points are realised by a corner cube reflector (CCR) which is magnetically held in consoles provided for this purpose. The coordinates of the individual network points are determined by the laser tracker by interferometry and in precise mode. Therefore, the CCR is manually moved from the laser tracker's home point (birdbath) to the particular console without interrupting the line-of-sight to the laser tracker. After the LT measurement, the CCR is oriented towards the total station without removing it and measurements in two faces with manual aiming are performed. These tasks are repeated for ca. 8 to 10 targets. Automation of these steps is currently not possible, since automatic measuring functions like automatic target recognition (ATR) do not yet meet the required standards (Linzer *et al.* 2021). For fully automated routines also multiple reflectors with automated alignment towards the measuring instrument would be necessary not to mention the interferometric distance measurement which needs continuous sights to the targets.

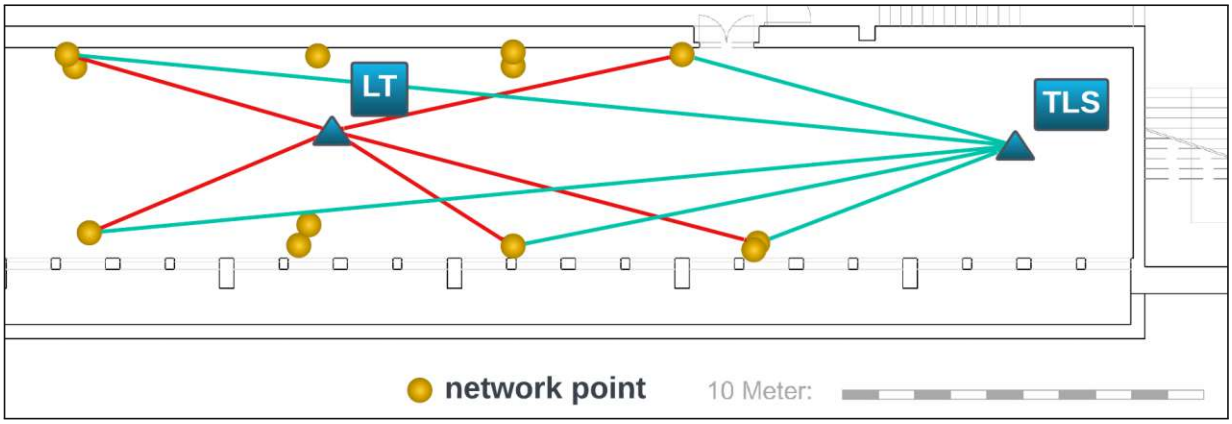

Figure 3.5.: Quasi-simultaneous measurements to common network measurements enable the derivation of a spatial relationship between LT and TS(TLS).

3.2.2. Network Evaluation

The two-faced TS measurements are averaged and checked for outliers. The main step is then the computation of transformation parameters between the laser tracker's coordinate system and the coordinate system of the total station (terrestrial laser scanner). This is done either by the function Unified Spatial Metrology Network (USMN) in SpatialAnalyzer (see Chapter 2.2.2) or by a Helmert transformation as detailed in Chapter 4. If the uncertainty of the derived transformation parameters is in the context of expectations, the ROSIAM procedure continues.

3.2.3. Scan Measurement

Following the network evaluation, the ROSIAM system is initialised for the scan procedure. This includes connection checks to all required hardware components (LT, HS, TLS, UR5, stepping motor) and the setting of initial values. Furthermore, scan parameters such as the scan rate are defined as well as the area of scanning which is typically 10 cm × 20 cm large. One important task is to ensure that the laser tracker successfully 'finds' the prisms of the handheld scanner. A new incidence angle of the object related to the laser beam of the TLS is set up. Then a reference scan is measured with the handheld scanner which in turn is being tracked by the laser tracker. Panning the handheld scanner in optimal distance to the object is done by the robot arm (Figure 3.7). This procedure takes less than one minute and generates approximately 1 million points for one reference scan. Then the master program in ROS triggers the TLS via the geocom interface to start its scan routine. The TLS scan lasts a few minutes and acquires about 3000 points. Subsequently, the next incidence angle is set up and both scanning routines restart. The scan configuration is illustrated in Figure 3.6.

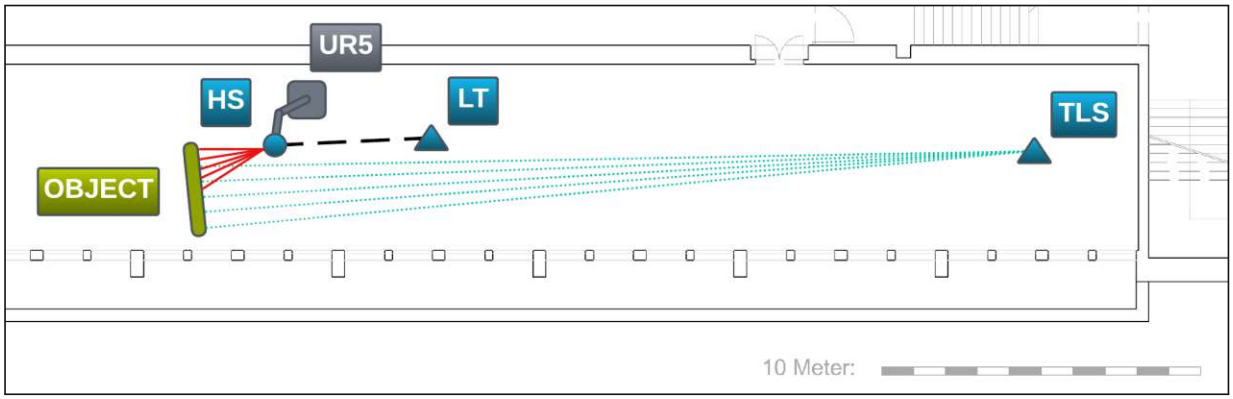

Figure 3.6.: Scan configuration of the ROSIAM procedure.

A single measuring epoch that examines up to 31 different incidence angles requires up to 10 h as stated in Linzer *et al.* (2021). In addition, the measuring devices should be turned on 3 h in advance to ensure the recommended warm-up time. Hence, the demands on the measuring equipment and the observer are very high due to the high accuracy to be called for and the duration.

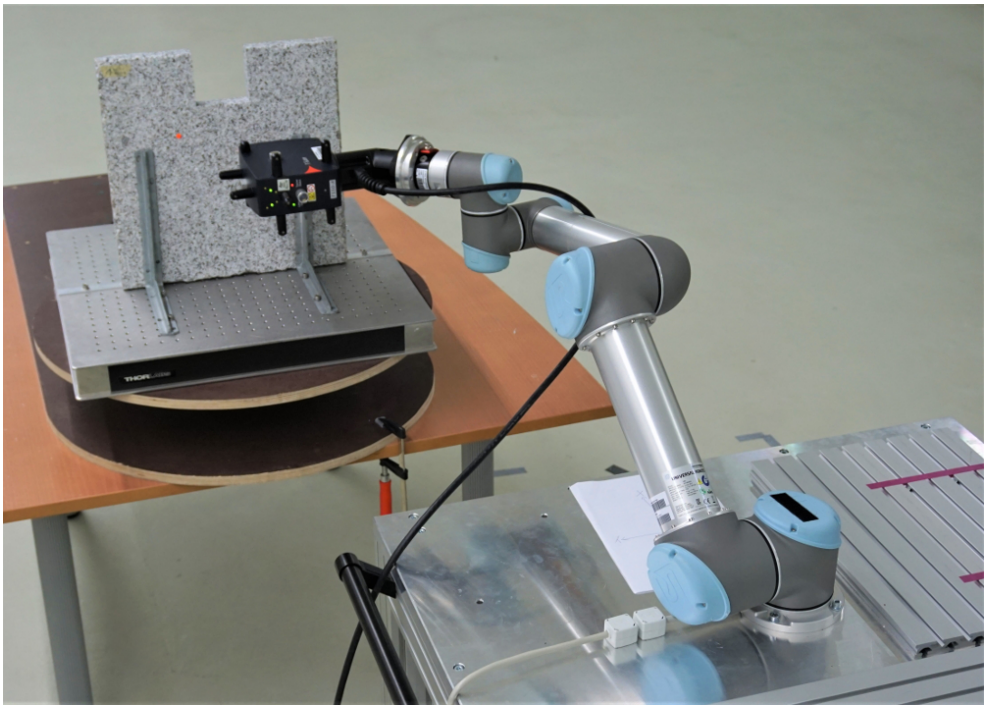

Figure 3.7.: Robot arm panning the HS along the object plate for the acquisition of a reference point cloud.

3.2.4. Scan Evaluation

In an automated routine, the measured point clouds are transformed into one joint coordinate system with the origin at the zero-point of the TS(TLS). The required transformation parameters are already estimated in the network evaluation (Chapter 3.2.2). Points that represent surfaces apart from the predefined scan area on the object plate are filtered out. Polar coordinates with respect to the same origin now enable direct comparison of reference distances D_{ref} and measured TLS distances D_{TLS} and are termed distance differences ΔD_i (3.1).

$$\Delta D_i = D_{ref,i} - D_{TLS,i} \tag{3.1}$$

To compute distance differences, TLS points and corresponding reference points need to be matched. Appropriate points are mapped by the least deviation in rheir polar coordinates (ΔHz and ΔV) while introducing limits to these angle deviations. Each point of the TLS scan is mapped to exactly that point of the reference scan, that fulfils the conditions (3.2) and (3.3). For enhancing computation efficiency, the search of point pairs is structured in a k-d tree.

$$\begin{aligned} \lim_{\Delta Hz \to 0} Hz_{TLS,i} + |\Delta Hz| &\widehat{=} Hz_{ref,i} \\ \lim_{\Delta V \to 0} V_{TLS,i} + |\Delta V| &\widehat{=} V_{ref,i} \end{aligned} \tag{3.2}$$

$$\sqrt{\Delta Hz^2 + \Delta V^2} < 0.1\,\text{mgon} \tag{3.3}$$

This mapping is neither injective nor surjective because of the maximum permissible angle deviation of 0.1 mgon and the different number of scan points. Between 200 and 600 correspondences can be assigned for each IA with that procedure.

Finally, the mean over all distance differences is computed per incidence angle (3.4) along with its standard deviation (3.5).

$$\Delta D_m = \sum_{i=1}^{n} \frac{\Delta D_i}{n} \tag{3.4}$$

$$\sigma_{\Delta D_m} = \sqrt{\sum_{i=1}^{n} \frac{(\Delta D_m - \Delta D_i)^2}{n(n-1)}} \tag{3.5}$$

4. Development of a Model for Network Transformation

In this chapter the development of a network transformation model for the transformation between the coordinate systems of a laser tracker and a total station is described. The objective of the model is to derive transformation parameters by joining measurements of both instruments. The development is done in due consideration of the subsequent premises.

- Integration of raw spherical measurands
- No restrictions to the instruments' orientations
- Avoidance of the requirement of approximate values
- Consideration of uncertainty information of all measurands
- Continuous differentiability in order to permit the application of common linearisation algorithms
- Design that allows ranked variance component analysis

4.1. Transformation Model

As basis for the network transformation serves the three-dimensional Helmert transformation. The transformation function of this similarity transformation is denoted in matrix notation for two right-handed systems (Niemeier 2008):

$$\boldsymbol{x} = \boldsymbol{t} + m \cdot \boldsymbol{R}(\omega, \varphi, \kappa)\, \boldsymbol{x'} \tag{4.1}$$

The shifting vector $\boldsymbol{t}$ with its elements t_x, t_y, t_z represents the translation between the origins of the coordinate systems. The rotation is determined by the rotation matrix $\boldsymbol{R}$, which is a function of the rotation angles ω, φ and κ around the coordinate axis of the primed coordinate system. The factor m acts as a scale factor. For this application, source coordinates (x', y', z') are laser tracker coordinates and target coordinates (x, y, z) are TS(TLS) coordinates. The seven transformation parameters $(t_x, t_y, t_z, \omega, \varphi, \kappa$ and $m)$ apply to the transformation direction from the LT-frame to the TS(TLS)-frame.

Instead of keeping the product of scale factor and rotation matrix $(m\boldsymbol{R})$ as a function of the geometrically descriptive Euler angles, the rotation matrix $\boldsymbol{Q}$ as function of a quaternion is used (4.4). A quaternion q is a hypercomplex number that follows the pattern as shown in Equation (4.2) (Kramer *et al.* 2022).

$$q = q_0 + q_1 i + q_2 j + q_3 k \quad with \;\; q_0, q_1, q_2, q_3 \in \mathbb{R} \tag{4.2}$$

and with the essential condition

$$i^2 = j^2 = k^2 = i \cdot j \cdot k = -1 \tag{4.3}$$

Quaternions can be viewed as an extension of complex numbers. If the scalars in (4.2) are arranged in a matrix as depicted in (4.4), the matrix $\boldsymbol{Q}$ serves as transformation matrix in 3D and is equivalent to the product $m\boldsymbol{R}$ (Kramer *et al.* 2022; Vince 2022).

$$\boldsymbol{Q}(q_0,q_1,q_2,q_3) = \begin{bmatrix} q_0^2+q_1^2-q_2^2-q_3^2 & 2\,(q_1q_2-q_0q_3) & 2\,(q_1q_3+q_0q_2) \\ 2\,(q_1q_2+q_0q_3) & q_0^2-q_1^2+q_2^2-q_3^2 & 2\,(q_2q_3-q_0q_1) \\ 2\,(q_1q_3-q_0q_2) & 2\,(q_2q_3+q_0q_1) & q_0^2-q_1^2-q_2^2+q_3^2 \end{bmatrix} \tag{4.4}$$

Replacing the Cartesian coordinates in (4.1) by the spherical measurands (horizontal angle Hz, vertical angle V, distance d) and using the transformation matrix $\boldsymbol{Q}$ leads to:

$$\begin{bmatrix} d_{TLS}\sin(V_{TLS})\sin(Hz_{TLS}) \\ d_{TLS}\sin(V_{TLS})\cos(Hz_{TLS}) \\ d_{TLS}\cos(V_{TLS}) \end{bmatrix} = \begin{bmatrix} t_x \\ t_y \\ t_z \end{bmatrix} + \boldsymbol{Q} \begin{bmatrix} d_{LT}\sin(V_{LT})\cos(Hz_{LT}) \\ d_{LT}\sin(V_{LT})\sin(Hz_{LT}) \\ d_{LT}\cos(V_{LT}) \end{bmatrix} \tag{4.5}$$

4.2. Adjustment Model

Since overdetermination is assumed, the merging of a transformation model (4.1) into an adjustment model is necessary. For the adjustment of a Helmert transformation, the Gauss-Markov model is used, which induces the limitation that coordinates of just one system act as observations while those of the other (reference) system are considered to be fixed constants (Niemeier 2008). To account for the uncertainties in the coordinates of both systems due to imperfect measurements, the Gauss-Helmert model (2.3) is applied instead for the adjustment.

The transformation function in (4.5) is adopted as functional adjustment model and shown in Equation (4.6) for one network point i.

$$\psi_{p,i}(\boldsymbol{L}_i,\boldsymbol{X}): \begin{bmatrix} d_{TLS,i}\sin(V_{TLS,i})\sin(Hz_{TLS,i}) \\ d_{TLS,i}\sin(V_{TLS,i})\cos(Hz_{TLS,i}) \\ d_{TLS,i}\cos(V_{TLS,i}) \end{bmatrix} - \begin{bmatrix} t_x \\ t_y \\ t_z \end{bmatrix} - \boldsymbol{Q} \begin{bmatrix} d_{LT,i}\sin(V_{LT,i})\cos(Hz_{LT,i}) \\ d_{LT,i}\sin(V_{LT,i})\sin(Hz_{LT,i}) \\ d_{LT,i}\cos(V_{LT,i}) \end{bmatrix} = \boldsymbol{0} \tag{4.6}$$

The vector of observations is built of the spherical measurands: $\boldsymbol{L}_i = [d_{TLS,i}, Hz_{TLS,i}, V_{TLS,i}, d_{LT,i}, Hz_{LT,i}, V_{LT,i}]^T$. The transformation parameters are condensed in the vector of unknowns: $\boldsymbol{X} = [t_x, t_y, t_z, q_0, q_1, q_2, q_3]^T$. The functional model is extended by the conditional equation (4.7). This condition is equivalent to fixing the scale factor m in (4.1) to 1. Background for this essential condition is to preempt a scaling of the networks to each other by the adjustment. The estimation of a scale factor would interfere a proper uncertainty propagation of the measured distances.

$$\psi_c(\boldsymbol{X}): \; q_0^2+q_1^2+q_2^2+q_3^2-1=0 \tag{4.7}$$

The complete model for n network points is given in Equation (4.8).

$$\psi(\boldsymbol{L}_1,\boldsymbol{L}_2,\ldots,\boldsymbol{L}_n,\boldsymbol{X}) = \begin{bmatrix} \psi_{p,1}(\boldsymbol{L}_1,\boldsymbol{X}) \\ \psi_{p,2}(\boldsymbol{L}_2,\boldsymbol{X}) \\ \vdots \\ \psi_{p,n}(\boldsymbol{L}_n,\boldsymbol{X}) \\ \psi_c(\boldsymbol{X}) \end{bmatrix} \tag{4.8}$$

The solution of the seven parameters requires at least two 3D points plus one height point. In the performed measurement campaigns all points are recorded as 3D points. Therefore, three 3D points are sufficient for an unambiguous solution. Due to the utilisation of a quaternion, no approximate values for the unknowns are required. Instead the transformation parameters for an identity transformation are used as initial values:

$$\begin{bmatrix} t_x \\ t_y \\ t_z \\ q_0 \\ q_1 \\ q_2 \\ q_3 \end{bmatrix} = \begin{bmatrix} 0 \\ 0 \\ 0 \\ 1 \\ 0 \\ 0 \\ 0 \end{bmatrix} \tag{4.9}$$

Equation (4.10) shows the implemented stochastic model, which is directly taken from the Helmert transformation model.

$$\boldsymbol{\Sigma}_{ll} = \frac{1}{\sigma_0^2}\boldsymbol{Q}_{ll} = \frac{1}{\sigma_0^2}\begin{bmatrix} \boldsymbol{Q}_{Hz,TLS} & & & & & & \\ & \boldsymbol{Q}_{V,TLS} & & & & & \\ & & \boldsymbol{Q}_{d,TLS} & & & & \\ & & & \boldsymbol{Q}_{Hz,LT} & & & \\ & & & & \boldsymbol{Q}_{V,LT} & & \\ & & & & & \boldsymbol{Q}_{d,LT} \end{bmatrix} \tag{4.10}$$

The submatrices in (4.10) are diagonal matrices of the same size and in identical order of the values corresponding to the network points. The sorting of the observations by observation type enables a simplified implementation of variance component analysis, termed as ranked variance component analysis. As a consequence, the observations need to be arranged in the same order as the corresponding cofactors in (4.10). Thus, the vector of observations is formulated like (4.11).

$$\boldsymbol{L} = [Hz_{TLS,1}, \dots, Hz_{TLS,n}, V_{TLS,1}, \dots, V_{TLS,n}, d_{TLS,1}, \dots, d_{TLS,n}, Hz_{LT,1}, \dots, Hz_{LT,n}, V_{LT,1}, \dots, V_{LT,n}, d_{LT,1}, \dots, d_{LT,n}]^T \tag{4.11}$$

5. Quantification of Uncertainties in ROSIAM

This chapter deals with the compilation of individual sources of uncertainty that occur throughout the entire process of deriving distance differences with the ROSIAM methodology. Relevant sources of uncertainty are detected, their magnitudes are estimated and their impacts on quantities along the process are computed. Finally, the overall effect on the uncertainty of distance differences $u_{\Delta D}$ is determined. For some influence factors, uncertainty information of Type A (by experiments), for others uncertainty information of Type B (from data sheets) is available.

5.1. Overview

The fishbone diagram in Figure 5.1 gives an comprehensive, structured overview on the variety of presumed sources of uncertainty.

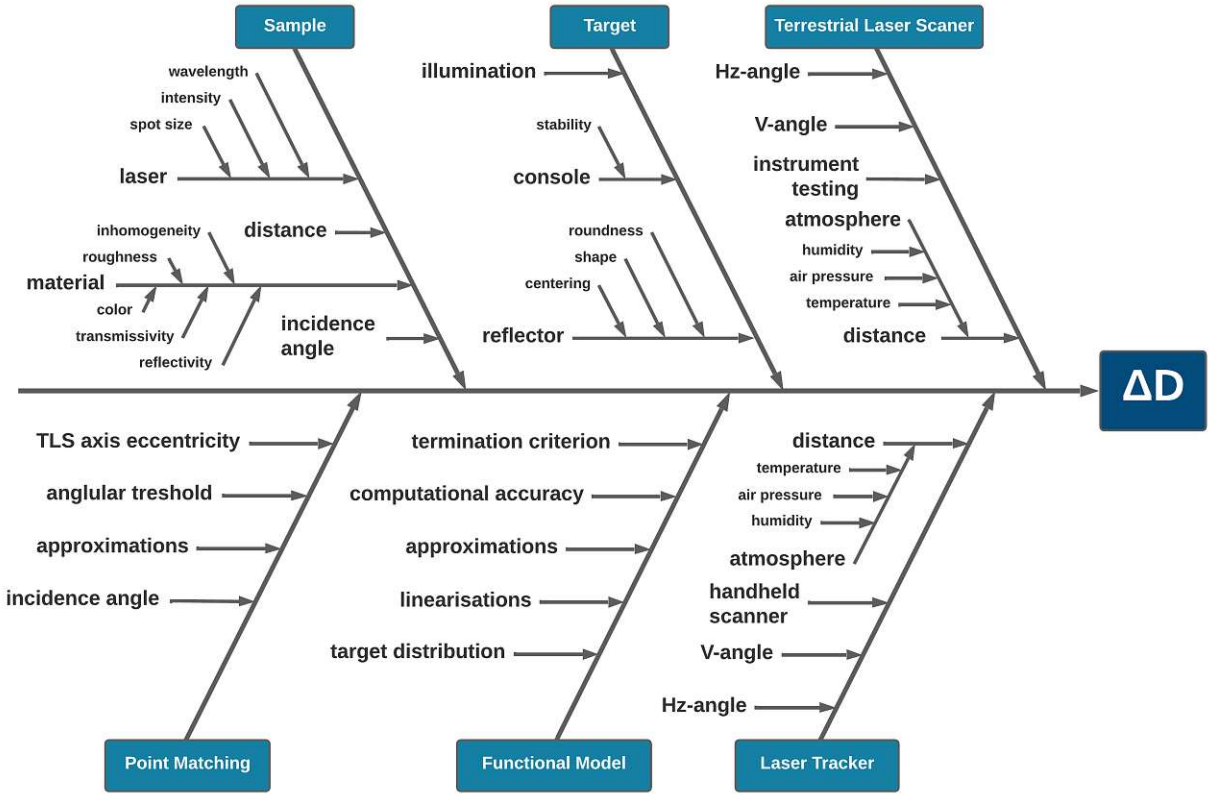

Figure 5.1.: Fishbone diagram listing sources of uncertainty which are relevant for the determination of the uncertainty of distance differences ΔD

As can be seen, not only the instrumental equipment act as sources of uncertainty, but also the measuring objects, the high-accuracy network and the entire laboratory environment. In addition, the used functional models and mathematical simplifications play a role in the determination of the uncertainty of distance differences. In the following sections the individual contributing factors are covered in detail. One exception is the sample topic and its subitems whose uncertainties are not estimated but analysed in Chapter 6. The reason for this is that the influence behaviour of the sample and its physical properties are not yet fully known and are therefore subject of further investigations in the Engineering Geodesy research unit. However, quantification of all other sources of uncertainty serves as basis for future data-driven derivations of relationships between distance differences and sample properties.

Measurement Campaigns

Table 5.1 lists the relevant measurement campaigns in chronological order. The aim of the listed experiments is to quantify individual influencing factors.

Table 5.1.: Overview on the performed measurement campaigns.

Data Set ID	Date	Types of Measurement	Instruments
1	03.2021	aiming accuracy	TLS
2	03.2021	network measurement	LT, TS(TLS)
3*	03.2021	ROSIAM campaign *'MS60'*	LT, TLS, HS
4	04.2021	network measurement	LT, TS(TLS)
5	05.2021	repeatability, comparability	LT
6	05.2021	CCR accuracy	LT
7*	08.2021	ROSIAM campaign *'Klinker'*	LT, TLS, HS
8	02.2022	network measurement, object scans	LT, TLS, HS
9*	03.2022	ROSIAM campaign *'Rauigkeit'*	LT, TLS, HS

*performed/provided by my supervisor Finn Linzer

5.2. Measurand Preprocessing

In order to comprehensively capture the effects of the uncertainties of the observations, the quantification and propagation of uncertainties begins at the raw measurement stage.

Terrestrial Laser Scanner

The raw network measurements of the TS(TLS) are recorded in two faces and consist of horizontal angles Hz, vertical angles V and distances d. In the first step, all measurements to the network points in two faces are averaged according to Gruber *et al.* (2014):

$$\begin{aligned} \overline{V} &= \frac{V_I + (400 - V_{II})}{2} \\ \overline{Hz} &= \frac{Hz_I + (Hz_{II} \pm 200)}{2} \\ \overline{d} &= \frac{d_I + d_{II}}{2} \end{aligned} \tag{5.1}$$

The standard uncertainty of the averaged measurands is therefore derived from the standard uncertainties of the manufacturers, assuming uncorrelated measurements (5.2).

$$\begin{aligned} \sigma_{\overline{V}} &= \frac{\sigma_V}{\sqrt{2}} \\ \sigma_{\overline{Hz}} &= \frac{\sigma_{Hz}}{\sqrt{2}} \\ \sigma_{\overline{d}} &= \frac{\sigma_d}{\sqrt{2}} \end{aligned} \tag{5.2}$$

Possible gross errors in the TS(TLS) network measurements are detected by comparing the differences between face averages and original face measurements against threshold levels. This increases the reliability of the derived uncertainties in (5.2). Equation (5.3) shows the conditions for outliers and the used thresholds.

$$\begin{aligned} |V_I - \overline{V}| &> 1.0\,[mgon] \\ |Hz_I - \overline{Hz}| &> 1.0\,[mgon] \\ |d_I - \overline{d}| &> 1.0\,[mm] \end{aligned} \tag{5.3}$$

Exceeding at least one of the outlier thresholds leads to the exclusion of the entire network point. The threshold values are chosen based on the results of the experiments in Chapter 5.8 and the instrument's accuracy stated by the manufacturer (see Leica Geosystems 2020).

Laser Tracker

The laser tracker measurements are output as Cartesian coordinates. However, uncertainty information is provided by the manufacturer for the spherical LT measurands exclusively. Consequently, the original spherical measurands (horizontal angle Hz_{LT}, vertical angle V_{LT}, distance d_{LT}) are restored. Equation (5.4) displays the transformation of the right-handed Cartesian coordinates provided by the measurement software into the spherical measurands (Dietmaier 2014).

$$\begin{aligned} d_{LT} &= \sqrt{x_{LT}^2 + y_{LT}^2 + z_{LT}^2} \\ Hz_{LT} &= \arctan\left(\frac{y_{LT}}{x_{LT}}\right) \\ V_{LT} &= \arccos\left(\frac{z_{LT}}{\sqrt{x_{LT}^2 + y_{LT}^2 + z_{LT}^2}}\right) \end{aligned} \tag{5.4}$$

For laser tracker measurements, the detection of outliers in the same manner as for the TS(TLS) measurements is not possible due to the lack of redundancy. Measurements of the laser tracker are available in the first face only since there is no concept of two face measurements for the used instrument. Measurements of the network points are realised by cautiously inserting the retroreflector into the consoles while the instrument is continuously tracking the reflector. In that sense, no manual aiming is conducted and hence the likelihood of outliers in LT measurements is diminished.

5.3. Atmospheric Correction

Distance measurements with lasers are usually affected by the atmosphere in two ways: The propagation speed is influenced via the refractive index of the medium and the geometric shape of the path is perturbed by the refraction (Joeckel *et al.* 2008). The latter effect is ignored since a constant atmosphere is assumed in space and the distances involved are small. The key parameters characterising the medium, i.e. the atmosphere in this particular respect, are temperature t, total pressure p and partial water vapour pressure e or alternatively relative humidity R. These parameters are set in the instruments' settings at the beginning of the measurements in order to correct distances automatically. The atmospheric conditions in the laboratory are recorded by a meteorological station of the model HM30. Its specifications are shown in Table 5.2.

Table 5.2.: Specifications of the used meteorological station Thommen HM30 (Revue Thommen AG n.d.).

Parameter	**Measuring range**	**Resolution**	**Accuracy** (1σ)
barometric pressure	225 ... 1125 hPa	0.1 hPa	±0.4 hPa
humidity	0 ... 100 %rH	0.1 %rH	±0.9 %rH
temperature	-40 ... 60 °C	0.1 °C	±0.2 °C
altitude	-500 ... 10 000 m	1 m	±2 m

The measured atmospheric parameters are therefore attached with uncertainties of type A. The calculation of the impact of the uncertainty of the atmospheric parameters on the uncertainties of the measured distances is achieved by variance propagation. Unfortunately, the intern atmospheric correction algorithms are unknown for both instruments. Hence, the correction formulas for electronic distance measurements (EDM) provided by the International Association of Geodesy (IAG) are applied surrogate. Divergences to the actually used algorithms in the instruments are assumed to be small and with neglectable impact. Equations (5.7) and (5.8) show the distance correction algorithm that is proposed by the IAG in its resolution from 1999 (IAG 1999). To consider the frequency dependency, also the laser's wavelength λ acts as input parameter for the correct distance correction. Since the outputs of the used meteorological station are temperature, atmospheric pressure and relative humidity, the first step is the derivation of the partial water vapour pressure e (Joeckel *et al.* 2008).

$$e = R \cdot \frac{E}{100} \tag{5.5}$$

with E as maximum humidity for air

$$E = 10^{\left(\frac{7.5 \cdot t}{237.3 + t} + 0.78571\right)} \tag{5.6}$$

The wavelength λ determines the group refractive index n_{Gr} for dry standard atmosphere ($t = 273.15\,\mathrm{K}$, $p = 1013.25\,\mathrm{hPa}$, CO_2-content $= 0.0375\,\%$ and $e = 0.0\,\mathrm{hPa}$)

$$N_{Gr} = (n_{gr} - 1) \cdot 10^6 = 287.6155 + \frac{4.88660}{\lambda^2} + \frac{0.06800}{\lambda^4}. \tag{5.7}$$

According to Joeckel *et al.* (2008), the reduction from standard atmosphere to actually prevalent atmosphere is achieved by the relationship in (5.8).

$$N_L = (n_L - 1) \cdot 10^6 = n_{Gr} \cdot \frac{273.15}{1013.25} \cdot \frac{p}{t} - \frac{11.27}{t \cdot e}. \tag{5.8}$$

The atmospherically corrected distance d is finally calculated as shown in Joeckel *et al.* (2008) via (5.9).

$$d = d_0 \frac{n_{L0}}{n_L} \tag{5.9}$$

There, n_{L0} is the refractive index for standard air and n_L the refractive index for the mean atmosphere in the laboratory at ($t = 293.15\,\text{K}$, $p = 1013.25\,\text{hPa}$, $\varphi = 35\,\%$ relative humidity). According to the law of uncertainty propagation (2.27), the respective contribution to the uncertainty of the measured distances is calculated. The resulting standard uncertainties are $u_{d,LT}$ =1.90 µm/m and $u_{d,TLS}$ =1.94 µm/m for the laser tracker and the terrestrial laser scanner, respectively. These factors are considered when propagating uncertainties further in the Monte Carlo method.

5.4. Reflector

Three kinds of experiments are performed specifically to address the uncertainty of the CCR in combination with the measurement uncertainty of the laser tracker. All of them consist of laser tracker measurements to the reflector. The aim of these experiments is to check whether the accuracy specifications of the CCR are met.

CCR Repeatability

In this experiment, the CCR remains in the console while being tracked by the LT ten times with time intervals of approximately one minute in between. These kind of measurements, where multiple measurements are performed over a short period of time with constant conditions are denoted as repeatability measurements (BIPM *et al.* 2008b). In total, ten different targets are measured consecutively in this procedure in order to increase statistical validity. As a visualisation for repeatability, Figure 5.2 displays the dispersion of the measurements around their individual mean values for horizontal angles, vertical angles and distances. The term repeatability in this section refers to the combination of the laser tracker and the reflector as a clear delimitation is not possible. The results of this experiment bear also limited validity on the stability of the target consoles. The derived standard uncertainties of $\sigma_{Hz,LT,repeat} = 0.07\,\text{mgon}$, $\sigma_{V,LT,repeat} = 0.05\,\text{mgon}$ and $\sigma_{d,LT,repeat} < 0.1\,\mu\text{m/m}$ as representatives for the dispersion of values clearly undercut the specifications of the manufacturer of $\sigma_{Hz,LT,manu} = 0.16\,\text{mgon}$, $\sigma_{V,LT,manu} = 0.16\,\text{mgon}$ and $\sigma_{d,LT,manu} = 0.25\,\mu\text{m/m}$ (Leica Geosystems n.d.).

CCR Reproducibility

In contrast to the previously described experiment, to ascertain the reproducibility, the reflector is reinserted into the magnetic console. Each measurement procedure starts with a distance initialisation by the absolute distance meter at the laser tracker's home point. This home point is a console for the CCR at the base of the LT (Joeckel *et al.* 2008). Then the CCR is moved to the target console under continuous tracking, where the final distance is logged. This procedure is repeated nine times for in total ten different targets. After checking for outliers, the measurements are reduced by their mean values and plotted comparably in Figure 5.3. The standard uncertainties $\sigma_{Hz,LT,reprod} = 0.08\,\text{mgon}$, $\sigma_{V,LT,reprod} = 0.07\,\text{mgon}$ and $\sigma_{d,LT,reprod} = 0.3\,\mu\text{m/m}$ do not exceed the standard uncertainties stated by the manufacturer or are in a comparable range: $\sigma_{Hz,LT,manu} = 0.32\,\text{mgon}$, $\sigma_{V,LT,manu} = 0.32\,\text{mgon}$ and $\sigma_{d,LT,manu} = 2.5\,\mu\text{m/m}$.

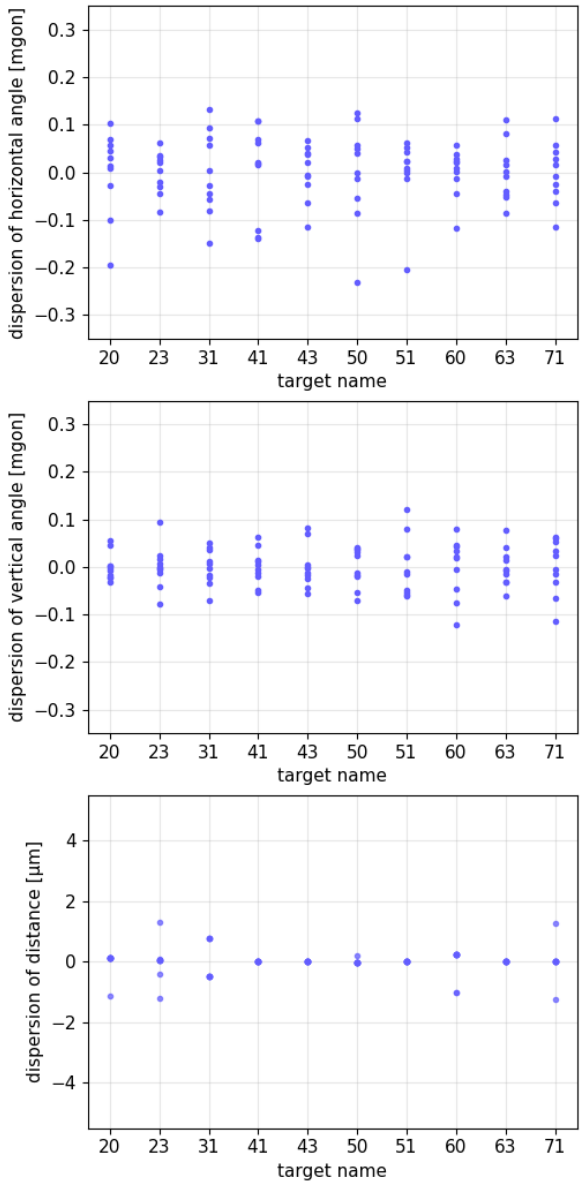

Figure 5.2.: Repeatability of LT measurements on CCR target.

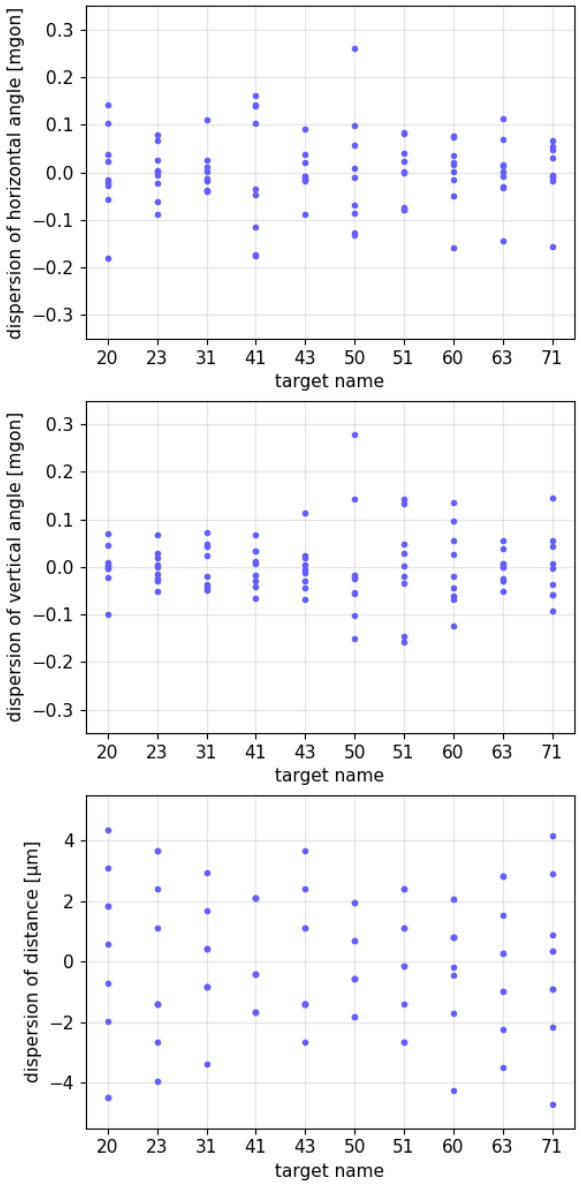

Figure 5.3.: Reproducibility of LT measurements on CCR target.

CCR Roundness

To determine eventual damages of the CCR or deviations from its spherical shape, the following experiment is carried out. The CCR is placed at a target console, aligned towards the LT and oriented upwards with its branding, as depicted in Figure 5.4. After triggering a measurement, the CCR is rotated around the line of sight clockwise by ca. 50 gon (looking towards the CCR) and the next measurement is triggered. This procedure is repeated until the CCR is turned for a full circle. This experiment is repeated for seven different targets, to achieve statistical validity and to cover all sides of the CCR. Figure 5.5 depicts the dispersion of the measurements with respect to the rotation angle of the reflector. The measurements are reduced by the mean value for each target.

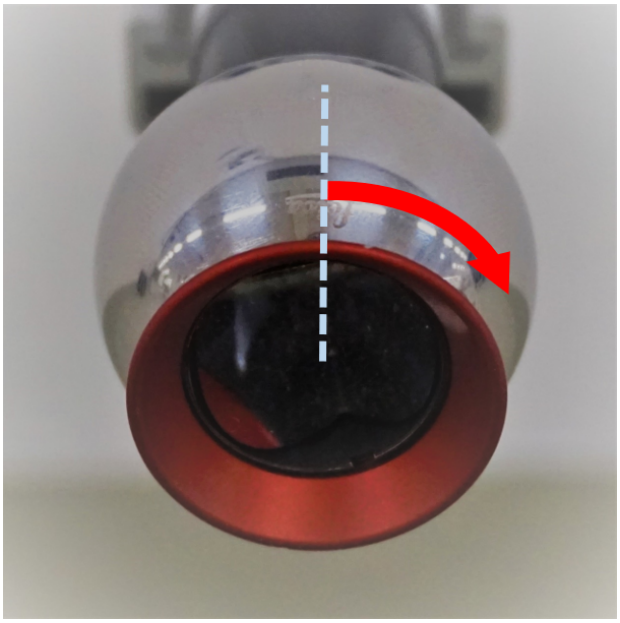

Figure 5.4.: The corner cube reflector is positioned at a console with its company branding pointing upwards. The red arrow indicates the reflector's direction of rotation.

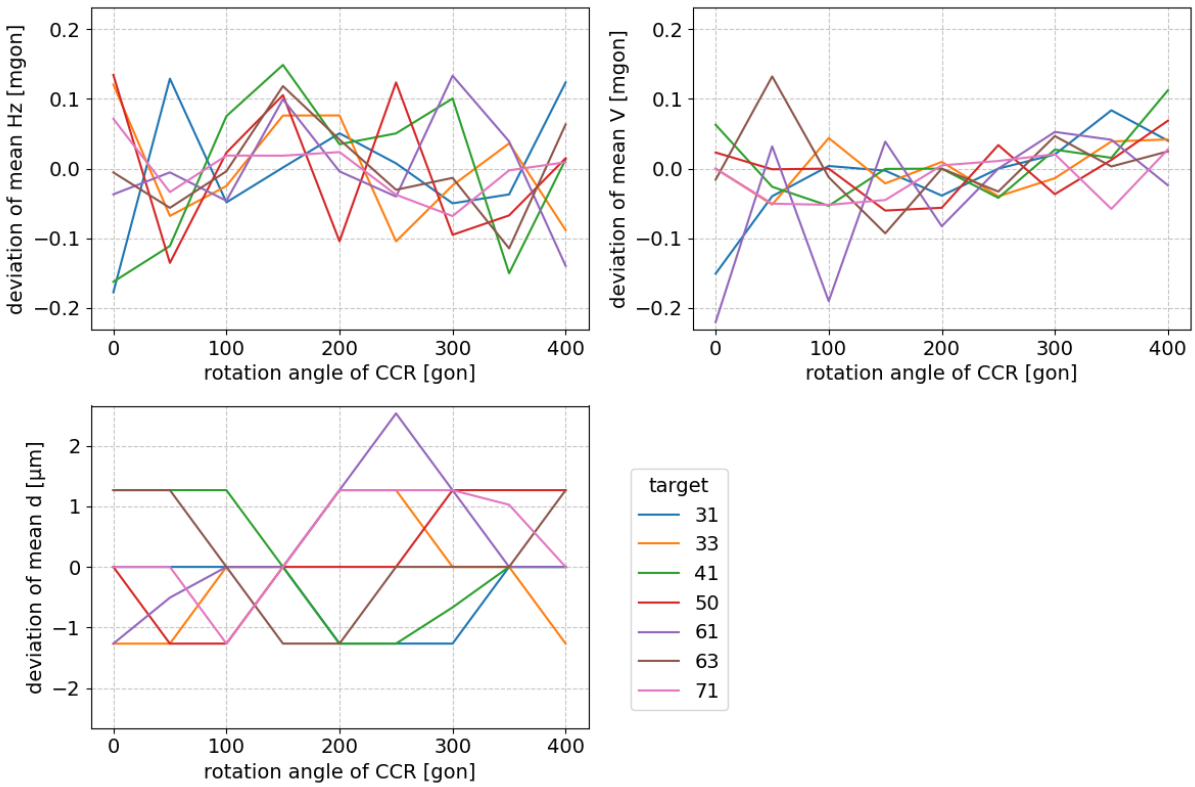

Figure 5.5.: Deviations to the mean values in the CCR roundness experiment for Hz_{LT}, V_{LT} and d_{LT}.

The deviations of the horizontal and vertical angle are in the same order of magnitude as those in the repeatability experiment. The plots do not reveal any systematic effects that would indicate deviations of the

CCR's roundness. The plot of distance deviations displays an unnatural behaviour which might be caused by the internal measurement process of the laser tracker. The deviations only seem to realise numbers of certain levels. Further investigation revealed that these levels correspond exactly to fractions and multiples of the wavelength used. Hence, the distance data of this experiment might be recorded at the level of the tracker's limit of distance resolution.

5.5. Total Station (Terrestrial Laser Scanner)

Before using geodetic instruments in extensive measurement campaigns, conducting testing procedures is recommended. Appropriate testing strategies for the used instrument are summarised in the standards ISO 17123-3 (theodolites) and ISO 17123-4 (electro-optical distance meters). However, no testing was done because the relevant measurement campaigns had already been performed much earlier until the final decision was made, which campaigns to use in this thesis. In addition, a gross deviation in the instruments accuracy would have been noticed in the available measurements.

As mentioned in Chapter 2.2.1, a multi station Leica MS60 is used as TLS instrument. This instruments provides automatic target recognition (ATR), nevertheless all experiments are conducted with manual aiming of the targets. The imperfect manufacturing of instruments causes uncertainties in the measurements conducted by the instruments. In order to gain insights into possible influencing factors that affect the uncertainty of TS(TLS) measurements, the following aspects are investigated.

Tilt Axis Deviation

The term tilt axis deviation denotes the non-perpendicularity of vertical axis and tilt axis i.e. the rotation axis of the vertical circle and the telescope. The tilt axis deviation is determined based on two-face measurements to targets with extreme vertical angles (Gruber *et al.* 2014). This procedure is recommended because the effect of a tilt axis deviation increases with observations far outside the horizon plane. In total ten targets with vertical angles ranging from 45 gon to 75 gon are measured in two faces in reflectorless mode. The resulting mean tilt axis deviation comprises 0.18 mgon. The effect of the tilt axis deviation can be eliminated by two face measurements, which is deployed in all network measurements. Nonetheless, this experiment aimed to detect gross instrumental malfunctions.

Collimation Deviation

Another error conditioned by the instrument is the non-perpendicularity of the tilt axis and the collimation axis (line of sight). This error, known as collimation deviation, is also eliminable by measurements in two faces. To check the used instrument for a possible collimation deviation, the procedure proposed by Gruber *et al.* (2014) with eight targets is conducted. Based on that, the collimation deviation of the used multi station is found to be 0.19 mgon.

Erroneous Reading of Vertical Angle

This error is caused by a deviation of the vertical angle reading from the true vertical angle of the telescope. It can be eliminated by measurements in two faces and is therefore noncritical for the network measurements. Nonetheless, it is determined by measurements to eight targets with a value of 0.62 mgon.

Axis Eccentricity

The term axis eccentricity refers to the angular difference between the distance axis and the collimation axis of the terrestrial laser scanner. Its effect on the final distance differences is important but only relevant for the scan measurements of the TLS, which can only be performed in one face. The influence of the axis eccentricity is covered in detail in Chapter 5.12.

Target Illumination

Especially for more distant targets, the difficulty of manually aiming at the centre of the CCR increases. Additional illumination to the laboratory lights by a torch facilitates the targeting of the reflector with the telescope. Two different torches with light colours white and green are used for illumination as shown in Figure 5.6. The light sources are contrasted against each other to see whether the colour of light could improve the observer's identification of the target centre. No significant differences between illumination with green and white light are observable based on comparing observations to 42 targets.

Figure 5.6.: Illumination of the corner cube reflector by white and green light. The visual impurities on the cube surfaces are caused by dust particles.

5.6. Laser Tracker

Similar to the TS(TLS), there is a standard for testing the performance of laser trackers (ISO 10360-10). Due to the enormous required effort and the lack of a suitable location for conducting the proposed testing procedures, only simple reproducibility experiments are done as outlined in Chapter 5.4.

5.7. Handheld Scanner

No geodetic testing procedures are carried out for this instrument. The reasons for that are the poor applicability of the most likely suitable standard (ISO 16331-1) and additional disproportionate effort.

5.8. Variance Component Estimation

To retrieve reliable results of the network adjustment, the VCE is based on the three available campaigns (data sets 3, 7, 9 in Table 5.1). In a first approach, all 22 epochs of these three campaigns are analysed separately. The standard uncertainties from the manufacturers and those derived in Chapter 5.2 are used as start values for the LT and TS(TLS), respectively. In fact, it is noted that different start values have almost no influence on the convergence behaviour. Epochs with unreasonable variance components such as unrealistically small or large components are excluded from further calculations. Throughout the whole process of estimating variance components it becomes apparent that one iteration in the estimation algorithm leads to most realistic variance components due to partly diverging iteration behaviour. The reason for this is blamed on the non-compliance of all preconditions that are stated in Chapter 2.1.2. The most important factor for the retention of the variance component estimates is the rapid convergence of the global test value towards 1 as discernible in Table 5.3. By means of a statistical test, the a-priori variance factor and the estimated variance factor are tested for statistical agreement (Niemeier 2008). Values close to 1 are considered acceptable. Apart from this, no covariances between the observations in the stochastic model are assumed.

Epochs of the same measurement campaign represent an identical geometrical constellation of the instruments. Thus, in a further step the VCE is done per measurement campaign with all related epochs together, except for those that are eliminated in the first step. In particular, the weak point of low redundancy per observation type is mitigated by this method. Table 5.3 shows the resulting variance components in the campaign-wise evaluation as well as the number of available and used epochs. Additionally, the improvement of the global test value between before and after the VCE is visible in the columns 'it. 0' and 'it. 1'.

Table 5.3.: Intermediate variance components per measurement campaign and the result of the global test prior and after the variance component estimation. The cancelled value is not used for the later derivation of global variance components due to its unrealistic magnitude.

campaign	**epochs**		**variance components**						**global test**	
	total	**used**	Hz_{TLS}	V_{TLS}	d_{TLS}	φ_{LT}	V_{LT}	d_{LT}	**it.0**	**it.1**
MS60	7	6	1.54	2.69	0.88	1.55	1.70	1.58	1.58	0.99
Klinker	6	4	1.09	1.10	0.48	1.02	1.06	0.67	0.60	1.00
Rauigkeit	9	6	1.08	1.14	~~0.06~~	1.27	1.24	1.24	0.76	0.94

The variance components can be interpreted as multiplicative factors for the a-priori instrument uncertainties. The aim of using variance components is to obtain appropriate instrument uncertainties suggested by the model and suitable for the particular measurement setup. Hence, the variance components are dependent on the functional model, the measurements i.e. the geometrical situation, and the assumed a-priori instrument uncertainties. Since identical instruments are used for all campaigns, global variance components are desired for each instrument irrespective of a campaign or epoch. Averaging the variance components of Table 5.3 yields in updated and to the conducted measurements more realistic instrument uncertainties. These global values are displayed in Table 5.4. For all types of observations, uncertainties of equal or slightly larger magnitude than initially assumed are ascertained. The difference between variance components for the horizontal angles and vertical angles is probably caused by the flattened, tube-shaped distribution of the network targets. This leads to low variations in the vertical angles in the measurements while the horizontal angles are, depending on the measurement campaign, spread over the entire horizon.

Table 5.4.: Global variance components plus original and updated instrument uncertainties for all observation types of the utilised laser tracker and total station (terrestrial laser scanner).

observation type	**variance component**	**uncertainty** (1σ)	
		manufacturer	after VCE
TS(TLS)			
horizontal angle	1.24	0.2 mgon	0.3 mgon
vertical angle	1.65	0.2 mgon	0.4 mgon
distance	0.68	0.7 mm	0.5 mm
LT			
horizontal angle	1.28	5.0 µm/m	6.4 µm/m
vertical angle	1.33	5.0 µm/m	6.7 µm/m
distance	1.16	5.0 µm	5.8 µm

Comparatively, a variance component analysis is performed for each epoch individually with the software SpatialAnalyzer (SA). The VCE comes along as by-product with the estimation of the transformation parameters. However, the resulting variance components differ significantly (up to two orders of magnitude) from the own estimates and are considered unrealistic due to extremely large and small values. These deviations are explicable by the presumably different functional model implemented in the used Unified Spatial Metrology Network (USMN) function. No explicit information on the technical functionality of USMN can be found in the user manual (New River Kinematics 2020). In addition, no obvious checking of the prerequisites for performing a VCE is done in SA. The critical point for the poor quality of variance components provided by SA is assumed to be also the low redundancy amounts per observation group.

5.9. Network Transformation

The propagation of uncertainties through the network transformation is solved via the Monte Carlo method (MCM). This offers the advantage that no linearisation is needed. The aim is to assign proper uncertainties to the transformation parameters between the LT network and the TS(TLS) network.

5.9.1. Input Quantities

A fundamental step in performing a Monte Carlo simulation is the determination of stochastic influence quantities. For this, it is essential to specify their probability density functions. In case of assumed correlations a switch to joint probability density functions is necessary. Furthermore, the mathematical impact of the input quantities on the functional model needs to be known. Most of the input quantities for the implemented measurement setup are already mentioned in Zámečníková *et al.* (2018). Table 5.6 is intended to give an overview of the selected input quantities as well as their assumed probability density and source. For better understanding and distinguishability, definitions of some input quantities that might be confusable or unclear are given in Table 5.5.

Table 5.5.: Description of input quantities

Input quantity	**Description**
CCR Centring Error	describes how well the cube corner is located in the centre of the outer sphere
CCR Radius	describes the quality of the physical realisation of the reflector's mean radius of 19.05 mm
CCR Shape	describes the mean deviation from the mean radius of a perfect sphere
Point Stability	physical stability of the consoles against deformations over time. Theoretically this quantity is individual for each console but large values for single consoles (rickety mounting) are considered as gross errors and are thus excluded from evaluation.
Axis Error	deviation between measured angle and physically realised angle
Atmospheric Error	atmospheric parameters for distance corrections are determined by measurements of a meteorological station and are therefore attached with uncertainties
Measurement Repeatability	uncertainty arising from repeated insertion of the reflector into a console
Instrument Stability	stability over time against displacement and loss of adjustment
TS(TLS) Eccentricity	eccentricity between the distance axis and the collimation axis of the TS
Point Matching Error	TLS scan points and reference scan points ordinarily do not lie on top of each other. Point pairs are found by matching close points if the angular deviations fall below thresholds.

Due to the used functional model and the utilisation of the MCM for uncertainty propagation, several sources of uncertainty can be ignored or are implicitly represented in the measurements. Levelling terms are not considered for example since the functional model is not depending on measurements of levelled instruments.

Uncertainties of axis errors of the TS(TLS) are also implicit in the measurements and are eliminated by observations in two faces.

Table 5.6.: Input quantities of the Monte Carlo method along with their probability density function (PDF) and source. All quantities are drawn from Gaussian distributions ($\mathcal{N}$)

Input quantity	**PDF**	**Unit**	**Source**
CCR Centring	$\mathcal{N}(0, 0.003)$	mm	data sheet (Hexagon Metrology 2022)
CCR Radius	$\mathcal{N}(0, 0.0025)$	mm	Chapter 5.4, data sheet (Hexagon Metrology 2022)
CCR Shape	$\mathcal{N}(0, 0.0015)$	mm	Chapter 5.4, data sheet (Hexagon Metrology 2022)
Point Stability	$\mathcal{N}(0, 0.013)$	mm	literature (Zámečníková *et al.* 2018)
Meas. Repeatability	$\mathcal{N}(0, 0.01)$	mm	Chapter 5.4, literature (Zámečníková *et al.* 2018)
Atmospheric Error	$\mathcal{N}(0, 1.94)$	µm/m	Chapter 5.3, data sheet (Revue Thommen AG n.d.)
Hz_{TLS}	$\mathcal{N}(Hz_i, 0.26)$	mgon	VCE, data sheet (Leica Geosystems 2020)
V_{TLS}	$\mathcal{N}(V_i, 0.35)$	mgon	VCE, data sheet (Leica Geosystems 2020)
d_{TLS}	$\mathcal{N}(d_i, 0.48)$	mm	VCE, data sheet (Leica Geosystems 2020)
Hz_{LT}	$\mathcal{N}(Hz_j, 6.40)$	µm/m	VCE, data sheet (Leica Geosystems n.d.)
V_{LT}	$\mathcal{N}(V_j, 6.65)$	µm/m	VCE, data sheet (Leica Geosystems n.d.)
d_{LT}	$\mathcal{N}(d_j, 5.80)$	µm	VCE, data sheet (Leica Geosystems n.d.)

Meticulous reflections on presumable correlations between the input quantities are done. The resulting and implemented correlations are illustrated in Table 5.7. Whereas most of the quantities are uncorrelated, some correlations, specifically related to the atmosphere, are introduced. These correlations and their magnitude are set out in detail below Table 5.7.

Table 5.7.: Assumed correlations among the input variables of the Monte Carlo method.The magnitudes of the non-zero elements are itemised below.

	CCR centre	CCR radius	CCR shape	Point stability	Meas. repeatability	Atmospheric error	$Hz_{TLS,i}$	$V_{TLS,i}$	$d_{TLS,i}$	$Hz_{LT,i}$	$V_{LT,i}$	$d_{LT,i}$
CCR centre		-	-	-	-	-	~	~	~	~	~	~
CCR radius	-		-	-	-	a	~	~	~	~	~	~
CCR shape	-	-		-	-	b	~	~	~	~	~	~
Point stability	-	-	-		-	c	-	-	-	-	-	-
Meas. repeatability	-	-	-	-		-	-	-	-	-	-	-
Atmospheric error	-	a	b	c	-		-	-	d	-	-	d
$Hz_{TLS,i}$	~	~	~	-	-	-		-	-	*	-	-
$V_{TLS,i}$	~	~	~	-	-	-	-		-	-	*	-
$d_{TLS,i}$	~	~	~	-	-	d	-	-		-	-	*
$Hz_{LT,i}$	~	~	~	-	-	-	*	-	-		-	-
$V_{LT,i}$	~	~	~	-	-	-	-	*	-	-		-
$V_{LT,i}$	~	~	~	-	-	d	-	-	*	-	-	

a	0.5	The radius of the CCR will slightly change with temperature (air pressure and humidity are expected to have no effect) within its uncertainty range.
b	0.2	The deviations from the CCR's mean radius are expected to correlate with temperature. The main effect of temperature is absorbed by the radius itself, though also the shape deformations are assumed to change (no effect from air pressure and humidity).
c	0.2	The stability of consoles, especially along the axis towards the wall is affected by temperature because the consoles are up to 20 cm long, made of metallic material and therefore offer potential for thermal expansion. The correlation is set low because only consoles mounted on walls and only one direction of the 3D stability is affected. Besides only temperature of the whole atmospheric term plays a role.
d	0.8	Relatively strong correlation is assumed between atmospheric correction and TS(TLS)- and LT-distance
~	0.0	Geometrically an imperfection of the CCR results in uncertainties of the measurands of the TS(TLS) and LT. However the effects in different directions for each point and altogether the final effect is mitigated below significance by redundancy.

*	0.0	Depending on the geometrical measurement setup i.e. the location of the instruments relative to each other and in relation to the high-accuracy network, correlations are thinkable. Particularly for a setup with the instruments positioned closely to each other relevant correlations are expected. Since this is not the case in the performed experiments, these correlations are set to zero.

For each Monte Carlo trial, input quantities are drawn from the joint probability density functions according to Tables 5.6 and 5.7.

5.9.2. Functional Model

The functional model of the MCM is the transformation model as derived in Chapter 4. The complete equation system consists of $3n + 1$ equations, where n is the number of measured network points. The mathematical integration of the input quantities apart from the physical LT- and TS(TLS)-observations is achieved by additive terms to the distances and additional perpendicular perturbations of the angle measurements as described by (5.10) to (5.12).

$$Hz_{MCM,i} = Hz_i + \delta Hz_{CCR\,centre,i} + \delta Hz_{CCR\,rad,i} + \delta Hz_{CCR\,shape,i} + \delta Hz_{point\,stab,i} + \delta Hz_{meas\,repeat,i} \tag{5.10}$$

$$V_{MCM,i} = V_i + \delta V_{CCR\,centre,i} + \delta V_{CCR\,rad,i} + \delta V_{CCR\,shape,i} + \delta V_{point\,stab,i} + \delta V_{meas\,repeat,i} \tag{5.11}$$

$$d_{MCM,i} = d_i + \delta d_{CCR\,centre,i} + \delta d_{CCR\,rad,i} + \delta d_{CCR\,shape,i} + \delta d_{point\,stab,i} + \delta d_{meas\,repeat,i} + d_i \cdot \delta d_{atmos,i} \tag{5.12}$$

All input quantities which perturb the spherical measurands are sampled for each Monte Carlo trial and for each measurand separately. Each sample consists of a set of scalars which represents the magnitude of the corresponding errors. The errors of CCR centring, radius and shape, the point stability and the measurement repeatability are considered to be 3D vectors whose absolute values are given by the sample. The direction of these errors is expected to be uniformly distributed. Hence, the absolute values of the errors are split up into spherical components that can be added to the spherical measurands. To avoid the introduction of unintended systematic characteristics to the spherical measurands, each error vector is attributed with a random direction. One exception is the additional error caused by the atmosphere, which contributes only to the distances. Additionally it is multiplied by the measured distances since it is given as a relative error (see Eq. (5.12)). The number of Monte Carlo trials is set to 5000.

5.9.3. Result

The resulting transformation parameters as well as their corresponding uncertainties as acquired by the MCM are listed in Table 5.8. The large uncertainty in Y-translation is reasoned by the eccentric position of the TS(TLS) in relation to high-accuracy network (see Figure 3.3). The direction of the eccentricity coincides with the Y-axis of the TS(TLS). The larger value of the X-rotation uncertainty is explicable again by the position of the TS(TLS). With respect to the X-axis as rotation axis all network points appear in a small field of the full circle. The rightmost column labelled 'empirical' provides comparative uncertainties. Therefore, transformation parameters are derived by network transformations for six epochs of the campaign 'Rauigkeit'. The individual epochs are measured in successive days and represent the identical geometric constellation. The scatter of the transformation parameters is described by the empirical standard deviation. However, the small number of

epochs only allows statements with limited significance. Nevertheless, most transformation parameters show pretty good agreement, while some parameters are estimated with a larger uncertainty by the MCM. This indicates, that based on the uncertainties of the input quantities, the MCM tends to estimate the uncertainties of the transformation parameters realistically to slightly pessimistically. The difference in the uncertainties of the Y-translation parameter might be caused by modelling the uncertainties related to distance measurements non-optimally.

Table 5.8.: Transformation parameters and their uncertainties for the campaign 'Rauigkeit' derived by Monte Carlo simulation and by empirical evaluation of 6 epochs.

Parameter	**Quantity**		**Standard Uncertainty**			
			MCM		empirical ($n = 6$)	
t_x	1089.39	[mm]	0.04	[mm]	0.04	[mm]
t_y	21534.67	[mm]	0.26	[mm]	0.12	[mm]
t_z	-102.44	[mm]	0.04	[mm]	0.03	[mm]
ω	0.1984	[gon]	0.88	[mgon]	0.60	[mgon]
φ	-0.4143	[gon]	0.45	[mgon]	0.45	[mgon]
κ	103.2834	[gon]	0.42	[mgon]	0.29	[mgon]

5.9.4. Effect on Distance Differences (ΔD)

The derived transformation parameters are used to transform the reference scans which are available in the laser tracker's coordinate system into the frame of the terrestrial laser scanner. Then the scan distances are available in the same coordinate system and a direct comparison of pairs of scan points is meaningful. However, the level of geometrical coincidence of the two origins is determined by the uncertainty of the transformation parameters. Ideally, the origin of the TLS and the (transformed) origin of the LT lie on top of each other. Depending on the measurement setup and the scan setup, uncertainties of the transformation parameters have different impacts on the uncertainties of the scans. Referring to the implemented setup (ROSIAM system) as sketched in Figure 5.7, the following facts and relationships are noted.

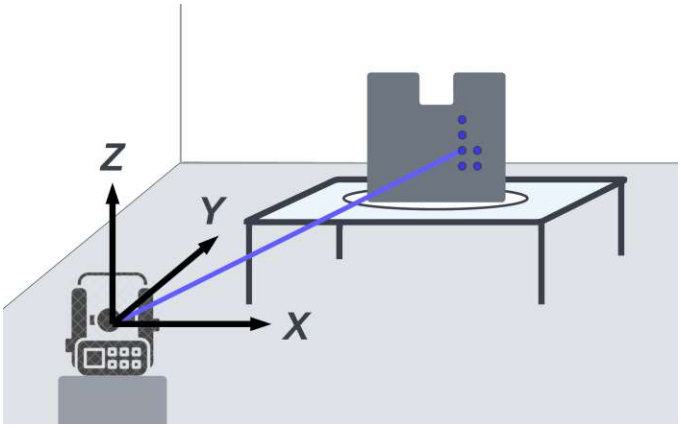

Figure 5.7.: Sketch of the TLS scan setup with particular emphasis to the coordinate system in relation to the scanned object.

– The scanned object is positioned in such a way that the X- and Z-coordinate of scan points vary around zero. An absolute translation error in X-direction leads to a pairing of different scan points. However, an uncertainty in the X-translation does not change the point correspondences but evokes an additional uncertainty in the distance differences ΔD_{tx}, which is sketched in Figure 5.8 and estimated in Eq. (5.13). With increasing angle of incidence, a significant uncertainty arises in the distance differences as depicted in the left plot of Figure 5.10. An uncertainty in X-translation has no impact on distance differences when the angle of incidence is zero. The reason for this is that with $IA = 0$ the object plate is parallel to the X-axis and thus both scans are, too.

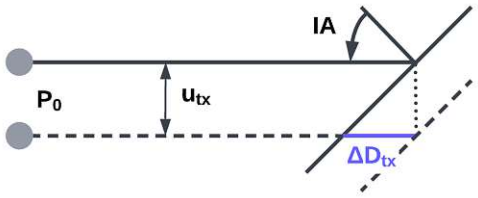

Figure 5.8.: Sketch displaying the effect of an uncertainty in X-translation onto distance deviations

$$\Delta D_{tx} = u_{tx} \cdot \tan(IA) \tag{5.13}$$

– The direction of scan distances approximately coincides with the Y-axis. Uncertainties in the Y-translation are therefore directly propagated into uncertainties of ΔD. This relationship is undisturbed by the incidence angle. Because of the missing attenuation of the uncertainty, this influence can be denoted as principal influence factor.

– Alike to the X-translation, uncertainties of the Z-translation propagate without affecting ΔD. This is the case for all angles of incidence since the object is fixed vertically throughout all experiments. A tilting of the scan object would cause a similar influence behaviour as described for the X-translation.

– Uncertainties in the rotation angle around the X-axis are omitted due to the negligible impact for the prevailing scan distances and the prevailing X-rotation uncertainty as being output by the MCM. Furthermore, attenuation of the effect is given by the averaging of distance differences spread over the object.

– Uncertainties of the Y-rotation angle are neglected. The qualified reason is again the vertical orientation of the scanned surface.

– Finally, uncertainties in the angle of Z-rotation map to ΔD-uncertainties in a similar behaviour as uncertainties in X-translation (see right plot of Figure 5.10). The effect cancels out when the object is scanned perpendicularly. With increasing angle of incidence, the effect rises according to Equation (5.14). Figure 5.9 displays the geometrical situation for the derivation of the additional error in distance differences.

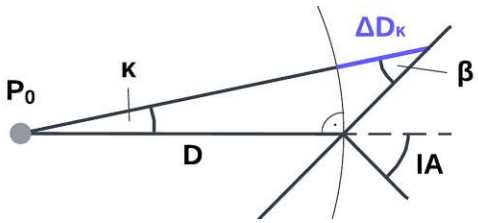

Figure 5.9.: Sketch displaying the effect of an uncertainty in Z-rotation angle (κ) onto distance deviations.

$$\Delta D_\kappa = D \cdot \left(-1 + \frac{\cos(IA)}{\cos(IA + \kappa)} \right) \tag{5.14}$$

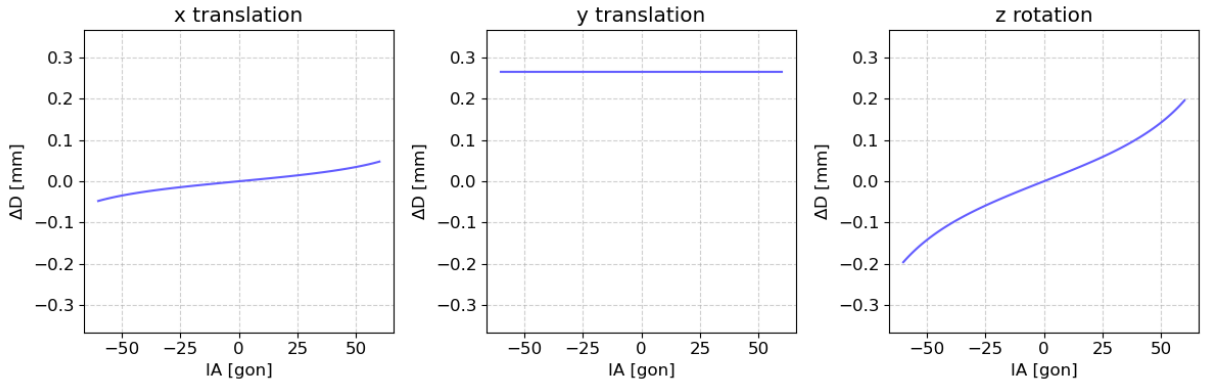

Figure 5.10.: Simulated influence curves of uncertainties in the transformation parameters onto uncertainties of ΔD. A mean scan distance of 30 m is assumed. The magnitude of the input uncertainties (uncertainties of the transformation parameters) correspond to the standard uncertainties generated by the Monte Carlo method.

5.10. Scan Point Matching

After the network transformation, corresponding scans are available in the same coordinate system. The origin of the coordinate system coincides with the TS's and TLS's zero point P_0. In fact, the spherical observations of the scans (horizontal angle, vertical angle and distance) exist as if both scans were measured from the standpoint of the TLS. This enables direct comparison of the spherical elements. Discrete comparative evaluations require the mapping of pairs of scan points. However, points of the TLS scan and the LT scan i.e. the reference scan do not lie physically on top of each other. The mapping criterion for building pairs of scan points is the least spherical distance without exceeding a threshold.

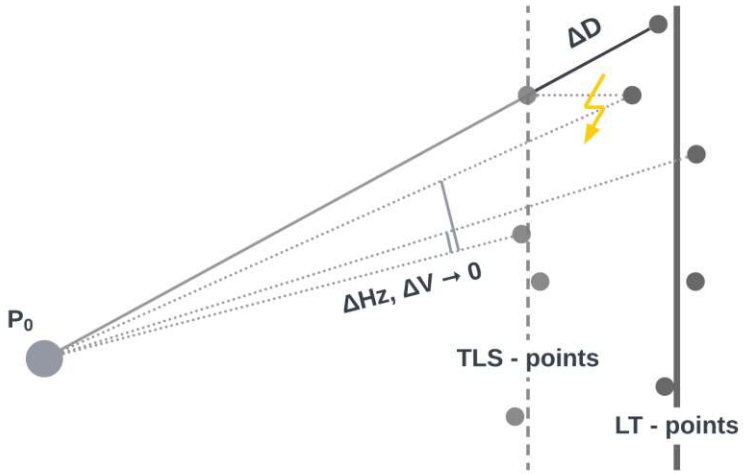

Figure 5.11.: Scan points are matched according to the lowest deviation in Hz and V (adapted from Linzer *et al.* (2021))

As legible in Figure 5.11, corresponding point pairs do not necessarily represent the geometrically closest possible pair of points. The arising error from this imperfection is estimated subsequently. In comparison to the scanning distance of approximate 30 m, the scan point spacing as well as the differences between TLS points and LT points are small. The maximum point spacing perpendicular to the line of sight (Δx) as allowed by the angular point matching thresholds (ΔHz and ΔV) is calculated. By solving the indicated right-angled triangle in Figure 5.12, the resulting error of distance differences $\zeta_{\Delta D}$ is derived (5.15).

$$\zeta_{\Delta D} = \frac{\Delta x}{\tan\left(\frac{\pi}{2} - IA\right)} = \frac{\sin(\Delta Hz) \cdot d}{\tan\left(\frac{\pi}{2} - IA\right)} \tag{5.15}$$

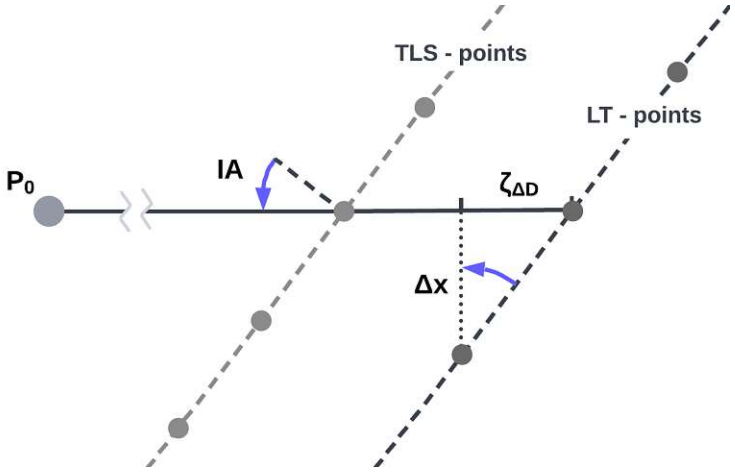

Figure 5.12.: The maximum point matching error $\zeta_{\Delta D}$ is dependent on the angle of incidence (IA) and the maximum point spacing Δx perpendicular to the line of sight.

Obviously, this source of uncertainty is dependent on the scan distance d and on the angle of incidence. Further simulated analysis of the magnitude of this error is shown in Figure 5.13. The curves represent the maximum permitted angular deviation when searching for corresponding points without exceeding a distance error of 0.06 mm. This maximum error is chosen in consensus with the uncertainty of the reference point determination at the limit of significance. A lower error threshold would fall below the determination uncertainty of individual points and therefore would reduce the number of assignable points without further reducing the point matching error. The areas below the curves can be interpreted as allowable angle deviations for the point matching. The dashed grey line indicates the chosen value for the maximum angle deviation. This criterion only becomes critical for large scan distances in combination with incidence angles of more than 55 gon.

As already mentioned, the point matching error is estimated as a maximum error. To consider its effect on distance deviations in compliance with the GUM, the maximum error is converted into a standard uncertainty according to Equation (2.34). This standard uncertainty is abbreviated as $u_{\Delta D,point\ matching}$.

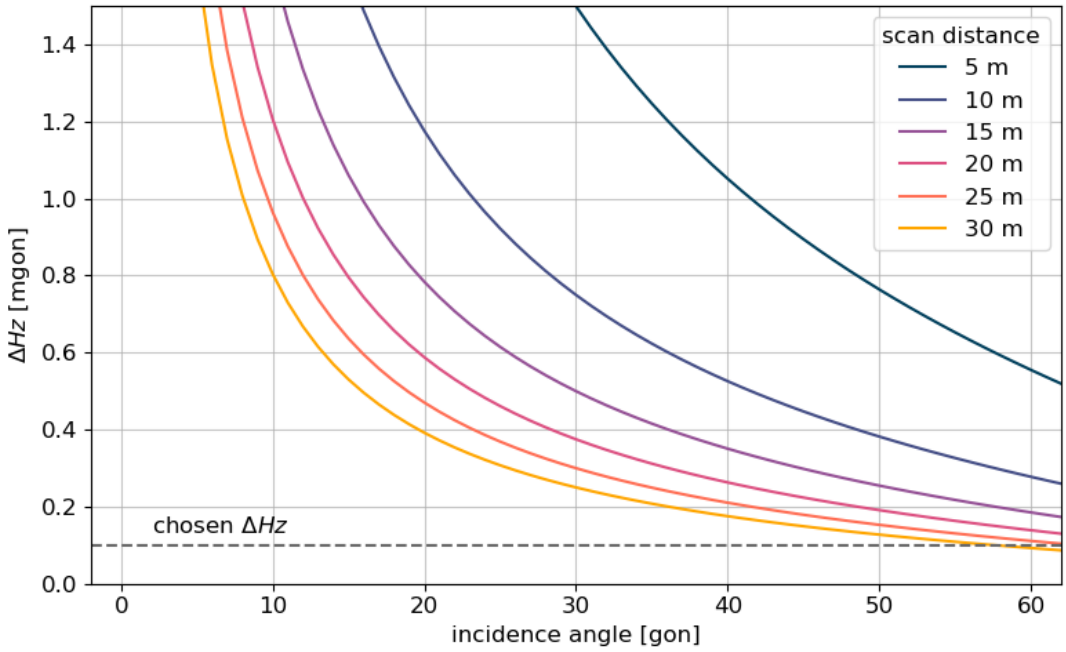

Figure 5.13.: Characteristic curves marking the maximum permissible angle deviations in order to not exceed a distance error ($\zeta_{\Delta D}$) of 0.06 mm

5.11. Scan Uncertainty

The relevant part of the scan uncertainty of the TLS (i.e. the range noise) is specified as 1 mm to 1.5 mm, depending on the scan distance and the scan frequency (Leica Geosystems 2020). This uncertainty applies to single scan points. The corresponding uncertainty for the mean of multiple scan points is lowered by the number of scan points q (5.16).

$$u_{TLS\,scan} = \frac{u_{TLS\,scan\,noise}}{\sqrt{q}} \tag{5.16}$$

The number of scan points is in this application the number of correspondences among scan points and reference points. This number typically varies between 300 and 3000 for each pair of scans in the experiments. Hence, an average TLS scan uncertainty of $u_{TLS\,scan} = 0.04$ mm is estimated.

5.12. Axis Eccentricity

A basic assumption used in the definition of D_{TLS} is that the distance axis coincides with the collimation axis (Zámečníková *et al.* 2018). If this assumption is incorrect, an eccentricity occurs which is denoted by ε in Figure 5.14. The direction of the eccentricity angle in the horizontal plane in combination with the orientation of the measuring object determine whether the measured D_{TLS} is longer or shorter than the distance in the direction of the collimation axis. The effect of an eccentricity on D_{TLS} and thus also on ΔD increases with increasing incidence angle and is zero for perpendicular aiming. It can be estimated by Eq. (5.17) from the difference between the correct distance and the perturbed distance. The influence characteristic of an axis eccentricity and thus its geometrical derivation is identical to that of the Z-rotation uncertainty (see Chapter 5.9.4).

$$\varepsilon_{\Delta D} = D \cdot \left(-1 + \frac{\cos(IA)}{\cos(IA + \varepsilon)} \right) \tag{5.17}$$

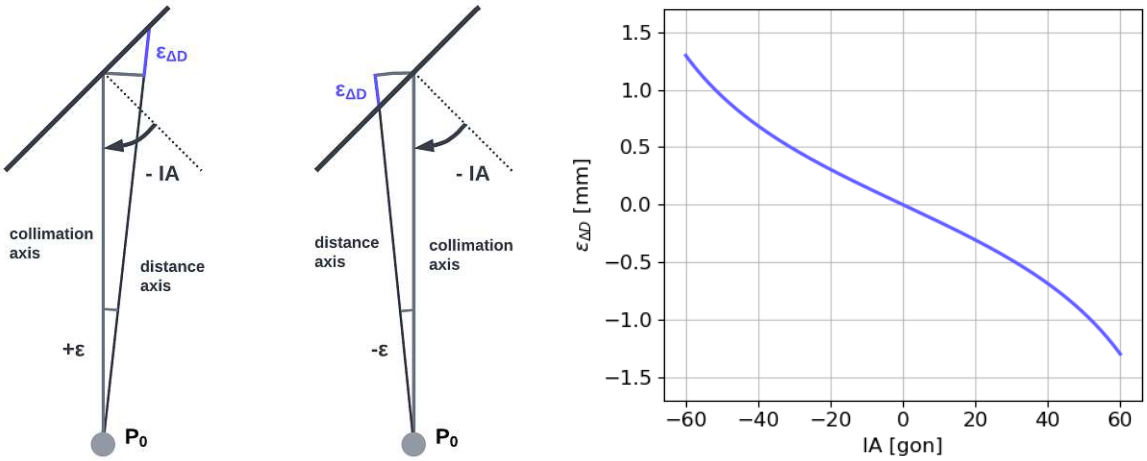

(a) (b)

Figure 5.14.: Eccentricity ε between distance axis and collimation axis and its effect on distance differences $\varepsilon_{\Delta D}$. (a) exaggerated sketch; (b) simulation of the influence under incidence angle ($\varepsilon = 2$ mgon, $D = 30$ m) (adapted from Zámečníková *et al.* (2018))

The error arising from the axis eccentricity is minimised by averaging distance differences of the same positive and negative IA as specified by Equation (5.18).

$$\Delta D_{\pm IA} = \frac{\Delta D_{m,+IA} + \Delta D_{m,-IA}}{2} \tag{5.18}$$

The corresponding standard deviation of the averaged distance differences can be derived by variance propagation of Eq. (5.18) and results in a compact Formula (5.19) as initially demonstrated by Zámečníková *et al.* (2018).

$$\sigma_{\Delta D,\pm IA} = \sqrt{\frac{\sigma_{\Delta Dm,+IA}{}^2 + \sigma_{\Delta Dm,-IA}{}^2}{4}} \tag{5.19}$$

5.13. Neglected Influential Quantities

A number of further issues might appear to be influencing and are therefore covered in this section.

Angle of Incidence

The angle of incidence is itself estimated as part of the measurement setup. For its determination a circular scale is attached to the rotary table. The sole purpose of the scale is to adjust the object's attitude as best as possible. This is achieved with an accuracy of approximately ±3 gon. However, results and plots with respect to the IA are not dependent on that accuracy value since the 'true' IA can be retrieved from the scanning data by fitting planes into the point clouds. This IA is determined with a high redundancy and its resulting uncertainty is negligible for the results.

Robot Arm

Neither the scanning by hand nor the scanning with the help of the robotic arm introduces new uncertainties for the reference scan as long as the scanning requirements for the T-Scan are obeyed. This includes scanning in optimal scan distance and not too rapid movements of the T-Scan. The uncertainty of the local reference point cloud is only determined by the interaction of the laser tracker and the handheld scanner. The means for the physical movement of the scanner is therefore irrelevant.

Functional Model

Uncertainties arising from the used functional transformation model and its linearisations are considered by the implicit variance propagation in the adjustment model. To minimise linearisation errors, the termination criterion for the iterative process is quite strictly set to 10^{-10}.

Target Distribution

As mentioned in Chapter 3.1.1, the targets of the high-accuracy network are distributed anisotropically in the elongated laboratory. This non-optimal geometrical constellation mitigates the achievable transformation accuracy based on the high-accuracy network. However, no extra evaluation of the target distribution is done since the observations implicitly represent the spatial distribution of the network points.

5.14. Summary

The conducted investigations on the individual sources of uncertainty are finally summarised. Table 5.9 comprises the findings of the foregoing sections and thus constructs a total uncertainty budget for the ROSIAM procedure and the developed network transformation model. Relevant influence factors and their uncertainties already analysed in Zámečníková *et al.* (2018) are adopted from this publication.

The derivation of final standard uncertainties assigned to the distance differences is carried out via uncertainty propagation. All sources of uncertainty, that are not considered already in the Monte Carlo method for the network transformation, are assumed to have an additive impact on the distance differences. Namely, these are the point matching uncertainty $u_{\Delta D,point\ matching}$ (see Chapter 5.10) and the standard uncertainty of TLS scan noise $u_{TLS\ scan}$ (see Chapter 5.11). Hence, Equation 5.20 shows the calculation of the final uncertainty for distance differences per angle of incidence. The first term denotes the resulting standard uncertainty of the MCM after the averaging step for positive and negative incidence angles (see Chapter 5.12).

$$u^2_{\Delta D} = u^2_{\Delta D,\pm IA} + u^2_{\Delta D,point\ matching} + u^2_{TLS\ scan} \tag{5.20}$$

Table 5.9.: Uncertainty budget for the ROSIAM procedure.

Part	Influence	Parameter/Action	Value
High-accuracy network	console stability	max. coordinate deviation	0.04 mm
	CCR-reflector	CCR radius	0.0025 mm
		CCR centring	0.003 mm
		CCR shape	0.0015 mm
TLS	horizontal angle	accuracy for two faces	0.3 mgon
	vertical angle	accuracy for two faces	0.4 mgon
	axis errors	eliminated in two faces	
	distance measurement	accuracy for two faces	0.5 mm
	atmospheric correction	considered	1.94 µm/m
	target illumination	no effect	
LT	horizontal angle		0.4 mgon
	vertical angle		0.4 mgon
	distance		5.8 µm
	atmospheric correction	considered	1.90 µm/m
	point repeatability		<0.05 mm
network transformation / D_{ref} starting point	levelling	not required	
	starting point accuracy	max. coordinate standard deviation	0.26 mm
end point of D_{ref}	LT stability	max. coordinate difference	0.05 mm
	HS-accuracy	max. coordinate	0.06 mm
	robot arm repeatability	no effect	
Spatial assignment $D_{TLS} - D_{ref}$	TLS orientation unknown	not required	
	TLS eccentricity		
	horizontal	eliminated by averaging ΔD under same positive and negative IA	
	vertical	low effect due to rotation of the measuring object about a nearly vertical axis	
	point matching thresholds ΔHz, ΔV		
	due to IA	max. impact under $IA = 60$ gon	0.06 mm
	due to roughness	reduced by averaging ΔD over an alignment of the measuring object	
	Hz_{TLS}, V_{TLS}-noise	reduced by averaging ΔD over an alignment of the measuring object	0.04 mm

6. Analysis of Uncertainties

This chapter is dedicated to the statistical analysis of the derived distance differences ΔD and their standard uncertainties. Figure 6.1 displays the distance differences for all materials (see Appendix A) that are investigated in the 'Rauigkeit' campaign. The curves are attached with 1σ intervals (intervals of standard uncertainty) as derived in Chapter 5. By visual interpretation of the plots it can be directly apprehended that significant differences between ΔD values of some materials exist. However, all findings are supposed to be approved by statistical tests.

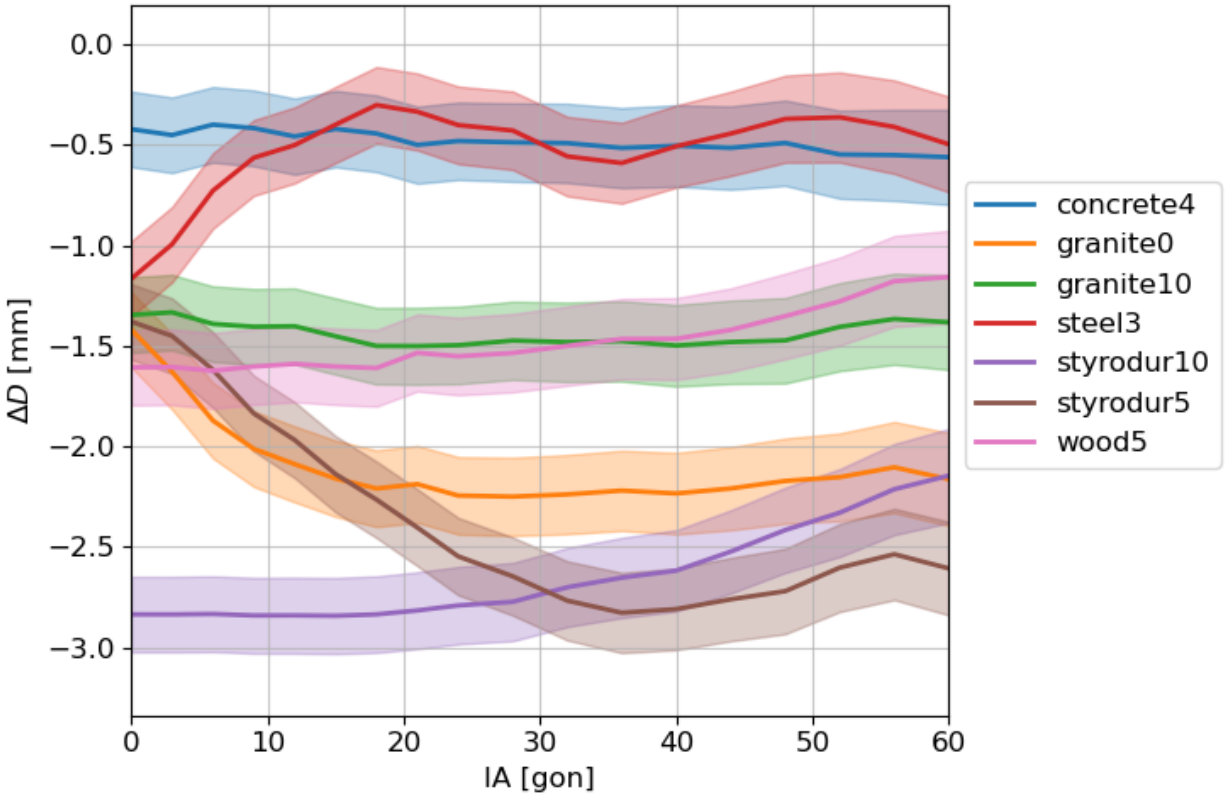

Figure 6.1.: Distance differences and the corresponding 1σ intervals for all investigated materials. Suffixed numbers to the materials are used to distinguish between different levels of surface roughness of the same kind of material.

Hypothesis tests are conducted in order to confirm or disconfirm assumed equality between distance differences of different materials but identical incidence angle. Since the main concern aims on the detection of statistical inequality in the distance differences, all null hypotheses are formulated for the equality of the respective values while the alternative hypotheses hold the corresponding inequality equations. Furthermore, all tests are evaluated for a level of confidence of 0.95 or 95 %.

6.1. Analysis of Distance Differences

The statistical testing of variations in the distance differences ΔD between different materials is accomplished via a paired difference test with known variances. This kind of hypothesis test is described in Niemeier (2008) and is summarised in Chapter 2.1.5. In its actual application for distance differences the null hypothesis is given as

$$H_0 : E(\Delta D_{IA,i}) = E(\Delta D_{IA,j}) \iff E(d) = E(\Delta D_{IA,i}) - E(\Delta D_{IA,j}) = 0 \tag{6.1}$$

where the indices i and j denote different materials. The alternative hypothesis is formulated as

$$H_a : E(\Delta D_{IA,i}) \neq E(\Delta D_{IA,j}). \tag{6.2}$$

If the null hypothesis is not rejected by the test it can not be stated that the distance differences between material i and j differ significantly. Oppositely, if the null hypothesis is rejected it can be stated that the distance differences between the respective materials differ significantly at a level of confidence of 0.95.

Another statistic test, the Welch's t-test, might appear more suitable at first sight to test the results. However, the available results do not obey all requirements to serve as input parameters for the test. The Welch's t-test is the parametric test for comparing means between two independent groups without assuming equal population variances (Ahad *et al.* 2014). This statistic is robust for testing the equality of means when the homogeneity assumption is not satisfied. Welch's t-test defines the statistic t by Formula (6.3).

$$t = \frac{(\overline{x}_1 - \overline{x}_2) - (\overline{\mu}_1 - \overline{\mu}_2)}{\sqrt{\frac{s_1^2}{n_1} + \frac{s_2^2}{n_2}}} \tag{6.3}$$

where

$$\begin{aligned} \overline{x}_1,\ \overline{x}_2 &= \text{mean of sample } 1,2 \\ s_1^2,\ s_2^2 &= \text{variance of sample } 1,2 \\ n_1,\ n_2 &= \text{size of sample } 1,2 \\ \mu_1 - \mu_2 &= \text{difference between the expected values} \end{aligned}$$

Consequently, the test statistic t requires two independent samples including their respective means, variances and sample sizes. Due to the derivation process of ΔD and its standard uncertainty $u_{\Delta D}$ these statistic parameters are not attuned to each other. The mean of ΔD is derived by averaging the distance differences of corresponding pairs of scan points. The related standard deviation to that mean value is only a small fraction of the final standard uncertainty of ΔD since it only represents the dispersion of distance differences of the individual scan points. The major portion of $u_{\Delta D}$ originates from the output of the uncertainty propagation of the network transformation which bundles uncertainty sources like atmosphere, high-accuracy network and instruments. The complex and nested uncertainty propagation especially concerning the MCM does not allow a proper derivation of joint sample sizes and joint degrees of freedoms which can be meaningfully attributed to the derived final uncertainty. The availability of these parameters is a precondition to correctly apply the Welch's t-test. Hence this test is disqualified for the analysis of distance differences.

Figure 6.2 and 6.3 exemplarily display the distance differences and the corresponding intervals of standard uncertainty for two selected materials each. In the first plot materials with similar distance differences are chosen, while in Fig. 6.3 materials with relatively dissimilar distance differences are displayed. The binary coloured bar at the bottom of each plot illustrates the (un-)successful detection of significant deviations in the distance differences as issued by the statistical tests at a level of confidence of 0.95.

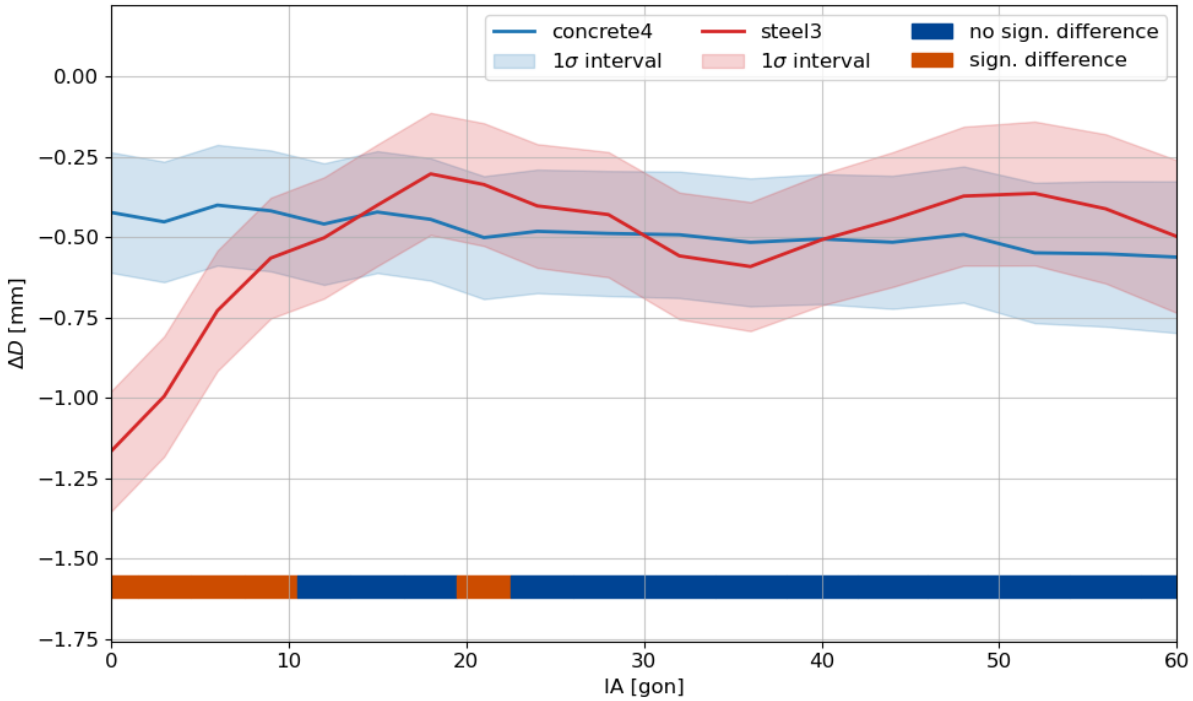

Figure 6.2.: Distance differences ΔD and corresponding 1σ intervals for two materials. Significant differences in ΔD are marked by the bar at the bottom.

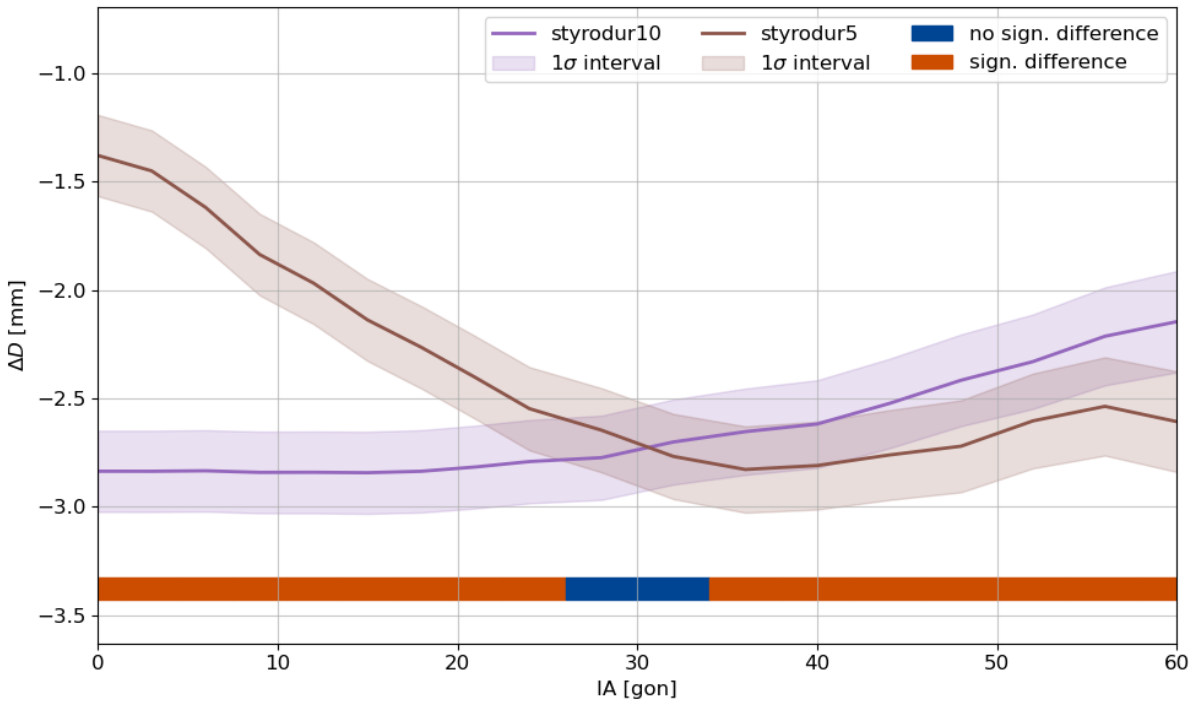

Figure 6.3.: Distance differences ΔD and corresponding 1σ intervals for two materials. Incidence angles with significant differences in ΔD are marked by the bar at the bottom.

Among the distance differences between the materials 'concrete4' and 'steel3' significant deviations are attested only for the incidence angle ranges of circa $[0, 11]$ and $[19, 23]$ gon. In contrast, significant deviations are observed for the compared materials 'styrodur5' and 'styrodur10' for all angles of incidence except for the interval of [27, 33] gon. Further comparisons of pairs of materials including significance statements are compiled in Appendix B.

6.2. Analysis of Uncertainties of ΔD

To answer the question whether the uncertainties of distance differences are equal for all investigated materials and incidence angles, the derived uncertainties are analysed in statistical tests. The utilised hypothesis test for this purpose is the F-test (see Chapter 2.1.5).

The null hypothesis (6.4) states the equality of the expectations of the two variances representing different materials or different angles of incidence (generically indicated by indices i and j).

$$H_0 : E(s^2_{\Delta D,i}) = E(s^2_{\Delta D,j}) \tag{6.4}$$

The case of inequality is caught in the alternative hypothesis:

$$H_0 : E(s^2_{\Delta D,i}) \neq E(s^2_{\Delta D,j}). \tag{6.5}$$

The test statistic for the two-tailed test is calculated as Equation (6.6) shows.

$$F = \frac{s^2_{\Delta D,i}}{s^2_{\Delta D,j}} \tag{6.6}$$

Based on the comparison to critical values, $F_{\nu 1,\nu 2,\alpha/2}$ and $F_{\nu 1,\nu 2,1-\alpha/2}$, given by tables of the Fisher distribution, the hypotheses are rejected or not rejected. The most difficult task here is to find proper estimates for the degrees of freedom. Although the Monte Carlo method offers with its number of trails an estimate of redundancy, this number is not suitable. The reason is that the uncertainty due to the MCM is only a small contribution of the total uncertainty of ΔD. The largest part originates from the adjustment model applied to the network transformation which is determined with rather little degrees of freedom of approximately 15 to 25 (depending on the number of network points per epoch). The Formula of Welch-Satterthwaithe (2.29) is unsuitable in this regard, since the uncertainty contributions are not summarised via variance-propagation but via MCM where one model (the model of network transformation) is nested in the other model (the adjustment model). Furthermore, the additional contributors in (5.20) are estimated by simulations and are therefore attached with infinite degrees of freedom. As a consequence, the DoF values of the adjustment model are used for this analysis, as they are likely to reflect the redundancy best.

Statistical tests are carried out between all materials while the angle of incidence is fixed. In addition, for each material the uncertainty of $IA = 0$ is tested against the uncertainties of all other angles of incidence. No significant differences in uncertainties were found in any of the tests performed. Hence, the uncertainties of the distance differences can be replaced by a single uncertainty value. This general standard uncertainty for all investigated materials and the range of covered incidence angles is specified with 0.2 mm. Based on that, it is concluded that material and incidence angle have a subordinate influence on the uncertainty of distance differences. The larger share is expected to be caused by the geometry of the high-accuracy network, the instruments and the model of network transformation.

6.3. Validation

Validation of the final uncertainties of distance differences is possible due to the availability of an empirical dispersion of distance differences. This dispersion arises from the individual values of distance differences for each corresponding pair of scan points. After the transformation of the scans into one joint coordinate system, distance differences ΔD_i as displayed in Chapter 3.2.4 are calculated for each pair of scan points.

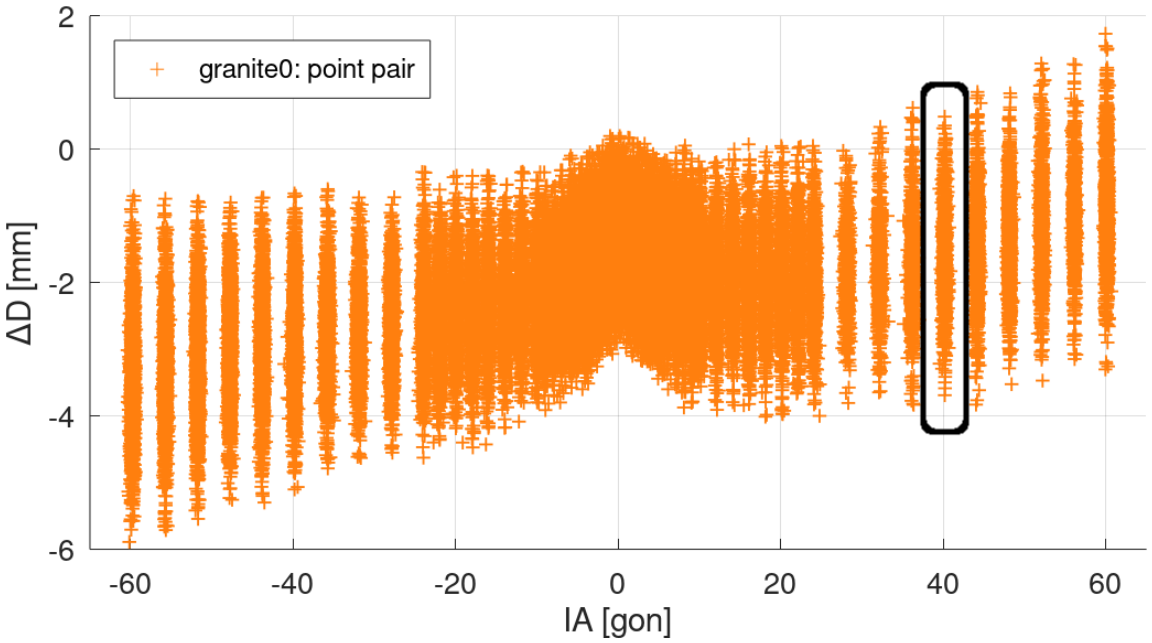

Figure 6.4.: Distance differences ΔD for all point pairs of the scanned object plate 'granite0'. Distance differences inside the black rectangle at $IA = 40$ gon are analysed in Figure 6.6.

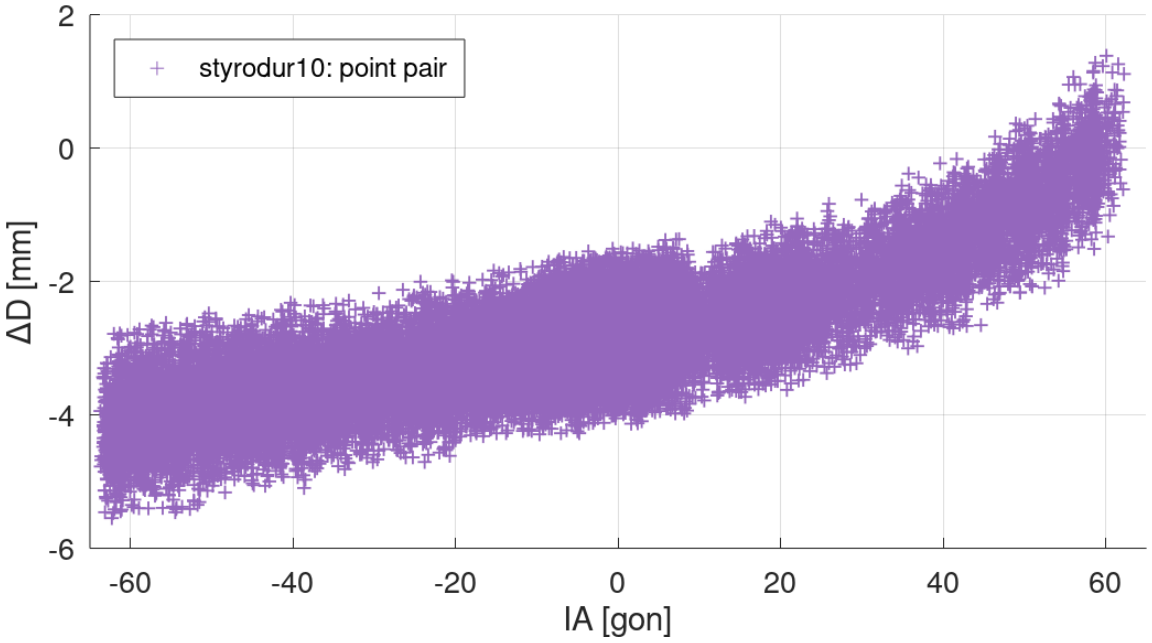

Figure 6.5.: Distance differences ΔD for all point pairs of the scanned object plate 'styrodur10'.

Figures 6.4 and 6.5 show these distance differences of all pairs of scan points as a function of incidence angle exemplarily for two object materials. Though the measurement procedure is identical for all object samples, the resulting distance differences show obvious distinctions. The values of the granite plate are spread over a larger range. Besides, the investigated discrete angles of incidence are clearly perceptible in the plot for the granite plate as vertically oriented clusters, while in Fig. 6.5 the distance differences of individual incidence angles overlap each other and result in a blurry structure. The reason for this is the different roughness of the material samples. Furthermore the plot in Fig. 6.4 indicates that a focus is upon incidence angles close to zero (experiments with higher IA-resolution). The most notably linear systematic in the data is caused by the TLS axis eccentricity.

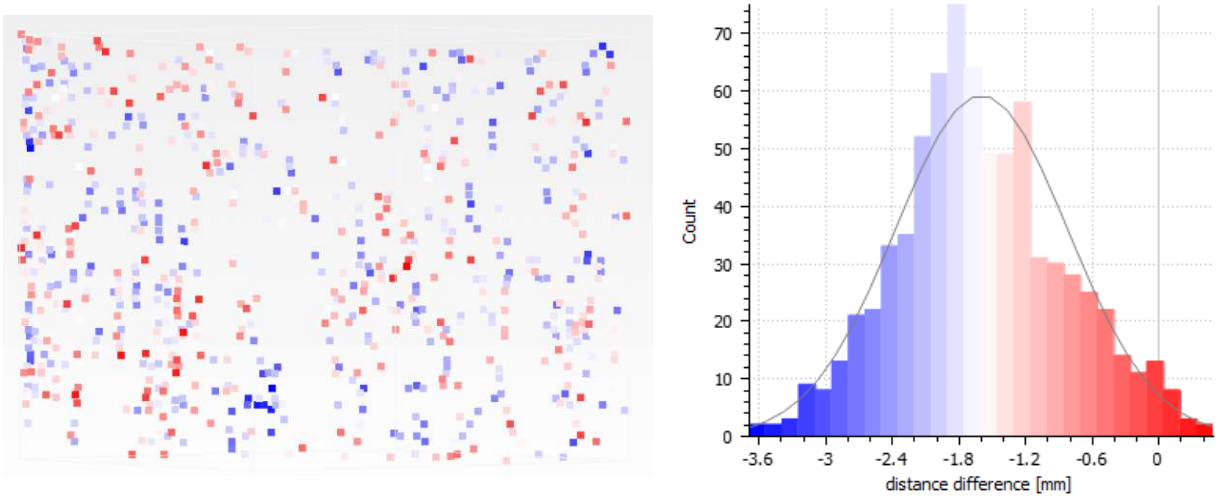

Figure 6.6.: Spatial distribution of the scan point pairs for $IA = 40\,\text{gon}$ of 'granite0'. The colour scheme corresponds to the histogram on the right side, which visualises the distribution of ΔD values for the selected situation.

In order to justify the building of mean value and standard deviation as representatives for the distance differences of all point pairs per angle of incidence, the internal distribution of ΔD values is analysed for some incidence angles and materials. Exemplarily, Figure 6.6 shows a histogram of all 'granite0' distance differences assigned to an angle of incidence of 40 gon. These values correspond to the data points inside the black rectangle in Figure 6.4. As can be seen, the distribution of ΔD values does not fit completely to the indicated Gaussian distribution, which is estimated from the data. However, the deviations to the Gaussian distribution are considered to be small enough, to still justify the derivation of mean value and standard deviation. The left plot of Figure 6.6 illustrates the spatial distribution of the scan point pairs on the object, colour-coded with the computed distance differences. No geometric systematics or spatial accumulations of high or low values are recognisable.

When deriving geometrical information from point clouds measured by scanners, the generated data (distances, lines, planes, shapes) are normally based on a large number of points. Hence, the uncertainty of the derived geometries rests upon the joint uncertainty of all contributing points. Transferring that idea onto the existing distance differences, the standard deviation of the mean value of distance differences $\sigma_{\Delta D_m}$ is more expressive than the standard deviation of distance differences between single pairs of scan points.

According to the Equations (3.4) and (3.5) in Chapter 3.2.4, the mean over all distance differences along with its standard deviation is computed for each angle of incidence. Due to large sample sizes of several hundred point correspondences per incidence angle, the derived statistical values can be viewed as reliable. Figure 6.7 shows the resulting averages of distance differences along with their derived uncertainties. Due to the large

number of point pairs, the standard uncertainties of the mean distance differences are extremely small. In order to make the differences related to IA visually perceptible, the intervals of $\pm 20\,\sigma$ (standard uncertainty times 20) are displayed instead.

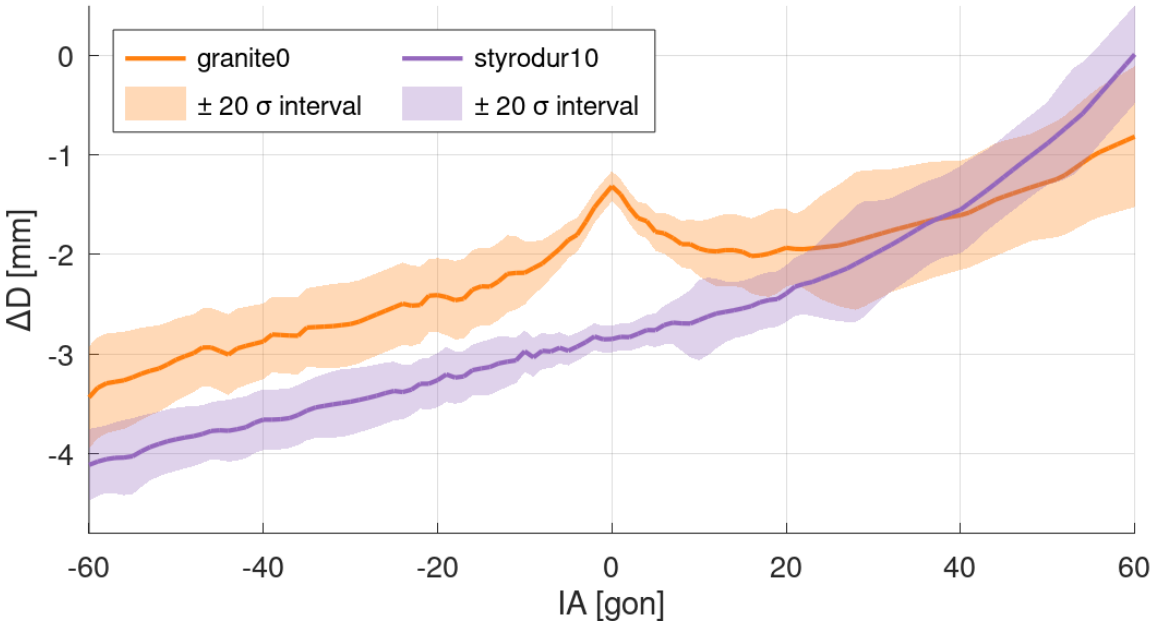

Figure 6.7.: Mean distance differences and their related $\pm 20\sigma$ intervals for the two material samples 'granite0' and 'styrodur10'.

The mean distance differences show a different behaviour especially at angles of incidence close to zero. This is also the area where the corresponding uncertainties are lowest. With increasing angle of incidence (in positive as well as in negative direction), the ranges created by the $20\,\sigma$ intervals become larger.

In order to eliminate the linear trend in the mean distance differences, values of the same positive and negative incidence angle are averaged as formulated in Equation (5.18). This also enables the possibility of direct comparison of theoretical and empirical uncertainties. Figures 6.8 and 6.9 show the direct comparison of the computed theoretical and empirical $1\,\sigma$ intervals for two materials. The theoretical interval is equal to the standard uncertainty as derived in Chapter 5 and displayed in Figure 6.1. The empirical interval corresponds to the dispersion of distance differences as illustrated in Figures 6.4 and 6.5. Both intervals represent the standard uncertainty of the mean distance difference per angle of incidence, but not the standard uncertainty of a single distance difference.

The theoretical values overestimate the standard uncertainty of distance differences compared to the empirical values regardless of material and angle of incidence. Possible causes for the nonconformity are:

- pessimistic assumptions for the instrument uncertainties
- non-optimal estimates for the correlations in the stochastic model of the Monte-Carlo method
- non-consideration of potential correlations in propagation steps apart from the Monte-Carlo method
- too pessimistic variance components for the TS(TLS) and LT measurands
- non-optimal transformation model leading to transformation parameters with pessimistic uncertainties

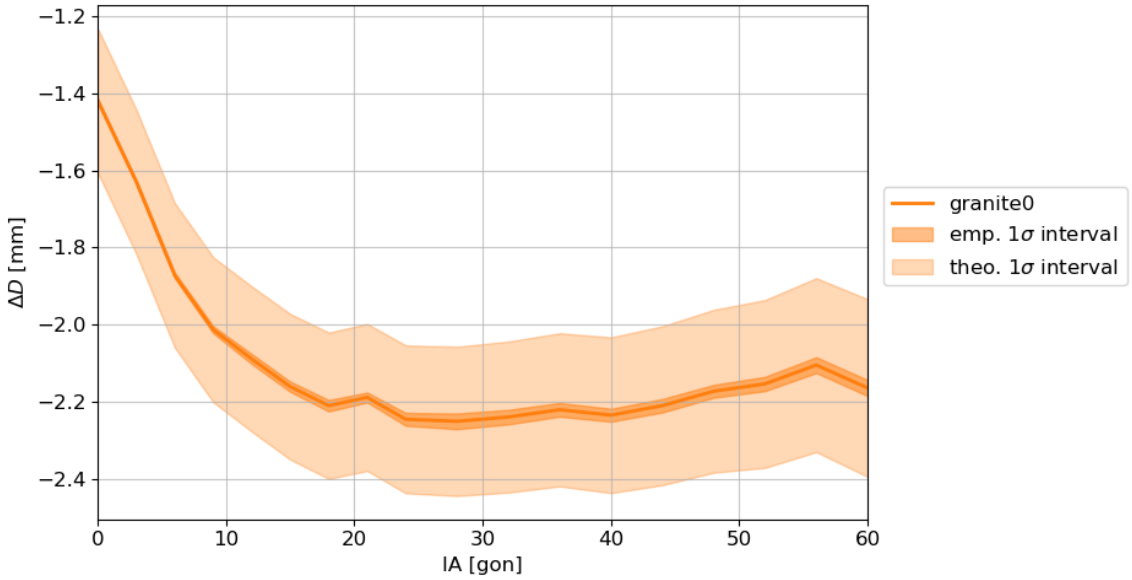

Figure 6.8.: Mean distance differences and their related theoretical and empirical 1σ intervals for the material sample 'granite0'.

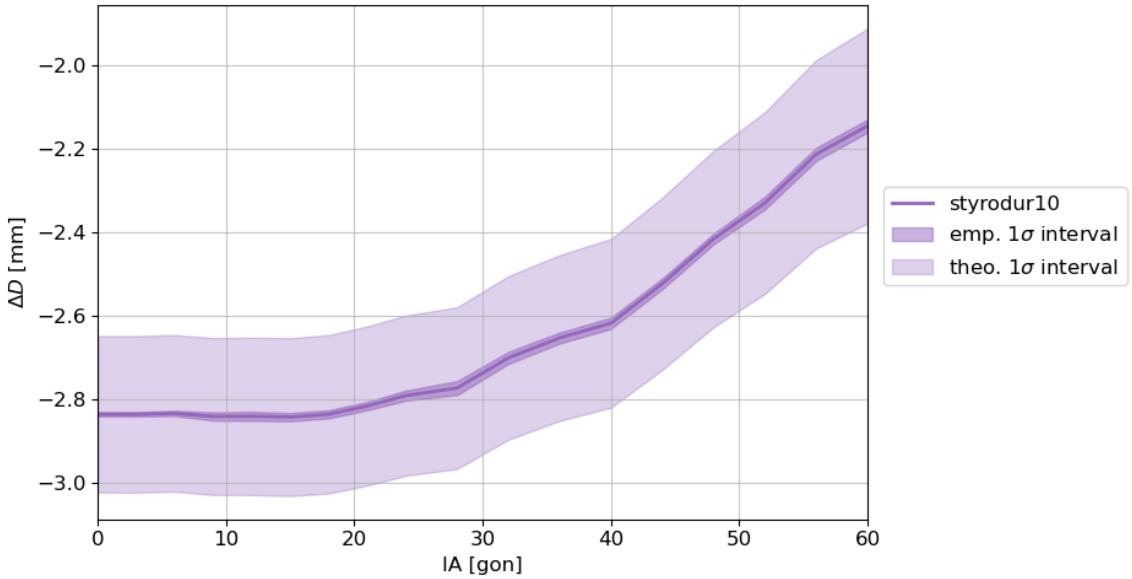

Figure 6.9.: Mean distance differences and their related theoretical and empirical 1σ intervals for the material sample 'styrodur10'.

7. Conclusion

The aim of this work is to assess the uncertainty of TLS distance differences. The distance differences are calculated as differences between reference distances and TLS distances. The necessary instrument setup, the partially automated execution of measurements and the evaluation of the measurements were developed by the Engineering Geodesy research unit at TU Wien and are referred to as ROSIAM.

In this thesis, the entire ROSIAM methodology is examined for sources of uncertainty. Presumed sources of uncertainty are quantified either by experiments or estimated by experience values in the literature. After the determination of all suspected sources of uncertainty, their impacts on the final distance differences are estimated. For most of the uncertainties, this is only possible via intermediate results. The correct transfer of the impact of individual uncertainties onto the distance differences is ensured via variance-covariance propagation or with the help of the Monte Carlo method. Some sources of uncertainty remain without effect on the distance differences since they can be eliminated during the procedure.

Since the ROSIAM methodology relies on a formulaic unknown concept for the network transformation, an own model for the network transformation is developed, which allows to analytically propagate uncertainties. It is based on the known model of Helmert transformation and it holds several advantages. Apart from the crucial benefit of permitting uncertainty propagation, it does not require approximate values. Furthermore, it considers uncertainty information of all input measurands and it does not cause spatial constraints on the instruments providing the measurands.

Experiments for the quantification of individual sources of uncertainty are carried out concerning the reflector, the laser tracker and the terrestrial laser scanner. The experiments show, that the uncertainty specifications given by the manufacturers are generally met.

The uncertainties of some influencing quantities such as the point matching error or the TLS axis eccentricity are estimated by geometric considerations and corresponding simulations of expected uncertainties. Wherever uncertainties are available by different sources (data sheet, empirically determined, simulated), direct comparisons are done for verification. These comparisons show that the uncertainties determined in this work are mostly consistent or slightly pessimistic in contrast to those of other sources.

By merging the impacts of all sources of uncertainty, the distance differences of seven materials and a range of incidence angles from 0 to 60 gon are assigned with standard uncertainties. Significant differences in the distance differences are found between all investigated materials at the majority of incidence angles.

Furthermore, it is noted that the standard uncertainties of TLS distance differences do not differ significantly with regard to material and incidence angle. With a limitation to the investigated materials and to the investigated range of incidence angles, the ROSIAM methodology is capable of determining distance differences with a standard uncertainty of 0.2 mm.

References

Ahad, Nor Aishah and Sharipah Soaad Syed Yahaya (2014). 'Sensitivity analysis of Welch's t-test'. In: *AIP Conference Proceedings*. Vol. 1605. 1. Melville: American Institute of Physics, pp. 888–893. isbn: 9780735412415. doi: 10.1063/1.4887707.

BIPM, IEC, IFCC, ILAC, ISO, IUPAC, IUPAP and OIML (2008a). *Evaluation of measurement data -— Supplement 1 to the "Guide to the expression of uncertainty in measurement" -— Propagation of distributions using a Monte Carlo method*. Joint Committee for Guides in Metrology, JCGM 100:2008. url: https://www.bipm.org/documents/20126/2071204/JCGM_101_2008_E.pdf.

BIPM, IEC, IFCC, ILAC, ISO, IUPAC, IUPAP and OIML (2008b). *Evaluation of measurement data —- Guide to the expression of uncertainty in measurement*. Joint Committee for Guides in Metrology, JCGM 100:2008. url: https://www.bipm.org/documents/20126/2071204/JCGM_100_2008_E.pdf.

Dietmaier, Christopher (2014). 'Koordinatensysteme und Kurven'. In: *Mathematik für angewandte Wissenschaften*. Springer Berlin Heidelberg, pp. 319–344. isbn: 9783827424204.

Donnelly, Robert A. and Fatma Abdel-Raouf (2016). *Statistics*. Third edition. Idiot's guides: as easy as it gets! Indianapolis, Indiana: Alpha. isbn: 1465454098.

Dunn, William L. and J. Kenneth Shultis (2012). *Exploring Monte Carlo methods*. Amsterdam; Boston: Elsevier. isbn: 1283173832.

Eaton, John W. (2022). *About Octave*. url: https://octave.org/about (visited on 20/11/2022).

Förstner, W. (1979). 'Ein Verfahren zur Schätzung von Varianz- und Kovarianzkomponenten'. In: *AVN* 11-12.

Grimm-Pitzinger, Albert and Klaus Hanke (1986). 'Bedeutung der Varianzkomponentenschätzung für die geodätische Praxis'. In: *Österreichische Zeitschrift für Vermessungswesen und Photogrammetrie* 74.2, pp. 101–112.

Gruber, Franz Josoef and Rainer Joeckel (2014). *Formelsammlung für das Vermessungswesen*. Vol. 17. Wien: Springer-Verlag. isbn: 978-3-658-06798-4.

Heunecke, Otto, Heiner Kuhlmann, Walter Welsch, Andreas Eichhorn and Hans Neuner (2013). *Handbuch Ingenieurgeodäsie: Auswertung geodätischer Überwachungsmessungen*. 2. Aufl. Berlin: Wichmann. isbn: 978-3-879-07467-9.

Hexagon Metrology (2011). *Leica Geosystems Metrology Products*. Version 1.1. Germany.

Hexagon Metrology (2013). *System Specifications Leica T-Scan TS50-A*. Germany. url: http://www.geniusinstruments.co.th/custom_file/LeicaTScan.pdf.

Hexagon Metrology (2022). *Absolute Tracker systems and accessories*. Version 3.0. Germany. url: https://go.hexagonmi.com/l/49752/2017-07-05/5t7pmw/49752/1654666941ogPvWeyz/Hexagon_MI_Tracker_Catalogue_3.0_210x210_en_WEB.pdf.

Horvath, Sabine (2014). 'Integration of relative and global orientation methods using a moving ToF camera'.

IAG (1999). *IAG Resolutions*. Birmingham, United Kingdom. url: https://office.iag-aig.org/doc/5d7b8fda0c032.pdf.

Joeckel, Rainer, Manfred Stober and Wolfgang Huep (2008). *Elektronische Entfernungs- und Richtungsmessung und ihre Integration in aktuelle Positionierungsverfahren*. 5. Heidelberg: Wichmann. isbn: 3879074437.

Kaasalainen, Sanna, Anssi Krooks, Antero Kukko and Harri Kaartinen (2009). 'Radiometric Calibration of Terrestrial Laser Scanners with External Reference Targets'. In: *Remote Sensing* 1.3, pp. 144–158. issn: 2072-4292. doi: 10.3390/rs1030144. url: https://www.mdpi.com/2072-4292/1/3/144.

Kersten, Thomas, Klaus Mechelke, Maren Lindstaedt and Harald Sternberg (2008). 'Geometric Accuracy Investigations of the Latest Terrestrial Laser Scanning Systems'. In: *FIG Working Week*. Stockholm: Fédération Internationale des Géomètres. url: http://www.fig.net/resources/proceedings/fig_proceedings/fig2008/papers/ts02d/ts02d_01_mechelke_etal_2785.pdf.

Kirkup, Les and Bob Frenkel (2006). *An introduction to uncertainty in measurement using the GUM (guide to the expression of uncertainty in measurement)*. Cambridge: Cambridge University Press. isbn: 0511755538. doi: 10.1017/CBO9780511755538.

Krabs, Werner (1979). *Optimization and approximation*. A Wiley-Interscience publication. Chichester: Wiley. isbn: 0471997412.

Kramer, Jürg and Anna-Maria von Pippich (2022). *Von den natürlichen Zahlen zu den Quaternionen: Basiswissen Zahlbereiche und Algebra*. 2nd ed. Wiesbaden: Springer. isbn: 3658366214. doi: 10.1007/978-3-658-36621-6.

Lachat, Elise, Tania Landes and Pierre Grussenmeyer (2017). 'Investigation of a Combined Surveying and Scanning Device: The Trimble SX10 Scanning Total Station'. In: *Sensors* 17.4. issn: 1424-8220. doi: 10.3390/s17040730. url: https://www.mdpi.com/1424-8220/17/4/730.

Leica Geosystems (2017). *Leica Nova MS60 white paper*. Heerbrugg, Switzerland. url: https://leica-geosystems.com/-/media/files/leicageosystems/products/datasheets/leica-nova-ms60-whp-lr.ashx.

Leica Geosystems (2020). *Leica Nova MS60 Data sheet*. Heerbrugg, Switzerland. url: https://leica-geosystems.com/-/media/files/leicageosystems/products/datasheets/leica_nova_ms60_ds.ashx.

Leica Geosystems (n.d.). *Leica Laser Tracker for Hand-Tools LT(D)800 Data sheet*. Unterentfelden, Switzerland. url: https://www.sigma3d.de/fileadmin/Webseiten-Daten/Dokumente/VermietungProduktPDFs/Vermietung_Lasertracker_Leica_LT_D_800.pdf.

Lichti, D, MP Stewart, M Tsakiri and AJ Snow (2000). 'Calibration and testing of a terrestrial laser scanner'. In: *International archives of Photogrammetry and Remote sensing* 33.PART B5, pp. 485–492.

Linzer, Finn, Miriam Papčová and Hans Neuner (2021). 'Quantification of Systematic Distance Deviations for Scanning Total Stations Using Robotic Applications'. In: *Contributions to International Conferences on Engineering Surveying*. Ed. by Alojz Kopáčik, Peter Kyrinovič, Ján Erdélyi, Rinaldo Paar and Ante Marendić. Cham: Springer, pp. 98–108. isbn: 978-3-030-51953-7. url: https://doi.org/10.1007/978-3-030-51953-7_8.

New River Kinematics (2020). *SpatialAnalyzer User Manual*. Williamsburg, VA. url: https://spatialanalyzer.com/ftp/SA/Install/Documentation/SA%20User%20Manual_2020.07.20.pdf.

Niemeier, Wolfgang (2008). *Ausgleichungsrechnung : statistische Auswertemethoden*. 2. edition. Berlin: de Gruyter. isbn: 9783110190557. doi: 10.1515/9783110206784.

Pesch, Bernd (2003). *Bestimmung der Messunsicherheit nach GUM*. Grundlagen der Metrologie. Norderstedt [u.a.]: Books on Demand. isbn: 3833010398.

Python Software Foundation (2022). *General Python FAQ*. url: https://docs.python.org/3/faq/general.html (visited on 20/11/2022).

Revue Thommen AG (n.d.). *Meteo Station HM30*. Waldenburg, Switzerland. url: https://www.huber-instrumente.com/cms/upload/imgfile534.pdf.

Riffenburgh, Robert H. and Daniel L. Gillen (2020). 'Tests on variability and distributions'. In: *Statistics in Medicine*. Elsevier Inc, pp. 311–336. isbn: 0128153296. doi: 10.1016/B978-0-12-815328-4.00013-9.

Staiger, Rudolf (2011). '10 years of terrestrial Laser Scanning technology, systems and applications'. In: *Интерэкспо Гео-Сибирь* Пленарное заседание, pp. 43–55.

Stanford Artificial Intelligence Laboratory et al. (2022). *Robotic Operating System*. url: https://www.ros.org.

Trefethen, Lloyd N and David Bau (1997). *Numerical linear algebra*. Philadelphia, PA: SIAM. isbn: 978-0-89-871487-6.

Universal Robots (2016). *UR5 Technical specifications*. Odense, Denmark. url: https://www.universal-robots.com/media/50588/ur5_en.pdf.

Vince, John (2022). *Mathematics for Computer Graphics*. 6th ed. Undergraduate Topics in Computer Science. London: Springer. isbn: 1447175204. doi: 10.1007/978-1-4471-7520-9.

Voegtle, Thomas, I. Schwab and T. Landes (2008). 'Influences of different materials on the measurements of a terrestrial laser scanner (TLS)'. In: *Proc. of the XXI Congress, The International Society for Photogrammetry and Remote Sensing, ISPRS2008*. Vol. 37. Beijing, pp. 1061–1066. url: https://www.isprs.org/proceedings/XXXVII/congress/5_pdf/182.pdf.

Wyszkowska, Patrycja (2017). 'Propagation of uncertainty by Monte Carlo simulations in case of basic geodetic computations'. In: *Geodesy and Cartography* 66.2. doi: 10.1515/geocart-2017-0022.

Zámečníková, Miriam and Hans Neuner (2018). 'Methods for quantification of systematic distance deviations under incidence angle with scanning total stations'. In: *Journal of Photogrammetry and Remote Sensing* 144, pp. 268–284. issn: 0924-2716. doi: 10.1016/j.isprsjprs.2018.07.008. url: https://www.sciencedirect.com/science/article/pii/S0924271618302004.

Zámečníková, Miriam, Hans Neuner and Stefan Pegritz (2014a). 'Influence of the Incidence Angle on the Reflectorless Distance Measurement in Close Range'. In: *INGEO 2014 - Proceedings of the 6th International Conference on Engineering Surveying*. Czech Technical University Prague, Faculty of Civil Engineering, pp. 257–262. isbn: 9788001054697. url: https://publik.tuwien.ac.at/files/PubDat_229161.pdf.

Zámečníková, Miriam, Andreas Wieser, Helmut Woschitz and Camillo Ressl (2014b). 'Influence of surface reflectivity on reflectorless electronic distance measurement and terrestrial laser scanning'. In: *Journal of Applied Geodesy* 8.4, pp. 311–325. issn: 0924-2716. doi: 10.1515/jag-2014-0016.

List of Acronyms

ADM	Absolute Distance Meter
ATR	Automatic Target Recognition
CCR	Corner Cube Reflector
EDM	Electronic Distance Measurement
DoF	Degree of Freedom
GHM	Gauss Helmert Model
GMM	Gauss Markov Model
GUM	Guide to the Expression of Uncertainty in Measurement
HS	Handheld Scanner
IUGG	International Union of Geodesy and Geophysics
LT	Laser Tracker
MCM	Monte Carlo Method
PDF	Probability Density Function
ROSIAM	Robot Operating System for investigating Incidence Angle and Material
SA	SpatialAnalyzer
SBI	Spatial Backward Intersection
TLS	Terrestrial Laser Scanner
TS(TLS)	Total Station (as part of the Multi Station)
USMN	Unified Spatial Metrology Network
VCE	Variance Component Estimation
VCM	Variance-Covariance Matrix
VCP	Variance-Covariance Propagation

List of Figures

2.1. Schematic process of uncertainty propagation using the MCM (adapted from BIPM *et al.* 2008a) 11
2.2. Accuracy specifications (1σ-values) and technical characteristics of the used multi station Leica MS60 stated by the manufacturer (Leica Geosystems 2020). 13
2.3. Accuracy specifications (1σ-values) and technical properties of the used laser tracker Leica LTD 800 stated by the manufacturer (Leica Geosystems n.d.). 14
2.4. Accuracy specifications (1σ-values) and technical characteristics of the used handheld scanner Leica T-Scan TS50-A stated by the manufacturer (Hexagon Metrology 2013). 15
2.5. Specifications of Leica Red Ring Reflector 1.5″ (Hexagon Metrology 2022). 15
2.6. Specifications of robot arm UR5 (Universal Robots 2016) 16
2.7. USMN composite point. Errors between total station and laser tracker measurements are exaggerated for clarity. (taken from New River Kinematics 2020) 17

3.1. Floor plan of the measurement laboratory (GUT TU Wien). The target points, realising a high-accuracy network, are highlighted and attached with their target names. 19
3.2. A spherical reflector inserted at consoles realises a point of the high-accuracy network. 20
3.3. Overview of the geometrical measurement setup of ROSIAM system. 20
3.4. Flow diagram of the measurement part of ROSIAM procedure (taken from: Linzer *et al.* (2021)) 21
3.5. Quasi-simultaneous measurements to common network measurements enable the derivation of a spatial relationship between LT and TS(TLS). 21
3.6. Scan configuration of the ROSIAM procedure. 22
3.7. Robot arm panning the HS along the object plate for the acquisition of a reference point cloud. . 23

5.1. Fishbone diagram listing sources of uncertainty which are relevant for the determination of the uncertainty of distance differences ΔD 29
5.2. Repeatability of LT measurements on CCR target. 34
5.3. Reproducibility of LT measurements on CCR target. 34
5.4. The corner cube reflector is positioned at a console with its company branding pointing upwards. The red arrow indicates the reflector's direction of rotation. 35
5.5. Deviations to the mean values in the CCR roundness experiment for Hz_{LT}, V_{LT} and d_{LT}. 35
5.6. Illumination of the corner cube reflector by white and green light. The visual impurities on the cube surfaces are caused by dust particles. 37
5.7. Sketch of the TLS scan setup with particular emphasis to the coordinate system in relation to the scanned object. 44
5.8. Sketch displaying the effect of an uncertainty in X-translation onto distance deviations 45
5.9. Sketch displaying the effect of an uncertainty in Z-rotation angle (κ) onto distance deviations. . 45
5.10. Simulated influence curves of uncertainties in the transformation parameters onto uncertainties of ΔD. A mean scan distance of 30 m is assumed. The magnitude of the input uncertainties (uncertainties of the transformation parameters) correspond to the standard uncertainties generated by the Monte Carlo method. 46

5.11. Scan points are matched according to the lowest deviation in Hz and V (adapted from Linzer *et al.* (2021)) . . . 46
5.12. The maximum point matching error $\zeta_{\Delta D}$ is dependent on the angle of incidence (IA) and the maximum point spacing Δx perpendicular to the line of sight. . . . 47
5.13. Characteristic curves marking the maximum permissible angle deviations in order to not exceed a distance error ($\zeta_{\Delta D}$) of 0.06 mm . . . 48
5.14. Eccentricity ε between distance axis and collimation axis and its effect on distance differences $\varepsilon_{\Delta D}$. (a) exaggerated sketch; (b) simulation of the influence under incidence angle ($\varepsilon = 2$ mgon, $D = 30$ m) (adapted from Zámečníková *et al.* (2018)) . . . 49

6.1. Distance differences and the corresponding 1σ intervals for all investigated materials. Suffixed numbers to the materials are used to distinguish between different levels of surface roughness of the same kind of material. . . . 53
6.2. Distance differences ΔD and corresponding 1σ intervals for two materials. Significant differences in ΔD are marked by the bar at the bottom. . . . 55
6.3. Distance differences ΔD and corresponding 1σ intervals for two materials. Incidence angles with significant differences in ΔD are marked by the bar at the bottom. . . . 55
6.4. Distance differences ΔD for all point pairs of the scanned object plate 'granite0'. Distance differences inside the black rectangle at $IA = 40$ gon are analysed in Figure 6.6. . . . 57
6.5. Distance differences ΔD for all point pairs of the scanned object plate 'styrodur10'. . . . 57
6.6. Spatial distribution of the scan point pairs for $IA = 40$ gon of 'granite0'. The colour scheme corresponds to the histogram on the right side, which visualises the distribution of ΔD values for the selected situation. . . . 58
6.7. Mean distance differences and their related $\pm 20\sigma$ intervals for the two material samples 'granite0' and 'styrodur10'. . . . 59
6.8. Mean distance differences and their related theoretical and empirical 1σ intervals for the material sample 'granite0'. . . . 60
6.9. Mean distance differences and their related theoretical and empirical 1σ intervals for the material sample 'styrodur10'. . . . 60

A.2. Images of the scanned materials . . . 74

B.1. Distance differences ΔD, corresponding 1σ intervals and significance result for two materials. . 75
B.2. Distance differences ΔD, corresponding 1σ intervals and significance result for two materials. . 76
B.3. Distance differences ΔD, corresponding 1σ intervals and significance result for two materials. . 76
B.4. Distance differences ΔD, corresponding 1σ intervals and significance result for two materials. . 77
B.5. Distance differences ΔD, corresponding 1σ intervals and significance result for two materials. . 77
B.6. Distance differences ΔD, corresponding 1σ intervals and significance result for two materials. . 78
B.7. Distance differences ΔD, corresponding 1σ intervals and significance result for two materials. . 78
B.8. Distance differences ΔD, corresponding 1σ intervals and significance result for two materials. . 79
B.9. Distance differences ΔD, corresponding 1σ intervals and significance result for two materials. . 79
B.10. Distance differences ΔD, corresponding 1σ intervals and significance result for two materials. . 80
B.11. Distance differences ΔD, corresponding 1σ intervals and significance result for two materials. . 80
B.12. Distance differences ΔD, corresponding 1σ intervals and significance result for two materials. . 81
B.13. Distance differences ΔD, corresponding 1σ intervals and significance result for two materials. . 81
B.14. Distance differences ΔD, corresponding 1σ intervals and significance result for two materials. . 82
B.15. Distance differences ΔD, corresponding 1σ intervals and significance result for two materials. . 82

B.16.Distance differences ΔD, corresponding 1σ intervals and significance result for two materials. . 83
B.17.Distance differences ΔD, corresponding 1σ intervals and significance result for two materials. . 83
B.18.Distance differences ΔD, corresponding 1σ intervals and significance result for two materials. . 84
B.19.Distance differences ΔD, corresponding 1σ intervals and significance result for two materials. . 84
B.20.Distance differences ΔD, corresponding 1σ intervals and significance result for two materials. . 85
B.21.Distance differences ΔD, corresponding 1σ intervals and significance result for two materials. . 85

A. Scanned Materials

The subsequently displayed materials are investigated as scan objects. The surfaces of some objects are divided into subareas with different surface roughness parameters. Therefore, the names of materials are suffixed by a number in order to distinguish objects of identical material but diverse surface roughness. Low integer suffixes denote rather smooth-surfaced objects while rough surfaces are indicated by larger numbers.

(a) steel 3

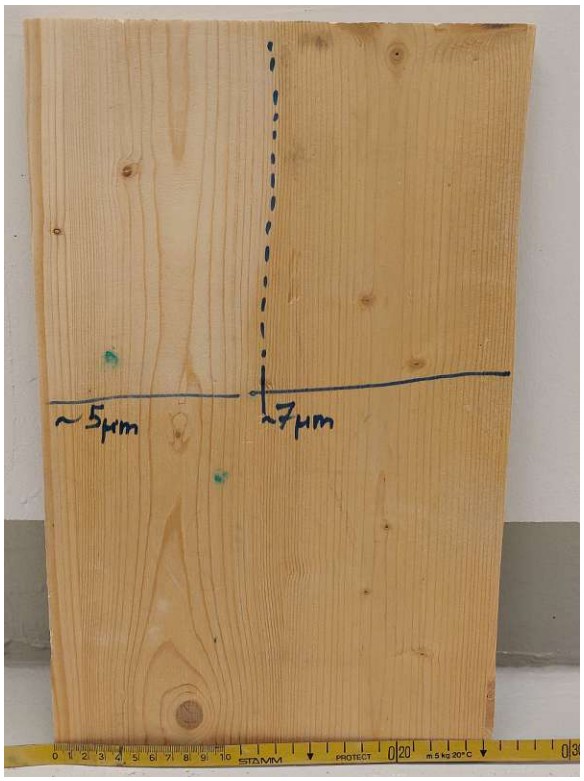

(b) wood 5 (upper left area)

(c) granite 0 (center area)

(d) granite 10 (upper left area)

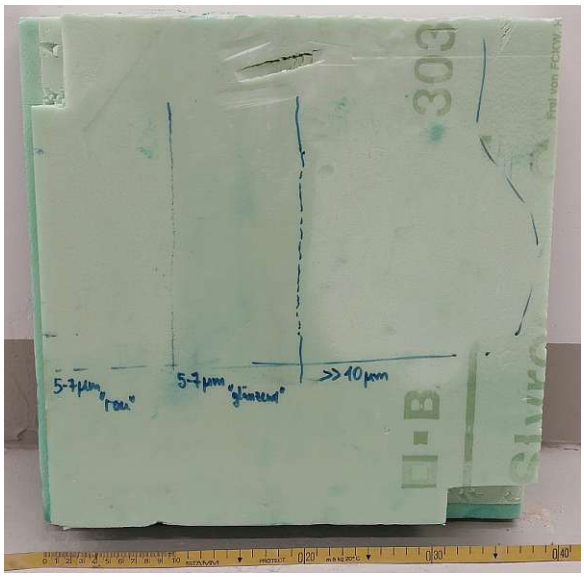

(e) styrodur 5 (left area) styrodur 10 (right area)

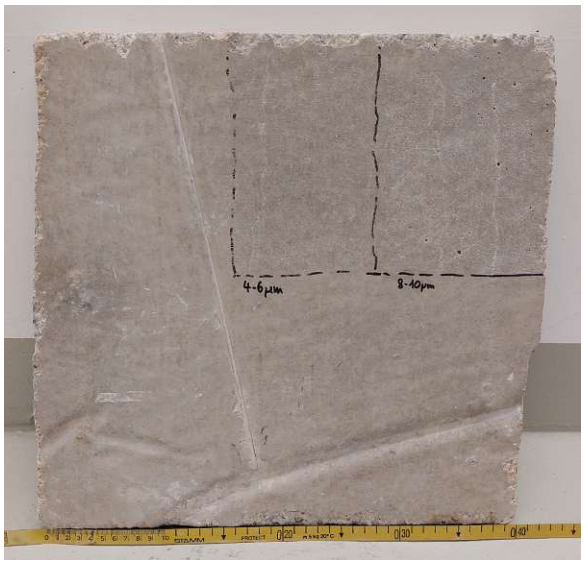

(f) concrete 4 (upper center area)

Figure A.2.: Images of the scanned materials

B. Results: Distance Differences and Uncertainties

This part of the appendix contains figures of all possible pairs of investigated materials. Each plot shows the distance differences as derived by the ROSIAM methodology for two materials together with the derived standard uncertainties in this work. The uncertainties are illustrated as 1σ intervals around the curves of distance differences. Additionally, a bar at the bottom of each plot indicates areas of incidence angles, where significant or insignificant differences in ΔD are found. The corresponding statistical tests are carried out at a level of confidence of 0.95.

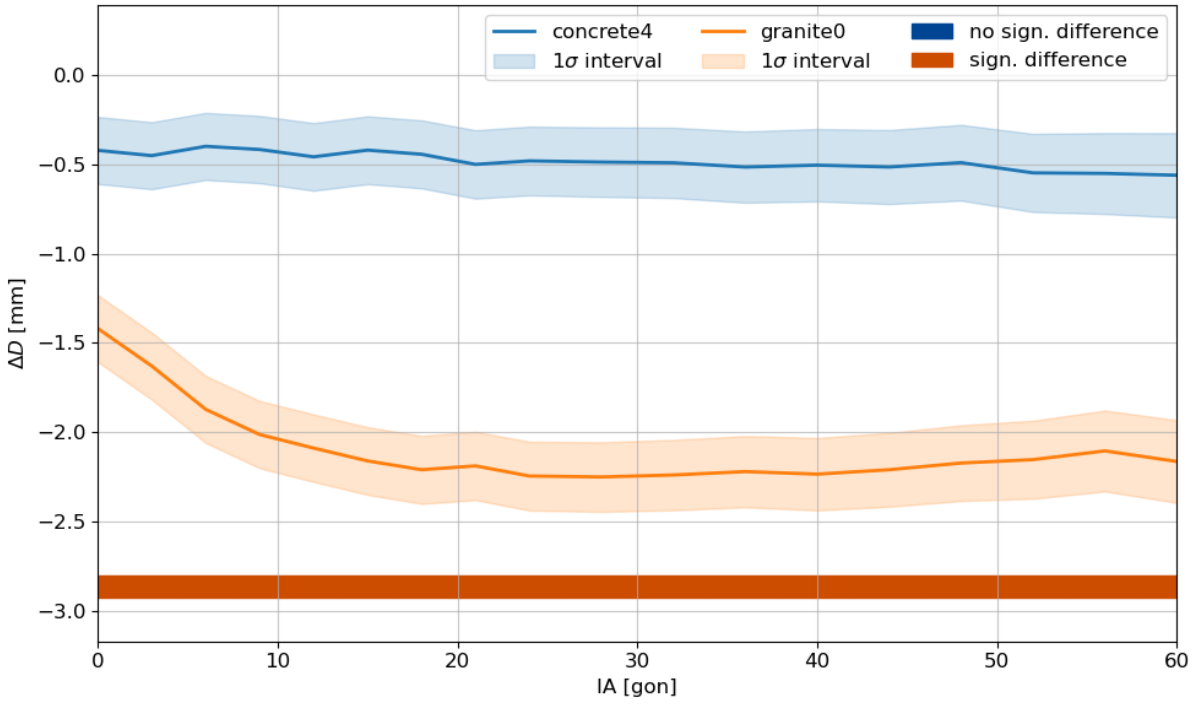

Figure B.1.: Distance differences ΔD, corresponding 1σ intervals and significance result for two materials.

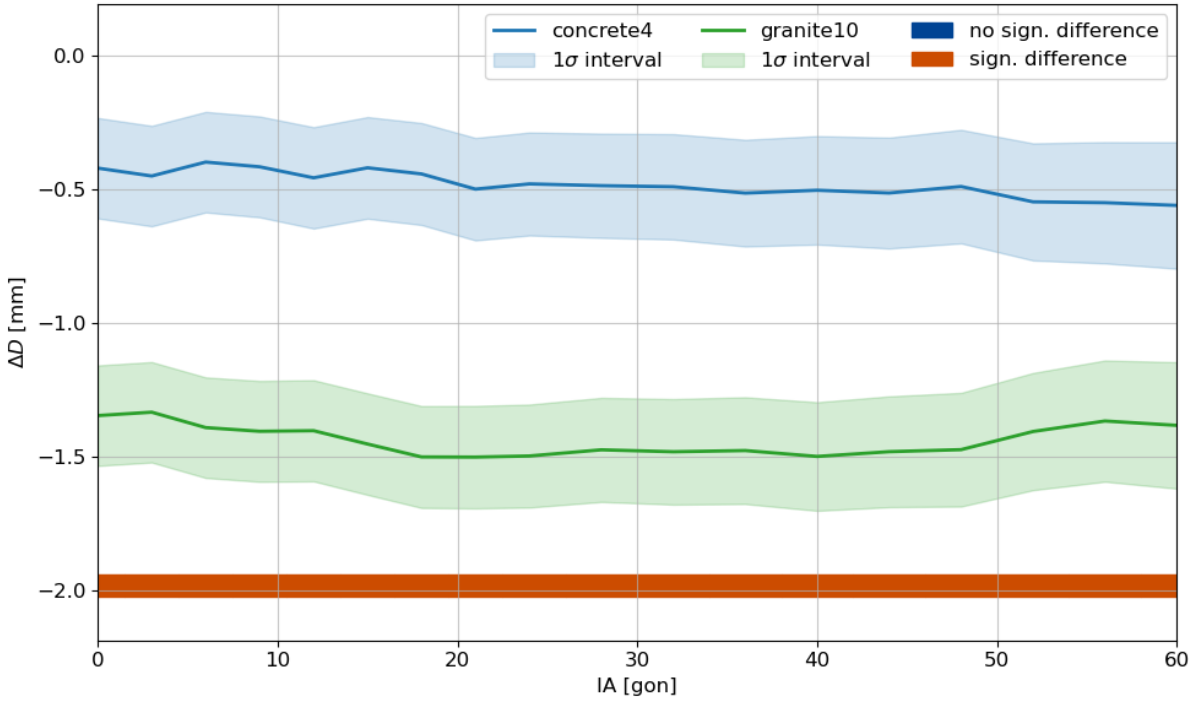

Figure B.2.: Distance differences ΔD, corresponding 1σ intervals and significance result for two materials.

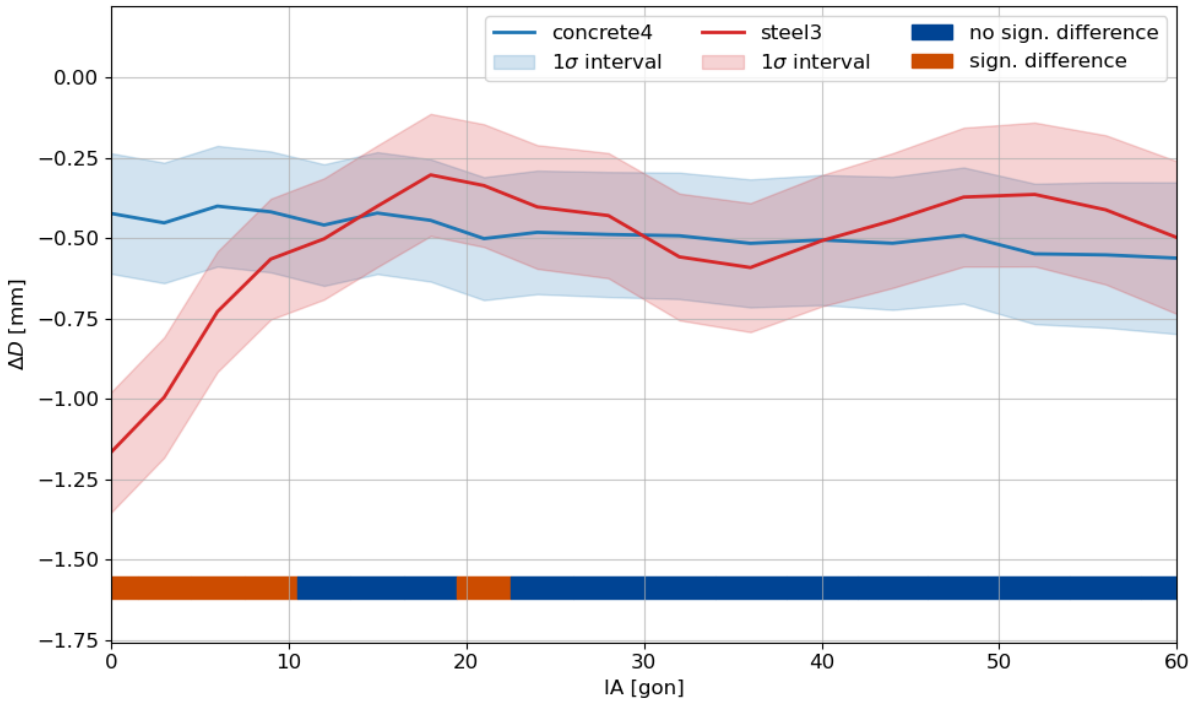

Figure B.3.: Distance differences ΔD, corresponding 1σ intervals and significance result for two materials.

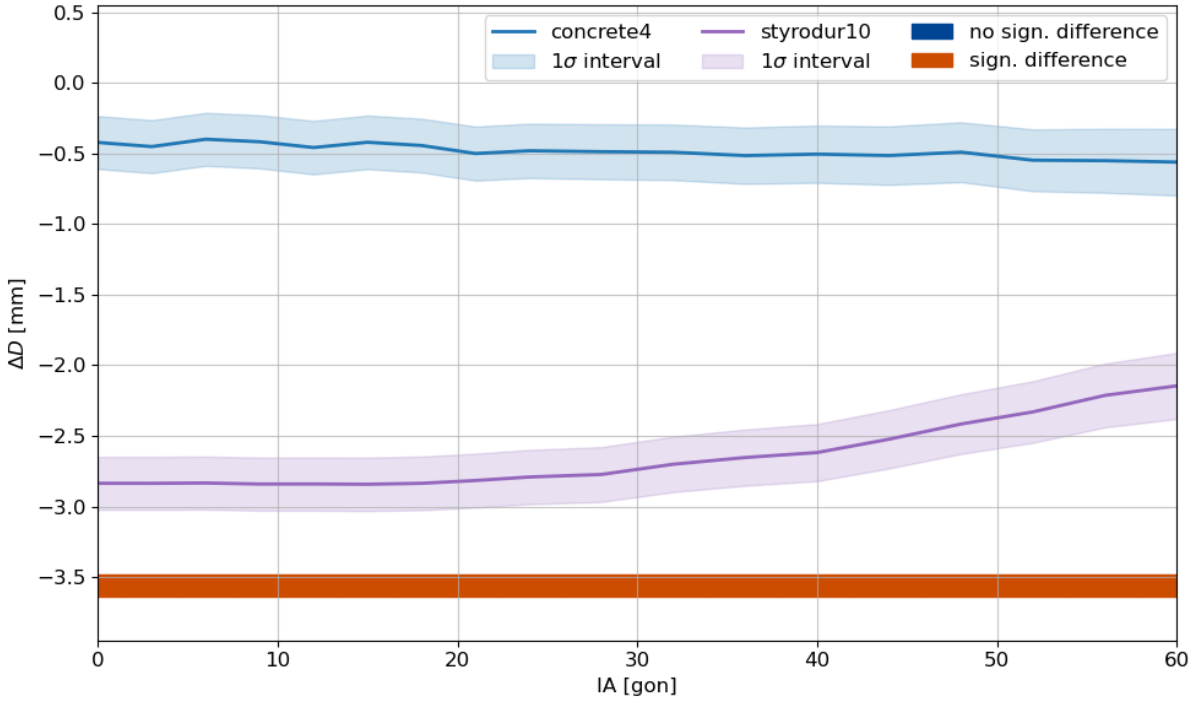

Figure B.4.: Distance differences ΔD, corresponding 1σ intervals and significance result for two materials.

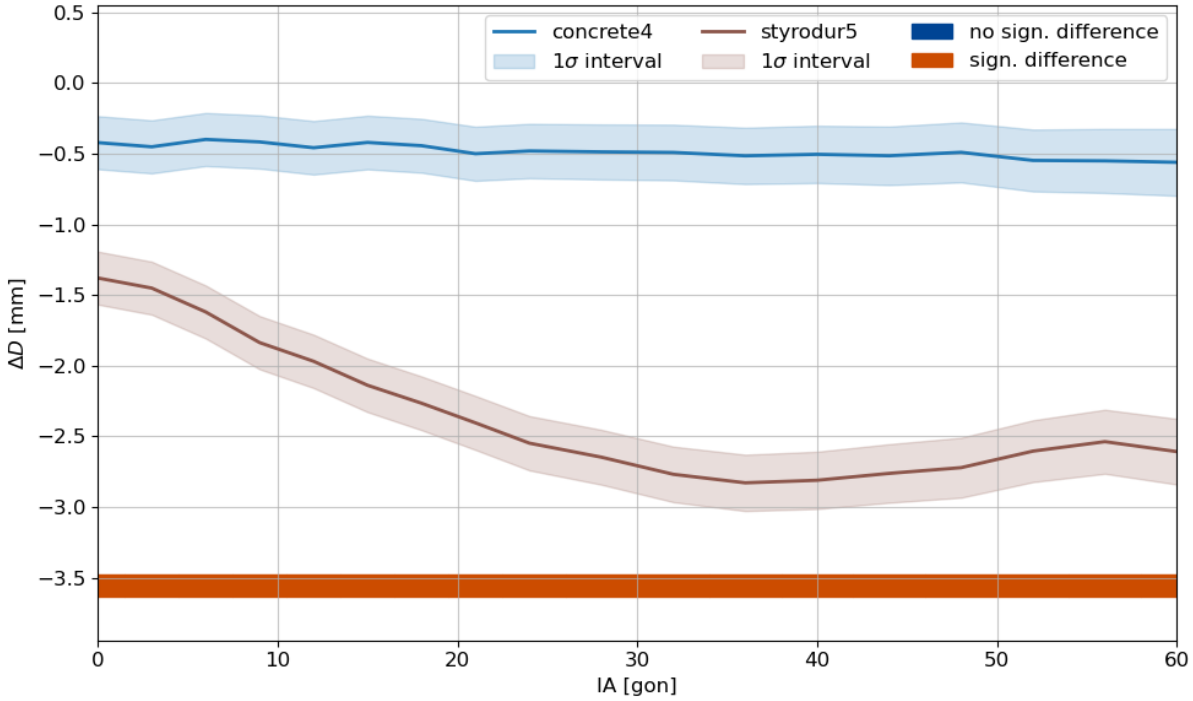

Figure B.5.: Distance differences ΔD, corresponding 1σ intervals and significance result for two materials.

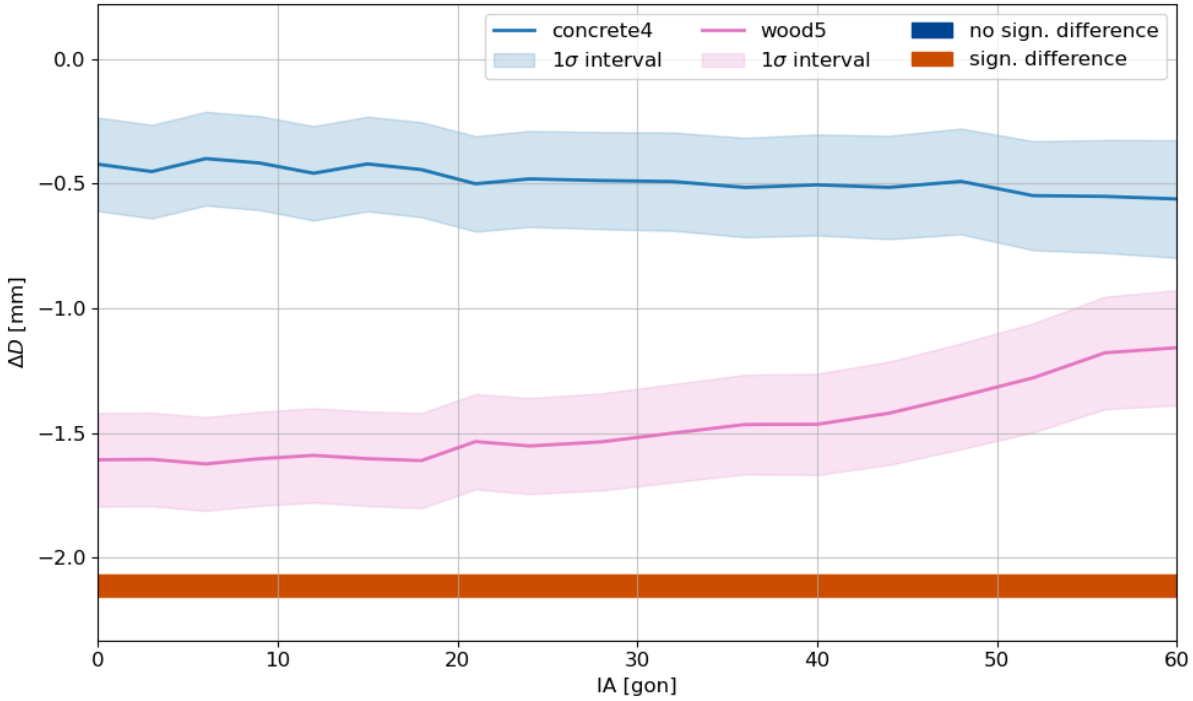

Figure B.6.: Distance differences ΔD, corresponding 1σ intervals and significance result for two materials.

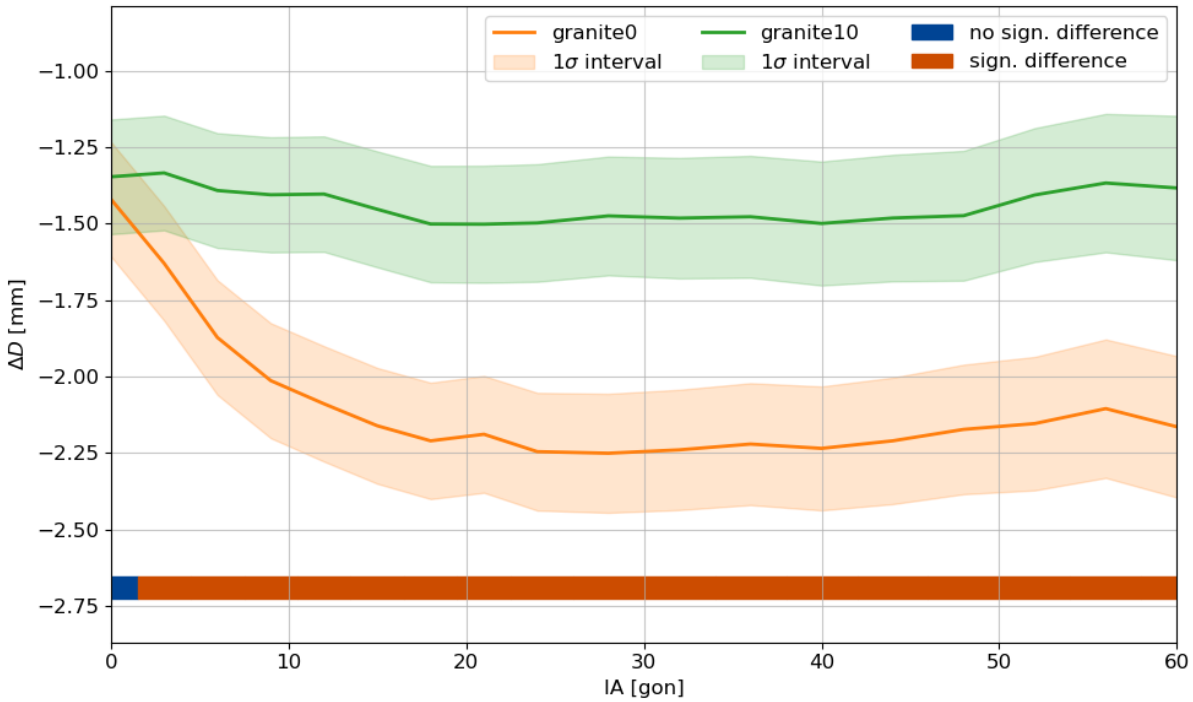

Figure B.7.: Distance differences ΔD, corresponding 1σ intervals and significance result for two materials.

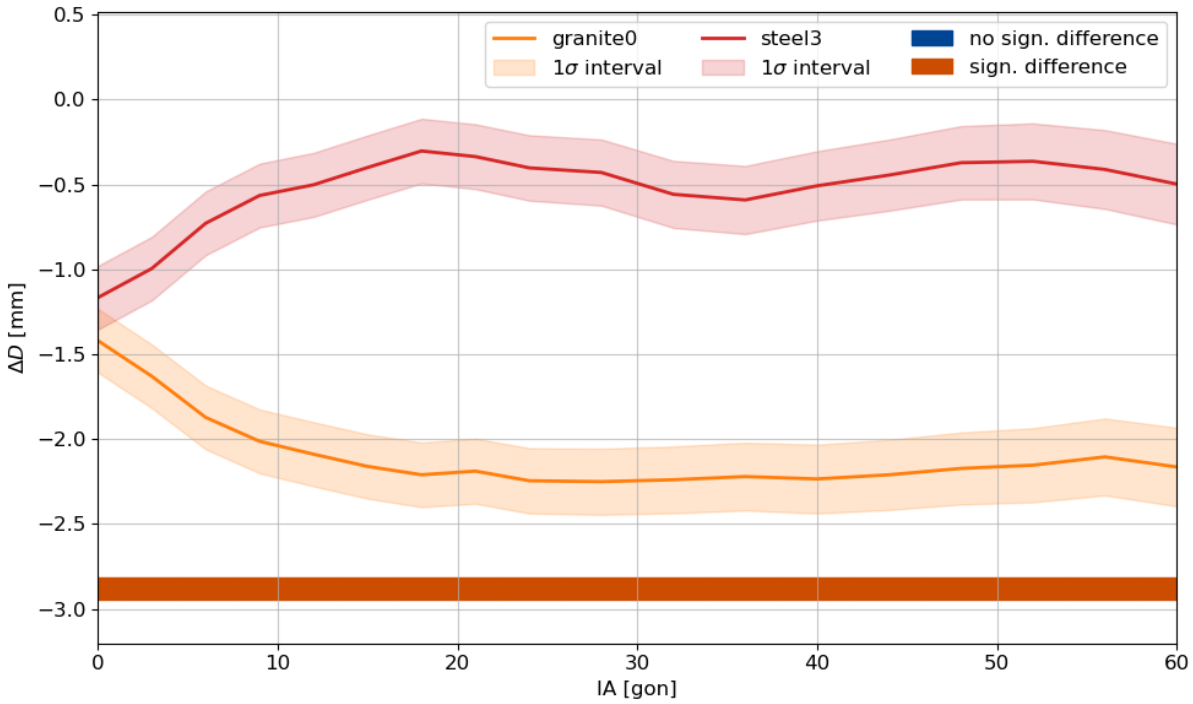

Figure B.8.: Distance differences ΔD, corresponding 1σ intervals and significance result for two materials.

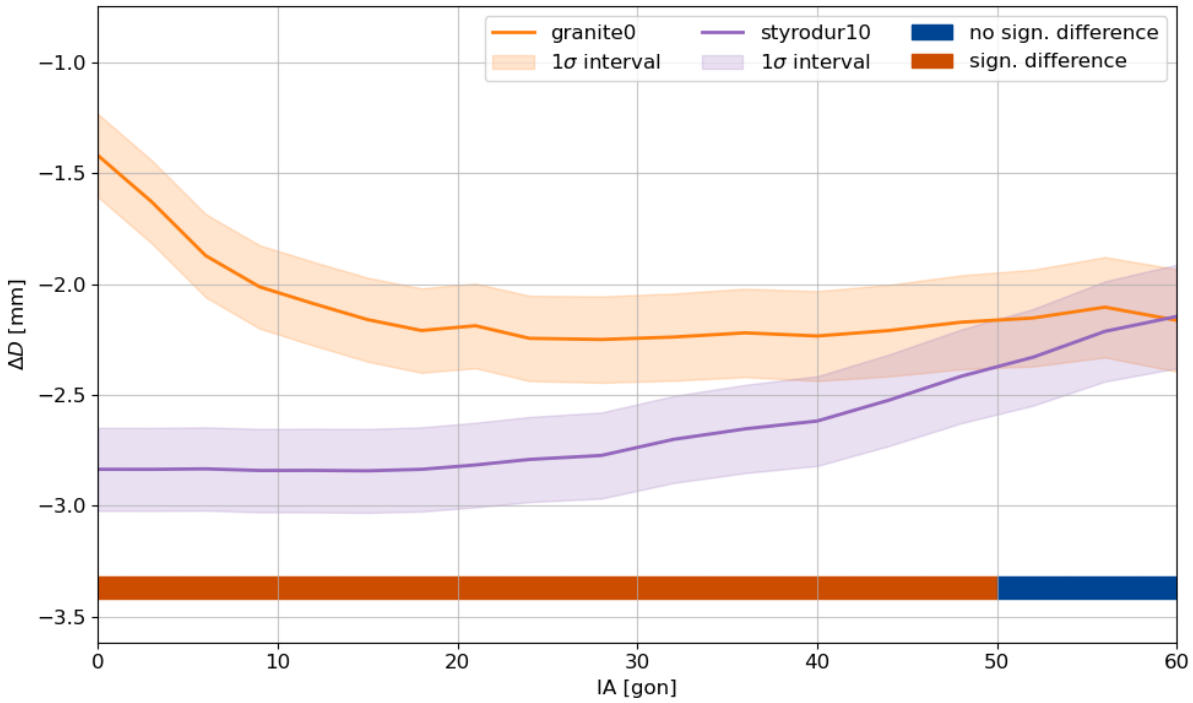

Figure B.9.: Distance differences ΔD, corresponding 1σ intervals and significance result for two materials.

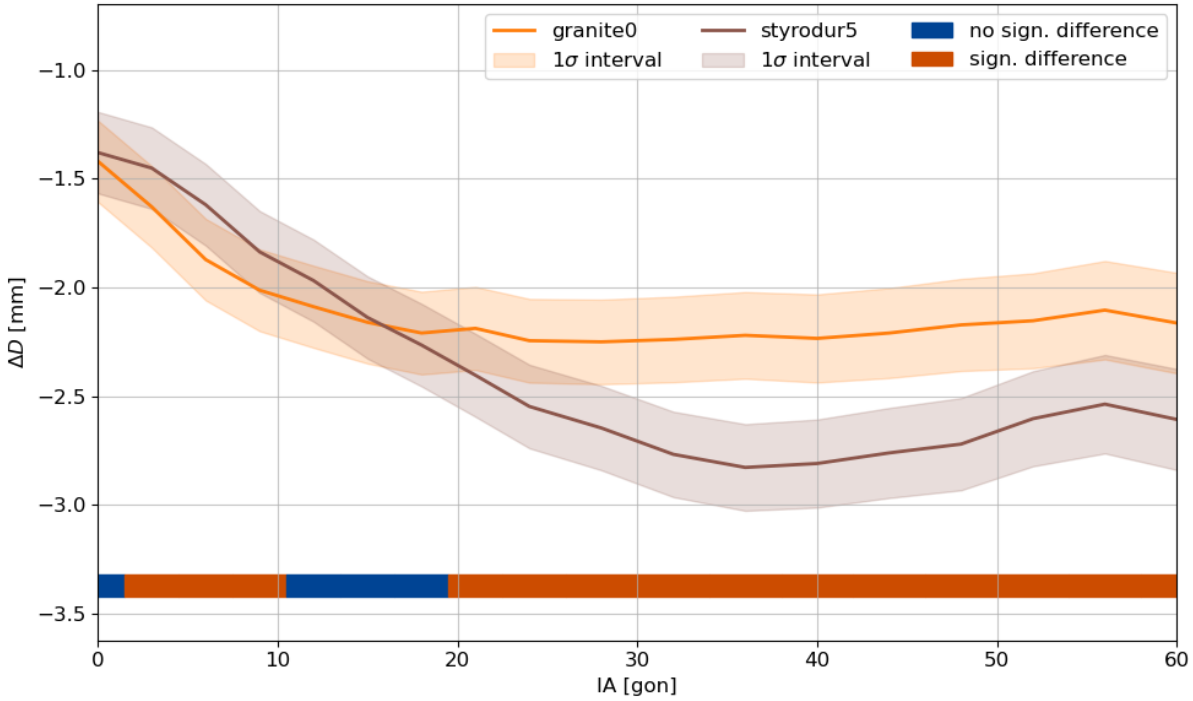

Figure B.10.: Distance differences ΔD, corresponding 1σ intervals and significance result for two materials.

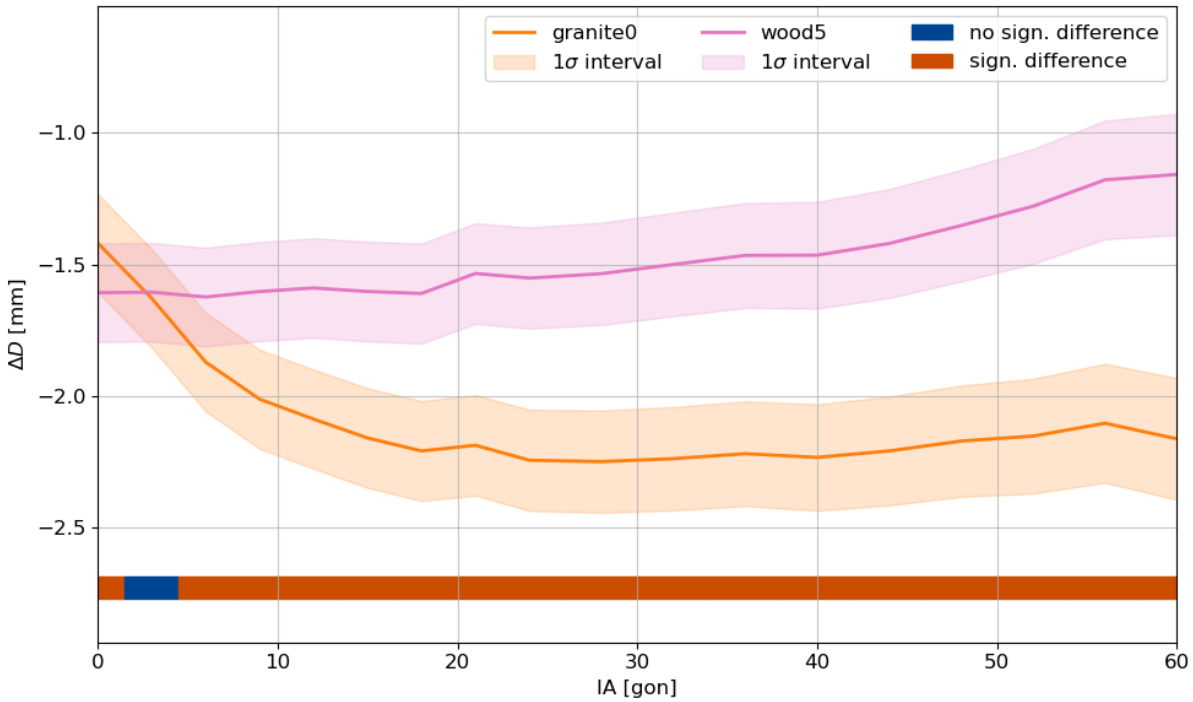

Figure B.11.: Distance differences ΔD, corresponding 1σ intervals and significance result for two materials.

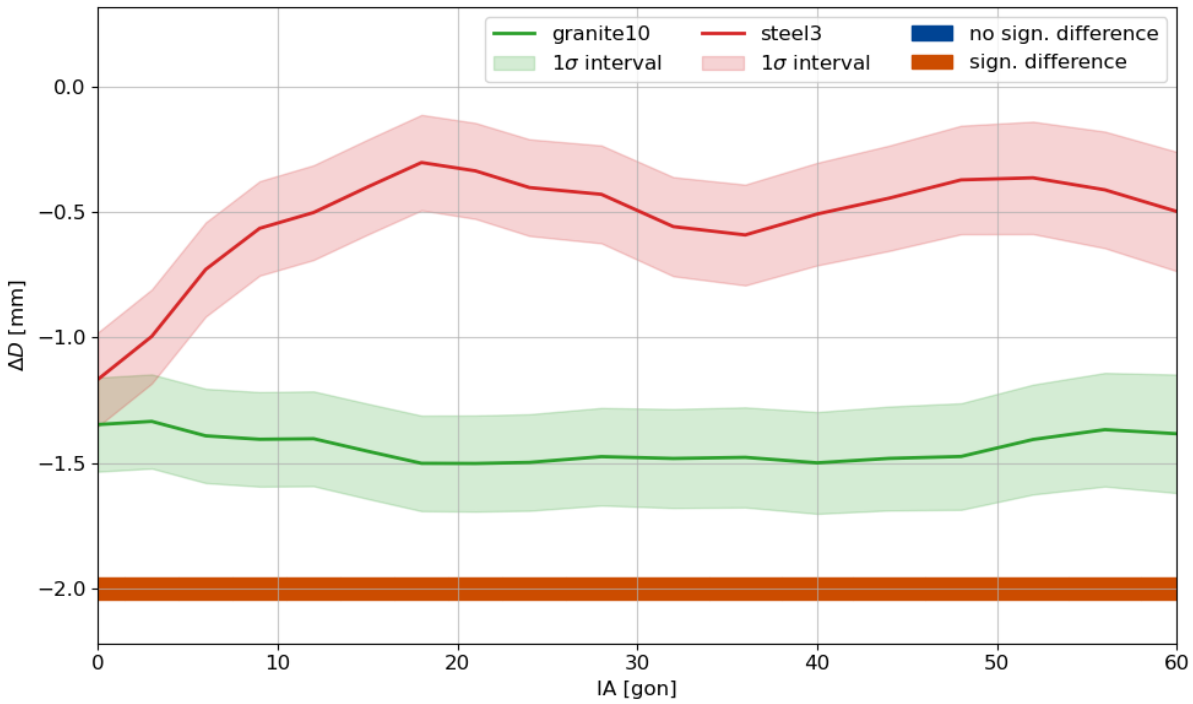

Figure B.12.: Distance differences ΔD, corresponding 1σ intervals and significance result for two materials.

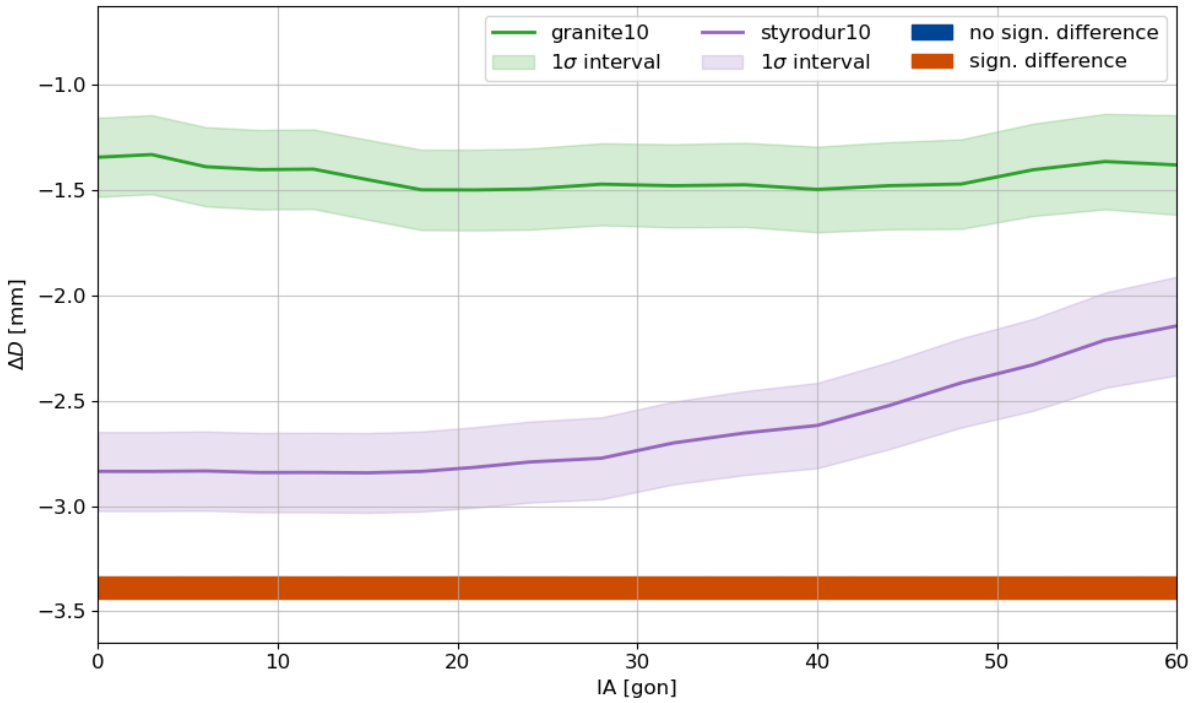

Figure B.13.: Distance differences ΔD, corresponding 1σ intervals and significance result for two materials.

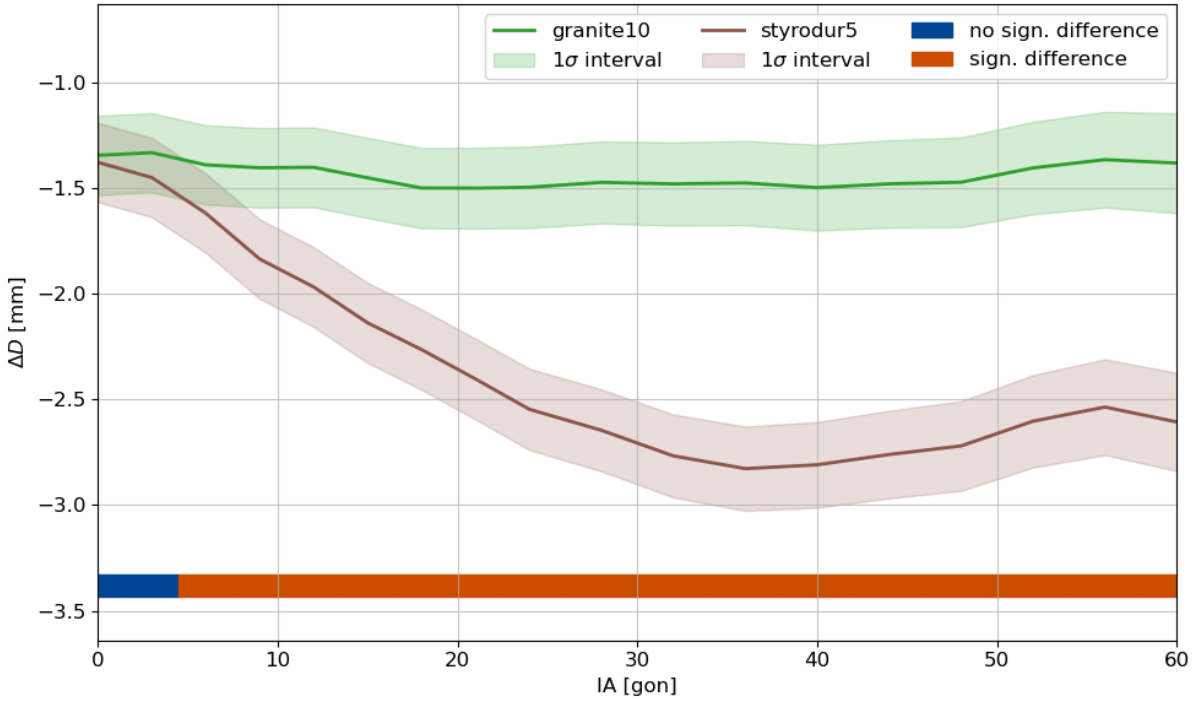

Figure B.14.: Distance differences ΔD, corresponding 1σ intervals and significance result for two materials.

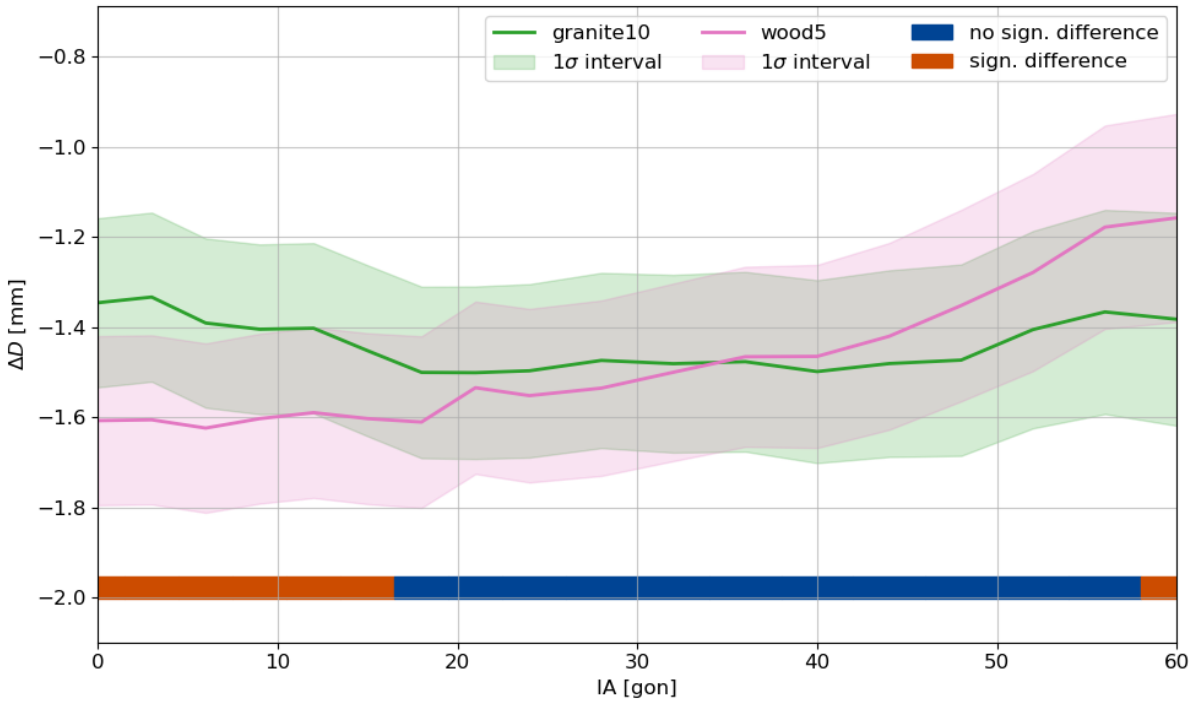

Figure B.15.: Distance differences ΔD, corresponding 1σ intervals and significance result for two materials.

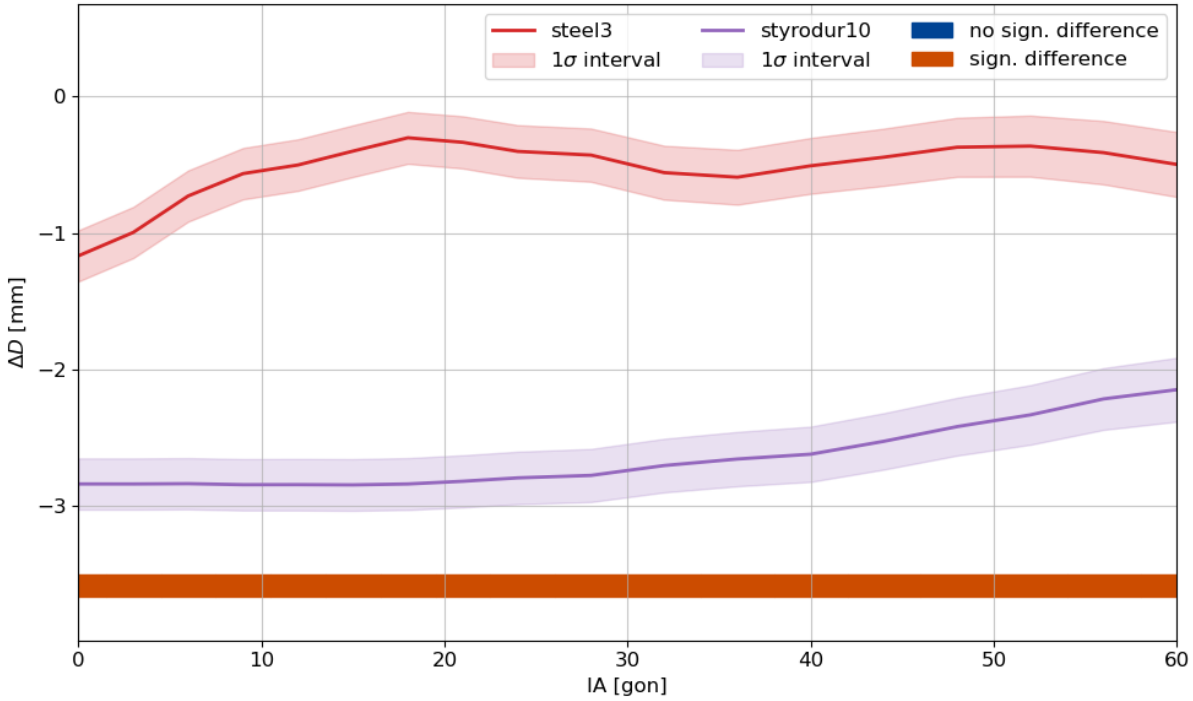

Figure B.16.: Distance differences ΔD, corresponding 1σ intervals and significance result for two materials.

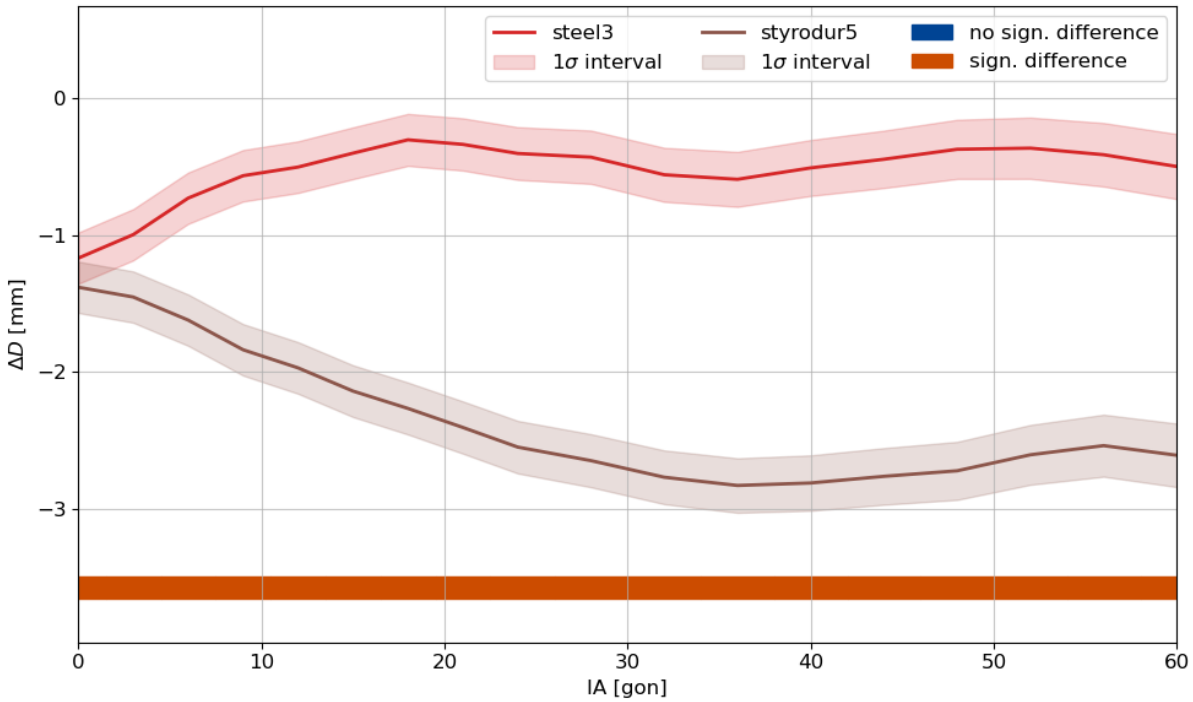

Figure B.17.: Distance differences ΔD, corresponding 1σ intervals and significance result for two materials.

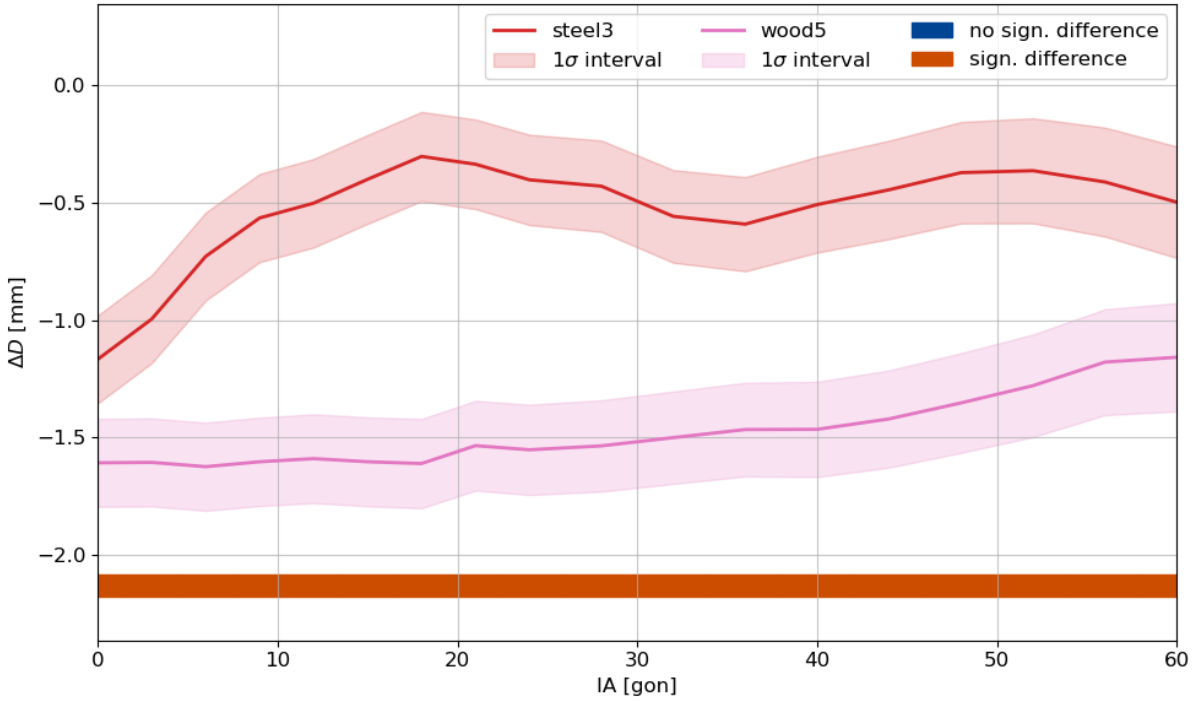

Figure B.18.: Distance differences ΔD, corresponding 1σ intervals and significance result for two materials.

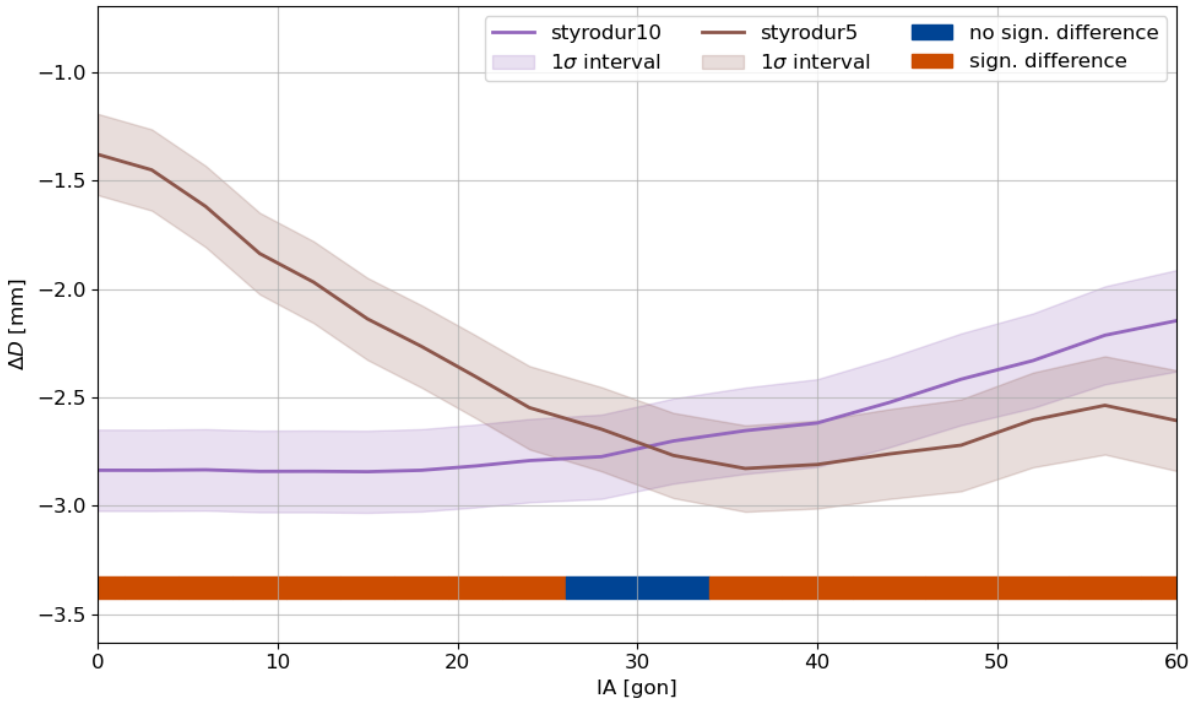

Figure B.19.: Distance differences ΔD, corresponding 1σ intervals and significance result for two materials.

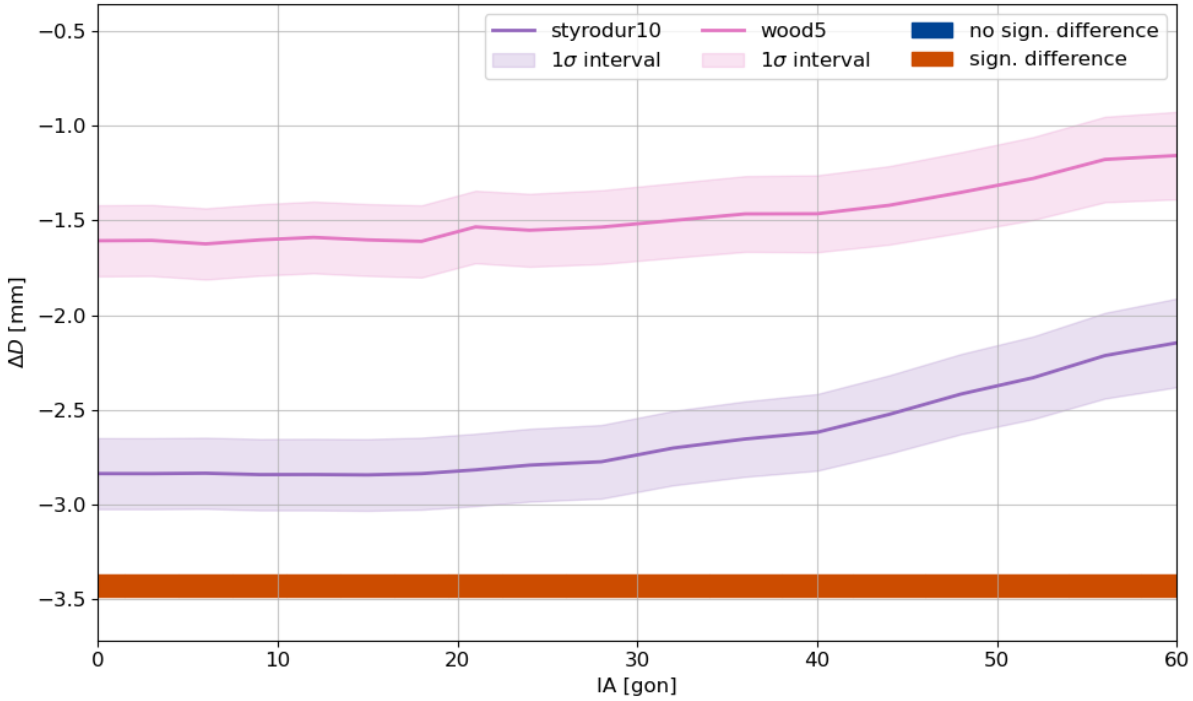

Figure B.20.: Distance differences ΔD, corresponding 1σ intervals and significance result for two materials.

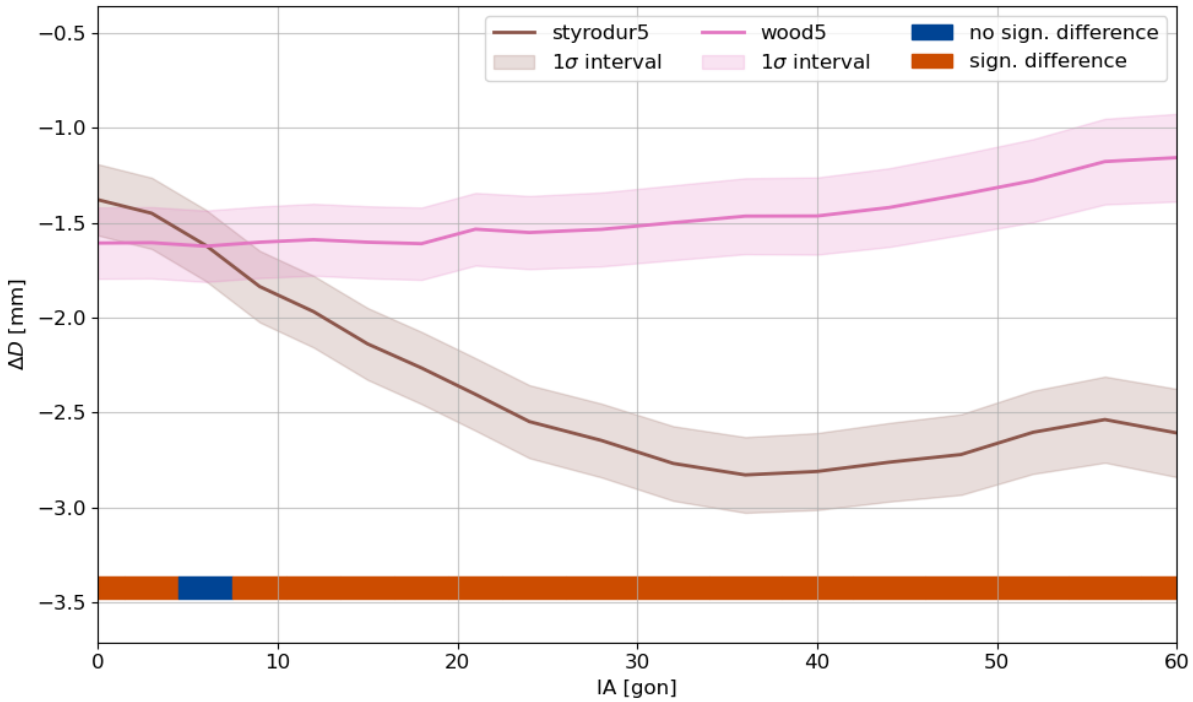

Figure B.21.: Distance differences ΔD, corresponding 1σ intervals and significance result for two materials.